STUDY OF SUBPICOSECOND ELECTRON TRANSPORT IN GaAs USING TRANSIENT PHOTOCONDUCTIVITY AND TRANSIENT ABSORPTION SPECTROSCOPY

by

Kevin E. Meyer

Submitted in Partial Fulfillment

of the

Requirements for the Degree

DOCTOR OF PHILOSOPHY

Supervised by Professors Gerard Mourou and Theodore Castner

Department of Physics and Astronomy

University of Rochester

Rochester, New York

1988

BIOGRAPHY

Kevin E. Meyer was born on July 19, 1958 in Poughkeepsie, New York. From 1976 to 1980 he attended Bucknell University in Lewisburg, Pennsylvania where he was granted a B.S. in Physics with a minor in Music. During his senior undergraduate year he took part in the Undergraduate Research Participation Program at Argonne National Laboratory where he performed research in the Solid State Science Division. After receiving his B.S. he returned to Argonne National Laboratory as a participant in the 1980 Summer Energy Research Institute. In the fall of 1980 he entered the Ph.D program at the University of Rochester in the Department of Physics and Astronomy. During his first two years he taught undergraduate solid state physics laboratories. In 1981 he worked as a Summer Technical Employee at the RCA David Sarnoff Research Center in Princeton, New Jersey. In the fall of 1981 he began work as a part-time co-op student and later as a full-time co-op student at the Xerox Webster Research Center in Webster, New York. In 1983 he joined the Ultrafast Sciences Group at the Laboratory for Laser Energetics, where he has conducted his thesis research under the supervision of Gerard Mourou and Ted Castner. Mr. Meyer is also a member of the American Physical Society.

ACKNOWLEDGEMENTS

It is a great pleasure to acknowledge the continuous support of Gerard Mourou, who has served as a source of ideas, expertise, and encouragement throughout the course of this work. I am also grateful to my advisor in Physics, Ted Castner, for many helpful discussions.

I have been very fortunate to have developed strong collaborations with a number of very fine theorists who have performed detailed simulations of my experiments. These include Bob Grondin, Sleiman Chouman, and Dave Ferry at Arizona State University and Mohammed Osman and Hal Grubin at Scientific Research Associates.

There are nearly too many students and staff to mention at the Laboratory for Laser Energetics who have influenced my research. Special thanks go to Ted Norris and Maurice Pessot for keeping sometimes temperamental lasers running far into the night. Other members of the Ultrafast Sciences Group who have been helpful include Doug Dykaar, Steve Williamson, John Whittaker, Todd Jackson, and Bill Donaldson. Many thanks to Jean Steve and Millie Grassi, our irreplaceable group secretaries, and to the Illustration Department, including Autumn Craft, Antonia Sweet, Diane Hixson, and Ladonna Black for consistently high-quality graphics.

There are several people who have been responsible for growing and fabricating specialized samples. Thanks to Gary Wicks and Bill Schaff at Cornell University for providing MBE material. Special thanks for all the cooperation from the Microelectronic Engineering Department at the Rochester Institute of Technology, headed up by Lynn Fuller, for teaching me the photolithography ropes. Kurt Kubath and Alex Matsev in the Optical Fabrication Shop have been responsible for many demanding grinding and polishing tasks and Doug Smith has supplied his expertise in optical coatings. This research was supported by AFOSR Grant #84-0318.

I am very grateful for the love and continuous support, emotional as well as financial, of my parents, who have always encouraged me to go after my dreams. Many thanks to the rest of my family as well, especially my sister Karen. I also appreciate the love of many close friends, including Sue Anders, Susan Dyer, Mary Gene Heinmiller, Gretchen Otting, Barbara Lakeburg, Patricia Lamos, and John Sweeney. Finally, I'd like to acknowledge the spiritual and emotional support provided by my "adopted family" at South Presbyterian Church, with special warm thanks to the Reverend Ray Trout.

DEDICATION

This work is dedicated to Laura, my "one-woman cheering section", without whom I would never have found the strength to persevere along what has been a long and winding road. It is also dedicated to the memory of Virginia Dawson, my "adopted grandmother".

ABSTRACT

The experimental study of subpicosecond transport in GaAs and other semiconductors is of fundamental importance for the understanding of scattering processes on very short time scales. New theoretical approaches have been developed to describe transport physics in this regime and these theories must be tested. From a practical point of view many active devices of different types operate on a picosecond time scale; the basic physics operant in these devices must be well understood before their speeds can be extended into the subpicosecond range.

The purpose of this work has been to develop and demonstrate techniques which are capable of measuring electron velocities and energies on a time scale of a few hundred femtoseconds. The two approaches described here are transient photoconductivity measured via electro-optic sampling and transient absorption spectroscopy obtained with a femtosecond continuum pump/probe arrangement.

Detailed Monte Carlo calculations of the evolution of the electron drift velocity and energy distribution for experimental conditions of interest have been developed. These calculations take into account all of the important scattering mechanisms, including, where appropriate, electron-electron and electron-hole interactions.

Transient photoconductivity results obtained using two different excitation wavelengths are qualitatively in very good agreement with the theoretical predictions. In particular a photocurrent overshoot with a risetime of 420fs has been measured which correlates well with the predicted electron velocity overshoot. To the author's knowledge this constitutes the first fully time-resolved measurement of velocity overshoot at room temperature. The Jones-Rees effect, which is apparent as a delay in the onset of photoconductivity at low fields, has also been observed.

Time-resolved transient absorption measurements have been undertaken for the first time with an applied electric field. In the absence of an applied field the observed thermalization of the electron distribution within the first 200fs following excitation is in good agreement with other results published in the literature. When the field is applied an increase in the population of the tail of the distribution due to electron heating via the field has been observed during the first 200fs. This is in qualitative agreement with Monte Carlo predictions. Due to nonuniformities in the field within the sample the observed field effect is not as large as predicted. Improvements in the experiment are discussed to achieve a uniform field which should yield experimental results in quantitative agreement with the theory.

TABLE OF CONTENTS

(7) Appendices

FIGURES AND TABLES

There was no 'One, two, three, and away,' but they began running when they liked and left off when they liked, so that it was not easy to know when the race was over.

Lewis Carroll

1. Introduction

The study of electron transport in GaAs has been driven by two separate but related forces. The first is that since the 1960's theorists have predicted several anomalous effects that should occur in this and other III-V materials, including negative differential resistance and the Gunn effect, velocity overshoot, and most recently hot phonon effects. In parallel with these theoretical developments has been the steady increase in applications of GaAs devices in communication and computer technologies. Two specific areas in which GaAs has a distinct advantage over its more mature Si competitor are in high-speed applications, because mobilities are generally higher in the III-V materials, and in optical and electro-optic devices, which take advantage of the direct-gap and electro-optic nature of GaAs. Currently the field of GaAs electro-optic devices is expanding geometrically as researchers explore the possibilities of ultra-high-speed hybrid optoelectronic computers and the "ultimate" possibility of an all-optical computer.

Despite this wealth of activity there are many details concerning the band structure and transport properties of GaAs which have been only indirectly measured if indeed they have been measured at all. An honest theorist who performs Monte Carlo calculations, which are being relied upon more and more heavily, will somewhat reluctantly admit that many of the 40-odd parameters that go into a typical calculation are best estimates based upon various band structure calculations. Clearly there is a need for carefully designed experiments which can illuminate some of the fundamental aspects of transport in GaAs.

Much of the early work on GaAs focussed on the potential development of its negative differential resistance (NDR) characteristics which were predicted by Ridley and Watkins [1]. In principal such behavior could be utilized for amplification similar to the Esaki tunnel diode. The steady-state velocity-field curve published by Ridley

and Watkins is shown in Fig. 1.1 along with a simplified band structure diagram. Ridley and Watkins postulated that for high fields electrons which were initially at the band edge would eventually gain sufficient energy from the applied electric field that they could scatter out of the central valley into the sidebands. The electron mobilities in the sidebands are considerably lower than in the central valley and hence electrons would slow down. According to the simple argument that the current density J=nev this would imply that above a threshold field of 3kV/cm the effective resistance of the device would be negative.

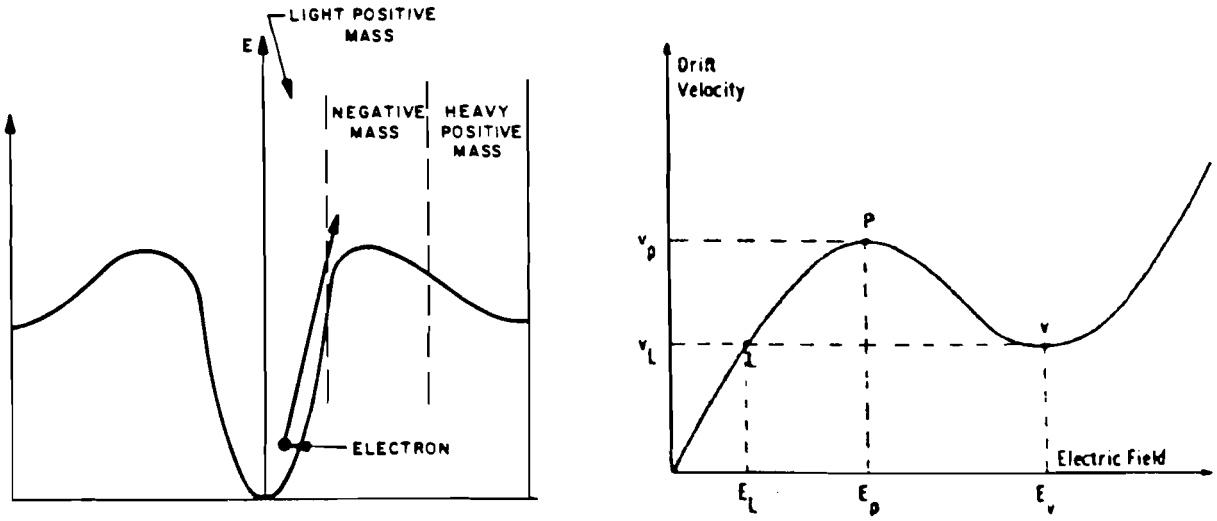

Fig. 1.1 Simplified band structure diagram of GaAs and the electron velocity-field curve predicted by Ridley and Watkins [1].

One of the first investigators to study the current-voltage behavior of GaAs was Gunn [2,3]. Gunn found that unlike germanium, which exhibited a saturated current at high fields, the GaAs response demonstrated extremely high-frequency current oscillations above a certain threshold field. The amplitude of the oscillations was large, with as much as 1-2% of the incident power being converted into RF

power. Gunn found that the frequency of oscillation scaled inversely with the sample length, indicating that the phenomenon was a transit-time effect. An analysis by Ridley [4] showed that the oscillations were a consequence of NDR. A uniform field distribution across the sample is not stable in a negative conductivity regime. Under certain conditions space-charge accumulation layers form in domains at the cathode which propagate across the sample to the anode with the drift velocity of the carriers. This gives rise to current oscillations at the terminals of the device which may have frequencies as high as 100GHz. This phenomenon formed the basis of a new class of devices, called Gunn diodes, which have been used extensively as oscillators for the generation of millimeter-wave radiation.

In order to understand the dynamics of electrons injected into a GaAs FET Ruch [5] performed a Monte Carlo simulation of an ensemble of electrons accelerated by a uniform electric field which was turned on instantaneously at t=0. The resultant transient electron drift velocity calculations are shown in Fig. 1.2 for three different applied fields. The behavior of the low-field transient was as expected. Electrons are initially accelerated by the applied field but eventually reach an equilibrium velocity which is determined by scattering with the lattice and impurities. At high electric fields the transient behavior is dramatically different. The electrons are accelerated to very high velocities for the first 400fs, reach a peak velocity, and then relax after a few picoseconds to a relatively low equilibrium velocity. This phenomenon is referred to as velocity overshoot. The mechanism is the same one that is responsible for NDR. Electrons are initially in the central valley at the band edge, where their mobility is high. When the field is turned on they are accelerated and gain energy and velocity from the field. As they gain energy they climb up the energy band until, at 300meV, they have sufficient energy to scatter into the sidebands and subsequently slow down. More electrons are in the sidebands at high field than low field, which is why the

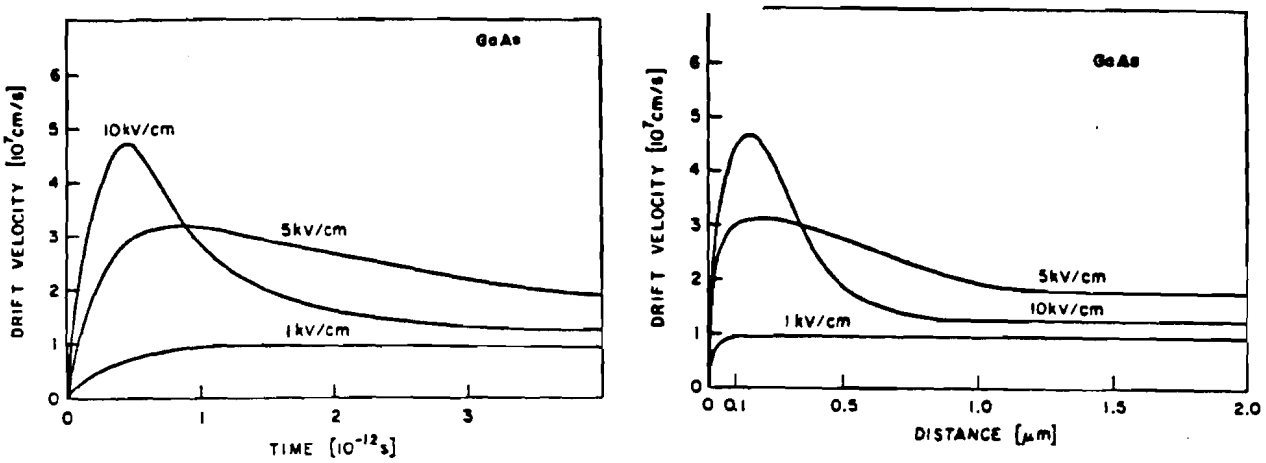

Fig. 1.2 Transient electron drift velocity in GaAs plotted versus time and propagation distance as calculated by Ruch [5].

high-field equilibrium velocity is lower.

In Fig. 1.2 is also plotted the transient electron drift velocity versus distance. This demonstrates the prediction that, for devices whose speed is determined by the electron transit time across the device, an enhancement of the device speed may be obtained if the channel length is reduced to less than one micron. The speed may in principal be very significantly increased if the channel length is made as short as 0.25um. It is on this premise that extensive research has been focussed on the fabrication of short-channel FET structures. A calculation by Shur [6], which assumes that the cutoff frequency of an FET is simply inversely proportional to the transit time, is shown in Fig. 1.3. The solid line does not include overshoot effects while the dotted line has such effects included. For gate lengths of less than one micron the cutoff frequency is enhanced and for a gate length of 0.25um overshoot effects increase the cutoff frequency by nearly a factor of three.

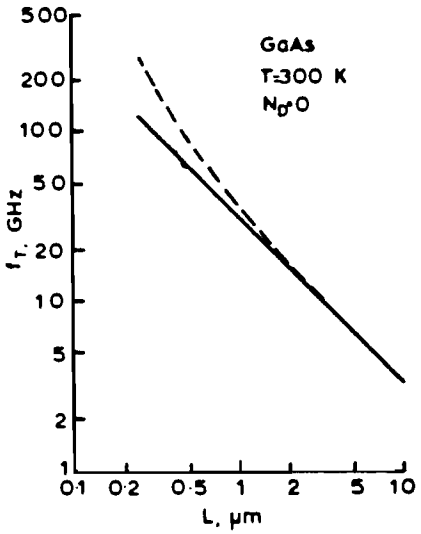

Fig. 1.3 Calculation of the cutoff frequency of a GaAs FET versus gate length: dotted line includes overshoot effects, solid line does not [6].

For actual GaAs MESFET's the general trend has been an increase in the operating frequency with decreasing gate length, but this cannot be attributed solely to reductions in the transit time [7]. Decreasing the gate length increases the transconductance and reduces the gate-source capacitance which together increase the cutoff frequency. The parasitic capacitances and resistances of the device must be carefully minimized, otherwise they will determine the upper frequency limit of the FET. A GaAs MESFET with a gate length of 0.2um has demonstrated an oscillation frequency as high as 110GHz [8]. A modification of the standard planar device design was introduced by Mishra et. al. [9] and Frensley et. al. [10]. By fabricating the device vertically short-channel devices with good uniformity and well-defined gate lengths could be obtained. This so-called VFET (Vertical FET) was predicted to have a maximum oscillation frequency of 200GHz. A similar structure called the PBT (Permeable Base Transistor) has an imbedded metallic grating as the gate and has

demonstrated an oscillation frequency of 200GHz [11].

In spite of this volume of research based upon the principal of overshoot, there remains extremely little direct evidence of velocity overshoot and "quasiballistic" transport in the literature. This is primarily due to two reasons. First, the appropriate time scale is only a few hundred femtoseconds, a regime which has been largely inaccessible until the recent advent of ultrafast dye lasers. Secondly, it is difficult to design an experiment in which the observable parameter can be directly related to the intrinsic electron drift velocity. Often space-charge effects, displacement currents, hole currents, trapping, heating effects, and other problems obscure the results. Chapter 3 will describe in detail the different experimental approaches that have been developed to date to measure transient drift velocities. The advantages and disadvantages of each of these techniques and their relationship to the approach taken in this work will be discussed.

Chapter 2 will introduce the appropriate theoretical concepts necessary to describe subpicosecond electron transport, including the important scattering processes that contribute to the electron velocity. The time-dependent Boltzmann equation will be reviewed and the difficulties of applying it to a realistic semiconductor on a subpicosecond time scale will be discussed. The retarded Langevin equation will be described which illuminates some aspects of the velocity overshoot problem. Finally, the Monte Carlo technique will be detailed as an appropriate way to model the semiconductor system in all of its complexity.

Chapter 4 will focus on the application of transient photoconductivity measurements to the study of subpicosecond electron transport. A qualitative theory will be described which shows the direct relationship between a transient voltage generated by a GaAs photoconductive switch and the transient electron drift velocity. The electro-optic sampling technique, which is capable of measuring transient voltage

waveforms on a time scale of a few hundred femtoseconds, will be presented. Monte Carlo predictions of the electron drift velocity specific to our experimental conditions, which have been carried out by Robert Grondin at Arizona State University, will be shown. In addition, experimental results that constitute a time-resolved qualitative measurement of velocity overshoot and the related phenomenon of the Jones-Rees effect, obtained at two different excitation wavelengths, will be described.

A complementary experiment which yields direct information about the electron distribution function, referred to as transient absorption spectroscopy, will be reviewed in chapter 5. Recall that velocity overshoot is caused by field-induced heating of the electrons and subsequent intervalley transfer. This heating is reflected in the shape of the electron distribution, which may not necessarily have an exponential form and which in general will have a characteristic temperature which is higher than the lattice temperature. Hence time-resolved measurements of the evolution of the distribution function will give information about electron heating which will complement the transient photoconductivity data. Monte Carlo predictions, developed by Mohammed Osman at Scientific Research Associates, will be compared with transient absorption data obtained using two different pump/probe configurations.

2.1 Introductory Comments

The theoretical description of subpicosecond carrier transport in GaAs involves the extension of standard solid state concepts into unique regimes, where in fact it will be seen that many familiar assumptions break down. Along with the need for new theoretical approaches comes the need for care in the terminology used for conceptualization. For example, when carriers have kinetic energies larger than the lattice temperature they are often referred to as "hot electrons", even though in the transient regime the distribution function may be highly non-Maxwellian and hence a well-defined temperature does not exist. Another example is the use of the terms "ballistic" or "quasi-ballistic", referring to the initial instance of time during which the carriers are accelerated freely by the applied field without collisional interference . This term may apply to the first few tens of femtoseconds of transport, but the emphasis here will be on the energy loss rate of the carriers and whether the carriers have gained sufficient energy between collisions to undergo intervalley transfer to the sidebands. The terms used to describe this regime will be "transient", "non-stationary", and "subpicosecond."

2.2 Band Structure and Scattering Mechanisms

GaAs is a III-V semiconductor which crystallizes in the cubic zincblende structure. It is a direct-gap semiconductor which implies that light at the bandgap energy is absorbed very efficiently; the bandgap at room temperature is 1.423eV (871nm). Incident light at this or shorter wavelengths will create free electrons and holes whose transport is governed by the band structure shown in Fig. 2.2.1 [12]. The conduction band has three valleys, the Γ, L, and X valleys. The effective mass of the electrons at the minima of these valleys is $0.067m_0$, $0.222m_0$, and $0.58m_0$

respectively, so that electrons in the Γ valley have much higher mobilities than in the L or X valleys. In addition, the effective electron mass at intermediate energies is governed by the curvature of the energy band, which in general is non-parabolic. For the holes there are three separate bands of importance. There are two adjacent bands, the heavy hole (m_{hh}=0.51m_0) and light hole (m_{lh}=.082m_0) bands, which are

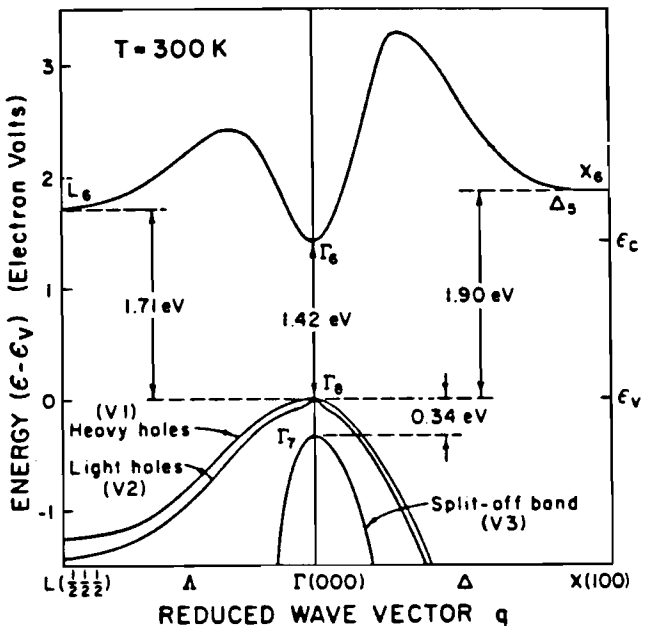

Fig. 2.2.1 Band structure of GaAs [12]

degenerate at the band edge, plus a split-off band (m_{so}=0.154m_0). The density of states of the light hole band is considerably lower than for the heavy hole band, so that over a wide temperature range the light holes only constitute ~7% of the total hole population [12]. For the split-off band the density of states is extremely low so that $p_{so}/p_0 < 0.0004$ [12], however, the band is important for some optical transitions away from the band edge, as will be discussed in Chapters 4 and 5.

Several different scattering mechanisms are operant in GaAs, including ionized impurities, optical and acoustic phonons, and carrier-carrier scattering. Each of these may be responsible for intravalley scattering, intervalley scattering, or both.

of these may be responsible for intravalley scattering, intervalley scattering, or both. Each may be characterized in terms of an interaction potential and a corresponding transition matrix element. According to the Fermi Golden Rule, the transition probability from state k to state k' due to a perturbed Hamiltonian H' is

$$S(k,k') = \frac{2\pi}{\hbar} |\langle k|H'|k'\rangle|^2 \delta(E'-E) \qquad [2.2.1]$$

where E and E' are the energy eigenvalues of the initial and final states. If the matrix element is Fourier transformed it may be factorized:

$$|\langle k|H'|k'\rangle|^2 = V(q)G(k,k') \quad q \equiv k'-k \qquad [2.2.2]$$

$$S(k,k') = \frac{2\pi}{\hbar} V(q)\, G(k,k')\, \delta(E'-E) \qquad [2.2.3]$$

V(q) is the squared Fourier transform of the interaction potential. G(k,k') is the overlap factor between the periodic part of the Bloch wavefunctions of the initial and final states. Particular forms for V(q) for different scattering mechanisms will be discussed below.

The simplest scattering mechanism of importance is that of ionized impurity scattering. The interaction potential is an electrostatic Coulomb potential. Two approaches have been developed to describe the screening of the potential, namely that of Conwell and Weisskopf [13] and Brooks and Henry [14]. The Brooks-Henry model uses an exponentially screened potential:

$$V(r) = \frac{Ze}{4\pi r} e^{-\beta r} \quad \beta = \left[\frac{ne^2}{k_\beta T}\right]^{\frac{1}{2}} \qquad [2.2.4]$$

where Z is the number of charge units at the impurity and β is the Debye-Huckel inverse screening length. The square of the matrix element is given by:

$$V(q) = \frac{N_I Z^2 q^4}{(4\pi\varepsilon)^2 (q^2 + \beta^2)} \qquad [2.2.5]$$

where N_I is the density of ionized impurities (usually assumed to be ~$10^{15}cm^{-3}$). Because the interaction is electrostatic in nature it is only important for low electron energies. At low fields the electron mobility will be determined by the impurity scattering, while at high fields phonon scattering and intervalley transfer will dominate.

Several different electron-phonon interactions are important in GaAs. The acoustic and optical dispersion relations for the zones of interest as obtained by Waugh and Dolling [15] are shown in Fig. 2.2.2. Each of these branches will be discussed separately below.

Phonons can interact with electrons in two ways. If the presence of the

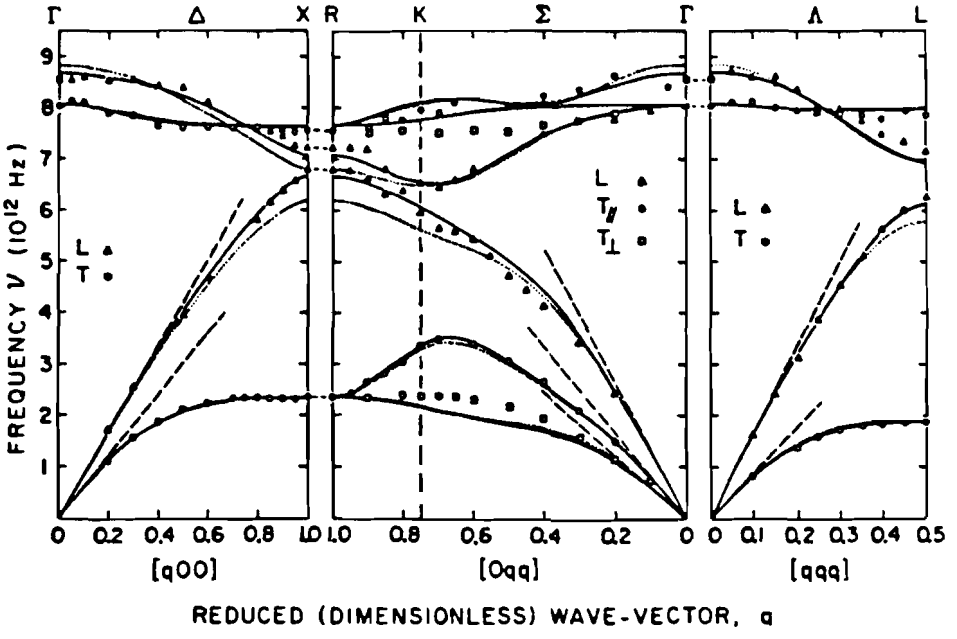

Fig. 2.2.2 Phonon dispersion relations for GaAs [15].

phonon perturbs the crystal lattice, then the interaction is referred to as the deformation-potential type and the term is applied to both acoustic and optical phonons. If the interaction is electrostatic in nature, typical of polar materials, then it is referred to as as a piezoelectric interaction for acoustic phonons and as a polar interaction for optical phonons.

Polar-optical phonon scattering results in strong coupling of the LO phonons to the electrons but negligible coupling to the TO phonons. The form for the interaction potential is

$$\phi_q = \frac{-A\,[2\rho\omega_{LO}V]^{-\frac{1}{2}}}{\varepsilon q \hbar}\left\{ a_q e^{i\vec{q}\vec{r}} + a_q^{+} e^{-i\vec{q}\vec{r}} \right\} \qquad [2.2.6]$$

where A is a proportionality constant and ρ is the crystal density. The corresponding square of the matrix element is

$$V_{LO}^{pol}(q) = \frac{e^2 \hbar\omega_0}{2\varepsilon q^2}\left(\frac{1}{\varepsilon_\infty} - \frac{1}{\varepsilon_0}\right)\left(N_0 + \frac{1}{2} \pm \frac{1}{2}\right) \qquad [2.2.7]$$

$$N_0 = \text{Bose-Einstein dist.} = \frac{1}{\exp\left[\frac{\hbar\omega_0}{k_\beta T}\right] - 1} \qquad [2.2.8]$$

ε_∞ and ε_0 are the high and low-frequency dielectric constants, the plus sign is for phonon emission, and the minus sign is for phonon absorption.

The treatment of deformation-type optical phonons is simplified by the fact that the dispersion curves (Fig. 2.2.2) are nearly independent of q. This justifies the assumption that the effective optical phonon temperature θ_{op} and distribution function N_q are independent of q. Under these conditions the squared matrix element is given by

$$V_{LO}^{def}(q) = \frac{\hbar^2 D_t^2 K^2}{2 V \rho k_\beta \theta_{op}} \left(N_q + \frac{1}{2} \pm \frac{1}{2} \right) \qquad [2.2.9]$$

where D_t is an interaction constant and K is a reciprocal lattice vector. This scattering mechanism is isotropic.

Acoustic phonons are relatively less important than the optical phonons, and only contribute significantly for high electron energies. Because the acoustic phonon energy is so low many authors assume that scattering with electrons is elastic. However, Reggiani [16] points out that for a Monte Carlo hot electron simulation a mechanism is necessary for exchange of infinitesimal amounts of energy between the electrons and the lattice. This role is filled by the deformation-type acoustic phonons. The squared matrix element has the form

$$V_{acoustic}^{def}(q) = \frac{\hbar E_1^2 q}{2 V \rho s} \left(N_q + \frac{1}{2} \pm \frac{1}{2} \right) \qquad [2.2.10]$$

where E_1 is the acoustic deformation parameter and s is the longitudinal sound velocity.

Because of the electrostatic nature of the piezoelectric interaction the scattering efficiency for that mechanism decreases with increasing electron energy, hence its role is usually neglected in hot electron simulations.

Intervalley scattering is handled separately in a Monte Carlo calculation, and it is the dominant mechanism for scattering at high fields [16]. Specifically it becomes important when the electron energy is above the threshold of 0.30eV for Γ-L transfer and 0.46eV for Γ-X transfer. Because the momentum transfer is small intervalley scattering may be formally treated in the same way as intravalley deformation-type optical phonon scattering. Therefore it takes the same form as eq [2.2.9]:

$$V_{iv}(q) = \frac{\hbar^2 D_{jk}^2}{2 V \rho k_\beta \theta_{jk}} \left(N_q + \frac{1}{2} \pm \frac{1}{2} \right) \qquad [2.2.11]$$

where D_{jk} is an appropriate interaction constant for scattering from the jth to the kth

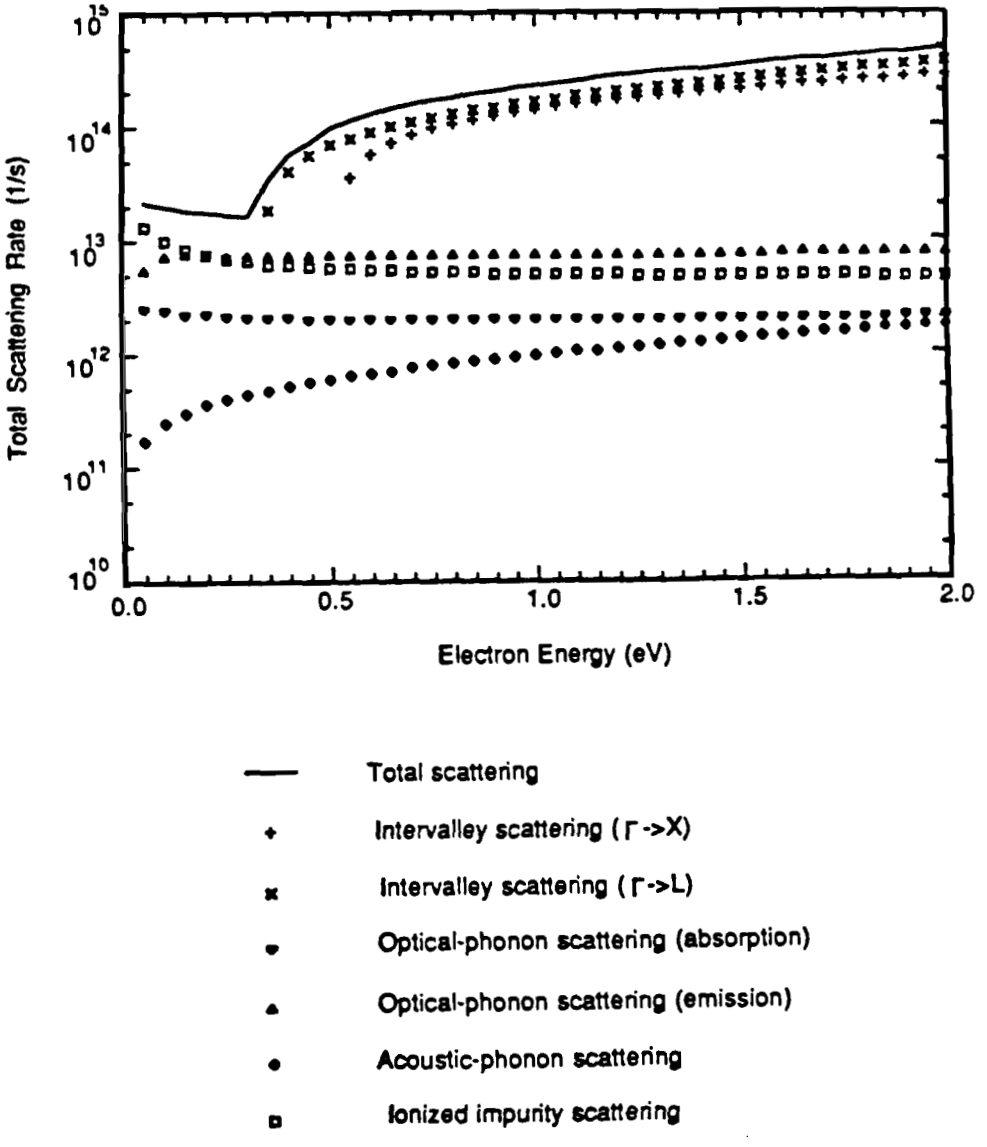

Fig. 2.2.3 Monte Carlo calculation of electron scattering rates for the GaAs Γ valley for the dominant scattering mechanisms [17].

valley induced by a phonon of energy $k_\beta\theta_{jk}$.

Fiq. 2.2.3 shows a sample Monte Carlo calculation of the total scattering rate for electrons in the Γ valley in GaAs including all of the above scattering mechanisms [17]. At low energies the dominant scattering mechanisms are ionized impurity scattering and optical phonon emission. As stated above, there is a sharp increase in the scattering rate at the threshold for Γ-L transfer and at high energies the rate is dominated by Γ-L and Γ-X scattering.

Another set of scattering mechanisms that have only recently been incorporated into Monte Carlo calculations are carrier-carrier interactions, which may be divided into electron-electron, hole-hole, and electron-hole scattering. Osman and Ferry [18,19] have carried out a detailed study of the impact of electron-hole scattering on hot phonon transport. This interaction becomes important at densities above $10^{17}cm^{-3}$ at room temperature. Because of their much lower effective mass, photoexcited electrons start out with more excess energy than their corresponding holes. The effect of the electron-hole interaction is to transfer energy from the electron ensemble to the hole ensemble, cooling the electrons and heating the holes. Recall that velocity overshoot requires electrons to transfer from the Γ to the L valley, and Γ-L transfer requires that electrons have an excess energy of 0.30eV or more. Therefore cooling of the electrons via electron-hole scattering will degrade velocity overshoot. This is shown in Fig. 2.2.4, which is a Monte Carlo calculation of electron drift velocity with $n=10^{18}cm^{-3}$ and T=300K. The solid line is with e-h collisions included, and the dashed line is without e-h collisions. In this case the degree of velocity overshoot degraded from 550% to 50% when e-h collisions were included. Fig. 2.2.5 shows the corresponding calculation for the percentage of electrons that have transferred to the L and X valleys. The percentage of transferred electrons was reduced from 50% to 30% with the inclusion of electron-hole

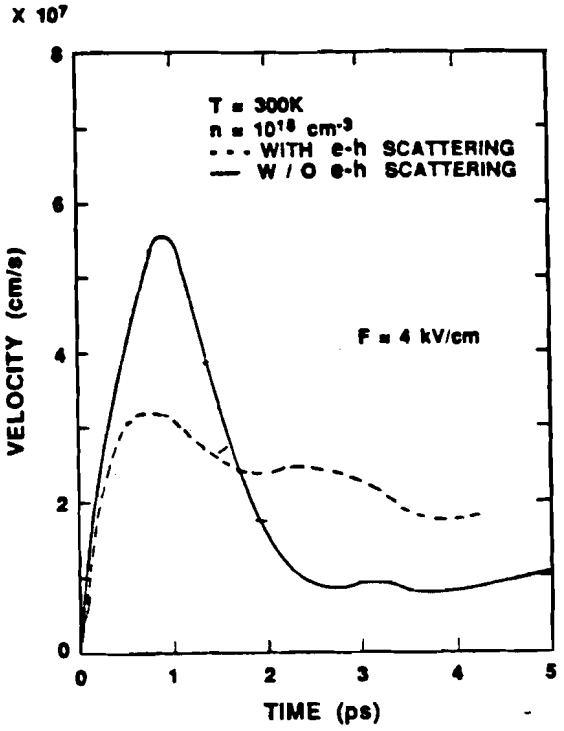

Fig. 2.2.4 Monte Carlo calculation of electron drift velocity for a density of $10^{18}cm^{-3}$ [18]. The dotted line includes e-h scattering; the solid line does not.

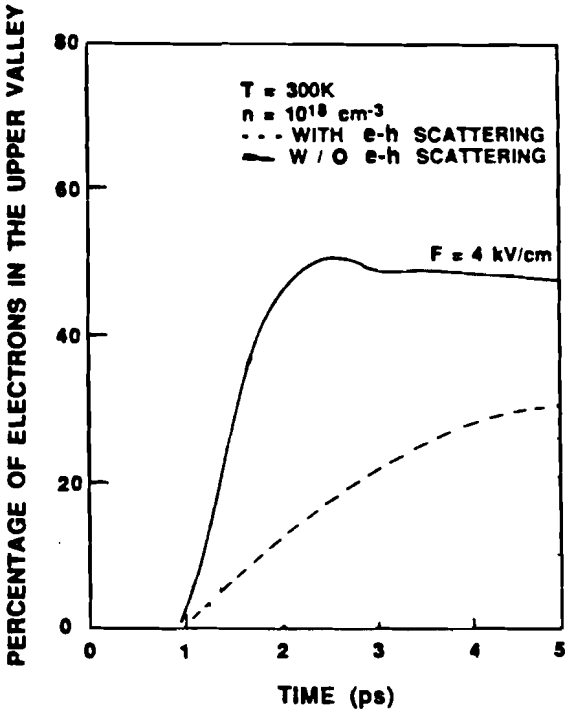

Fig. 2.2.5 Monte Carlo calculation of percentage of Γ electrons that scatter to the upper valleys [18]. The dotted line includes e-h scattering; the solid line does not.

scattering. Clearly to maximize velocity overshoot effects experiments must be undertaken at as low a density as possible, preferably at or below $10^{17}cm^{-3}$.

Electron-electron and hole-hole collisions are elastic and so will not change the average energy of an electron (hole) ensemble but will drive the distribution into a thermalized Maxwell-Boltzmann shape if it is not initially so distributed. These conclusions are based upon transient absorption experiments in bulk GaAs [20] and GaAs quantum wells [21] as well as Monte Carlo calculations [22,23]. The experiments measure the time dependence of a hot electron distribution function as it cools down from an initially near-monoenergetic photoexcited state. The electron distribution broadens to a Maxwell-Boltzmann distribution on a time scale of 200fs. Because e-e and h-h collisions do not affect the average energy of the electron and hole distributions they should not affect the magnitude of the velocity overshoot in a hot electron transport experiment, though they may have a small effect on the time scale of the overshoot [24].

2.3 Time-Dependent Boltzmann Transport Equation

This section will discuss some of the details of the application of the Boltzmann equation to transient transport along with the limitations of the approach.

According to Reggiani[16] the operator form of the Boltzmann equation may be written

$$\left[\frac{\partial}{\partial t} + \frac{d\vec{k}}{dt}\frac{\partial}{\partial \vec{k}} + \vec{v}\frac{\partial}{\partial \vec{r}} + C_k \right] f(\vec{k}, \vec{r}, t) = 0 \qquad [2.3.1]$$

where f is the distribution function and C_k is the collision operator. The usual equations for momentum and group velocity are

$$\frac{d\vec{k}}{dt} = \frac{q}{h}\vec{E}(\vec{r},t) \qquad \vec{v}(\vec{k}) = \frac{1}{\hbar}\frac{\partial}{\partial\vec{k}}\varepsilon(\vec{k}) \qquad [2.3.2]$$

If carrier-carrier scattering and space-charge effects can be ignored then the collision operator is linear in f and may be written as

$$C_k f(\vec{k},\vec{r},t) = \lambda(\vec{k}) f(\vec{k},\vec{r},t) - \frac{V_0}{(2\pi)^3}\int d\vec{k}' W(\vec{k},\vec{k}') f(\vec{k}',\vec{r},t) \quad [2.3.3]$$

$$\lambda(\vec{k}) = \frac{V_0}{(2\pi)^3}\int d\vec{k}' W(\vec{k},\vec{k}') \qquad [2.3.4]$$

where V_0 is the volume of the crystal, W(k, k') is the total transition rate, and λ(k) is the scattering rate. W(k, k') is the sum of all independent scattering processes. Microscopic reversibility has been assumed in the transition rates.

Once the transport equation has been solved then all macroscopic quantities may be found with respect to the distribution function:

carrier concentration: $$n(\vec{r},t) = \frac{1}{4\pi^3}\int f(\vec{k},\vec{r},t)\, d\vec{k} \qquad [2.3.5]$$

current density: $$\vec{J}(\vec{r},t) = \frac{q}{4\pi^3}\int \vec{v}(\vec{k}) f(\vec{k},\vec{r},t)\, d\vec{k} \qquad [2.3.6]$$

mean velocity: $$v_d(\vec{r},t) = \frac{\vec{J}(\vec{r},t)}{e\, n(\vec{r},t)} \qquad [2.3.7]$$

mean energy: $$\langle \varepsilon(\vec{r},t) \rangle = \frac{1}{n(\vec{r},t)}\int \varepsilon(\vec{k}) f(\vec{k},\vec{r},t)\, d\vec{k} \qquad [2.3.8]$$

Unfortunately, solution of the full transport equation with realistic band structure, scattering mechanisms, and boundary conditions is extremely difficult. Simplifying assumptions for particular cases of interest are usually invoked. For times much longer than the energy and momentum relaxation times, a quasi-equilibrium exists and the velocity-field relation may be derived [25,26]. For high

carrier densities, in which case carrier-carrier scattering equilibrates the respective electron and hole energies, the distribution has a characteristic temperature and hence may be described using a displaced Maxwellian formalism [27-29]. Other common assumptions include ohmic contacts, spatially uniform fields, instantaneous scattering events, parabolic energy bands, existence of a drift-diffusion relation (Einstein relation), and the effective mass approxiamation.

2.4 Retarded Langevin Equation

Boltzmann equation approaches, as described in the previous sections, are semi-classical one-electron models. One assumption in such models is that carriers respond instantaneously to changes in the applied field. However, on the short times scales of interest here it has been shown that transport is non-instantaneous and indeed non-Markovian [30]. Scattering does not completely randomize the energy and momentum of the carriers, so that memory effects are important.

A theoretical approach that illuminates the connection between electron correlations and velocity overshoot is the Retarded Langevin Equation (RLE) [30-35]. Consider an ensemble of electrons in equilibrium with the lattice; at t=0 a homogeneous steady-state electric field E_0 is turned on. The time evolution of the electron motion is determined by three factors. The electrons are accelerated by the applied field. Random changes in electron velocity are introduced by scattering events, represented by a random force R(t). Finally, there is a net momentum relaxation to the lattice through scattering which, in steady-state, is balanced by the net momentum gain from the field. The equation of motion may be written as [30]

$$m\dot{\vec{v}} = -m\int_0^t \dot{M}(t-u)\,v(u)\,du + R(t) + qE_0H(t) \qquad [2.4.1]$$

where M(t) is the so-called memory function and H(t) is the unit Heaviside function.

In steady state the derivative of the memory function is

$$\dot{M}(t) = \frac{\langle R(0)R(t)\rangle}{m^2\langle v^2(0)\rangle} \qquad [2.4.2]$$

Eq. [2.4.1] may be solved using Laplace transforms. If a function X(t) is defined in terms of the transform of M(t):

$$\hat{X}(s) \equiv (s+M(s))^{-1} \qquad [2.4.3]$$

then the solution of the transport equation has the form

$$v(t) = v(0)X(t) + \frac{qE_0}{m}\int_0^t X(u)\,du + \frac{1}{m}\int_0^t R(t-u)X(u)\,du \qquad [2.4.4]$$

If an ensemble average is performed and $\langle R(t)\rangle = 0$ is assumed, then X(t) may be written in terms of the ensemble drift velocity:

$$X(t) = \frac{m}{qE_0}\dot{v}_d(t) \qquad [2.4.5]$$

Clearly, X(t) corresponds to the macroscopic acceleration of the carriers. X(t) is also closely connected to velocity fluctuations. The velocity-velocity correlation function $\varphi(t)$ is defined as

$$\varphi(t,t') = \langle v(t)v(t')\rangle - v_d(t)v_d(t') \qquad [2.4.6]$$

Using eqs. [2.4.3] and [2.4.6] it can be shown that

$$\varphi(0,t) = \langle v^2(0)\rangle X(t) \qquad [2.4.7]$$

Hence X(t) is the non-stationary correlation function calculated at t'=0. Comparing

eqs. [2.4.5] and [2.4.7] yields

$$v_d(t) = \frac{q E_0}{m\langle v^2(0)\rangle}\int_0^t \varphi(0,t')\,dt' \qquad [2.4.8]$$

This form is recognizable as the Kubo linear response formula [36] extended into the transient regime. The validity of this formula has been proven using Monte-Carlo techniques [35]. This equation illustrates the strong connection between the drift velocity and the velocity correlation function. Clearly, if the correlation function is negative in any interval there has to be an overshoot in the velocity response. Fig. 2.4.1 shows the velocity correlation function and drift velocity calculated for electrons in silicon with T=300K and E_0=50kv/cm [37].

An additional fundamental parameter important for transport and device

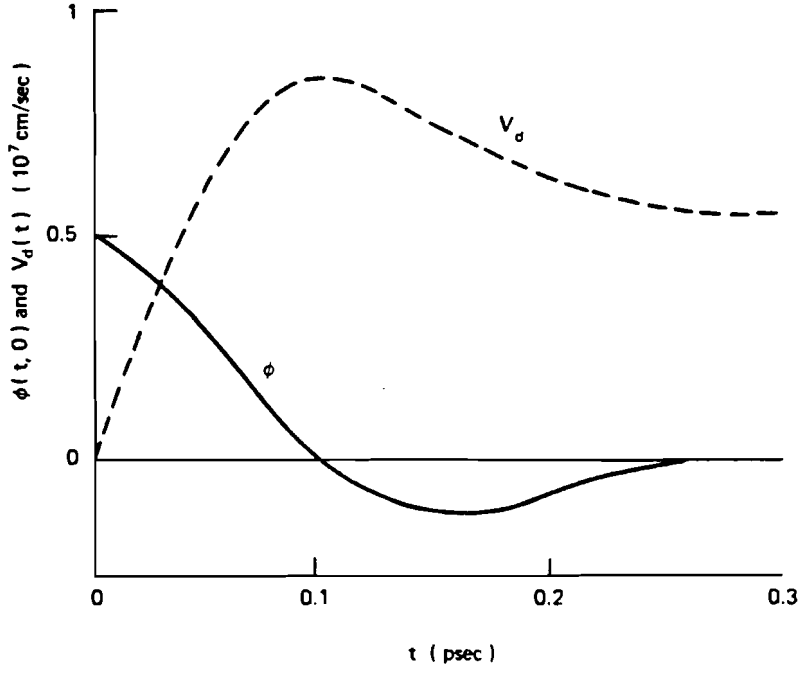

Fig. 2.4.1 Monte Carlo calculation of velocity autocorrelation function and transient drift velocity for Si. [37].

modeling is the diffusion coefficient. Within the context of the above discussion, the diffusion coefficient may be written as :

$$D(t) = \frac{1}{2}\frac{d}{dt}\langle x(t) - \langle x(t)\rangle\rangle^2 = \int_0^t \varphi(t', t)\, dt' \qquad [2.4.9]$$

An example of calculated values for the drift velocity, the second moment , and the

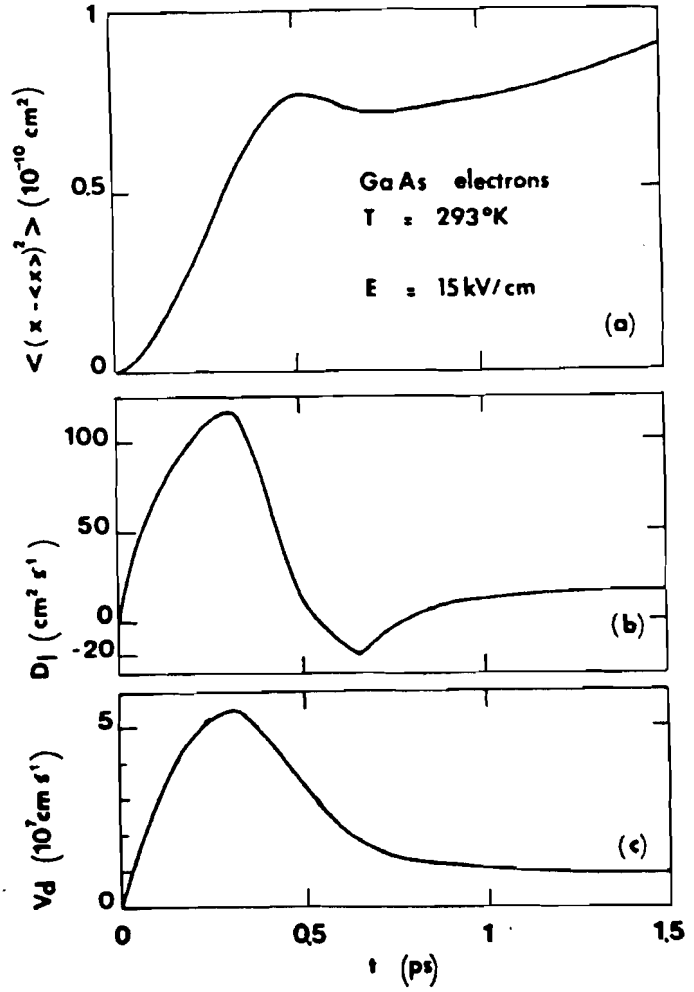

Fig. 2.4.2 Monte Carlo calculation of second moment, diffusion coefficient, and drift velocity for electrons in GaAs [38].

related diffusion coefficient are shown in Fig. 2.4.2 for GaAs at T=300K and E_0=15kv/cm [38]. In the transient regime, because memory effects cause both the drift velocity and the diffusion coefficient to be strongly time-dependent, an Einstein-type relation, which is often assumed in device simulations, is not valid. Even in the steady-state, both the drift velocity and the diffusion coefficient are field-dependent, and a modified field-dependent Einstein relation must be used [39].

It should be noted that the RLE approach sheds light on the origin of velocity overshoot behavior, but does not facilitate calculations of the transport parameters. All the transport parameters may be written in terms of the correlation function, but imbedded in the correlation function are the details of the unknown scattering functions. Fortunately, the correlation function may be calculated numerically using the Monte-Carlo technique and known (and approximated) physical constants of the system. This numerical technique will be discussed in the following section.

2.5 Monte Carlo Approach

As has been seen in the preceding discussions, analytic solutions to semiconductor transport equations do not exist for any but the simplest systems. Photoexcited GaAs under high field conditions is not a simple system, owing to the contributions of numerous scattering mechanisms, multiple non-parabolic bands, hole contributions, and memory effects. To model such complex systems, solid state theorists often turn to numerical solutions of the transport equation, or, alternatively, to the simulation of individual electrons sequentially evolving in time under appropriate constraints. This latter method is known as the Monte Carlo technique, and has been proven to be quite a powerful tool for the understanding of transport in modern devices [40-46]. The approach will be described briefly here; for a thorough

discussion of its application to transport in semiconductors, the reader is referred to the review article by Jacobani and Reggiani [46].

There are two types of Monte Carlo analysis, the original single-particle approach and the more versatile ensemble Monte Carlo (EMC). When steady-state, homogeneous systems are simulated, the motion of a single particle is modeled and allowing the particle to evolve to equilibrium yields information about the entire system of carriers. If, however, non-stationary and/or non-homogeneous conditions exist, a large collection of particles is simulated and ensemble averages of the macroscopic variables of interest are taken at regular time intervals during the evolution of the ensemble. The latter approach is the EMC and will be the focus of the discussion here.

A flowchart of a typical Monte Carlo program is shown in Fig. 2.5.1 [46]. The initial conditions of the system are set up with the assumptions of a particular band structure, values of initial energy and momentum, and probability tables are generated to describe the various scattering mechanisms that are to be included in the calculation. A standard case, and the one of most interest in this work, is that of a cubic semiconductor with an externally applied field E. An electron is simulated with initial energy ε and momentum k; during free flight between scattering events the electron's momentum is modified by

$$\frac{d}{dt}\vec{k} = \frac{q}{\hbar}\vec{E}(\vec{r},t) \qquad [\,2.5.1\,]$$

The duration of each free flight is determined stochastically and the change in energy and momentum of each scattering event is determined by the type of scattering event chosen and the electron's incident energy and momentum. The simulation region is partitioned into spatial bins of equal size. The field, doping, and material parameters are assumed to be uniform within a bin but may vary from bin to bin. The

sampling time, the time-step at which ensemble averages are taken, should be chosen much smaller than the free flight time. A large number of electrons are simulated simultaneously and an ensemble average is taken at each sampling time for such parameters as the net drift velocity, the average energy, the average momentum, the spatial distribution, and the electron and hole energy distribution functions.

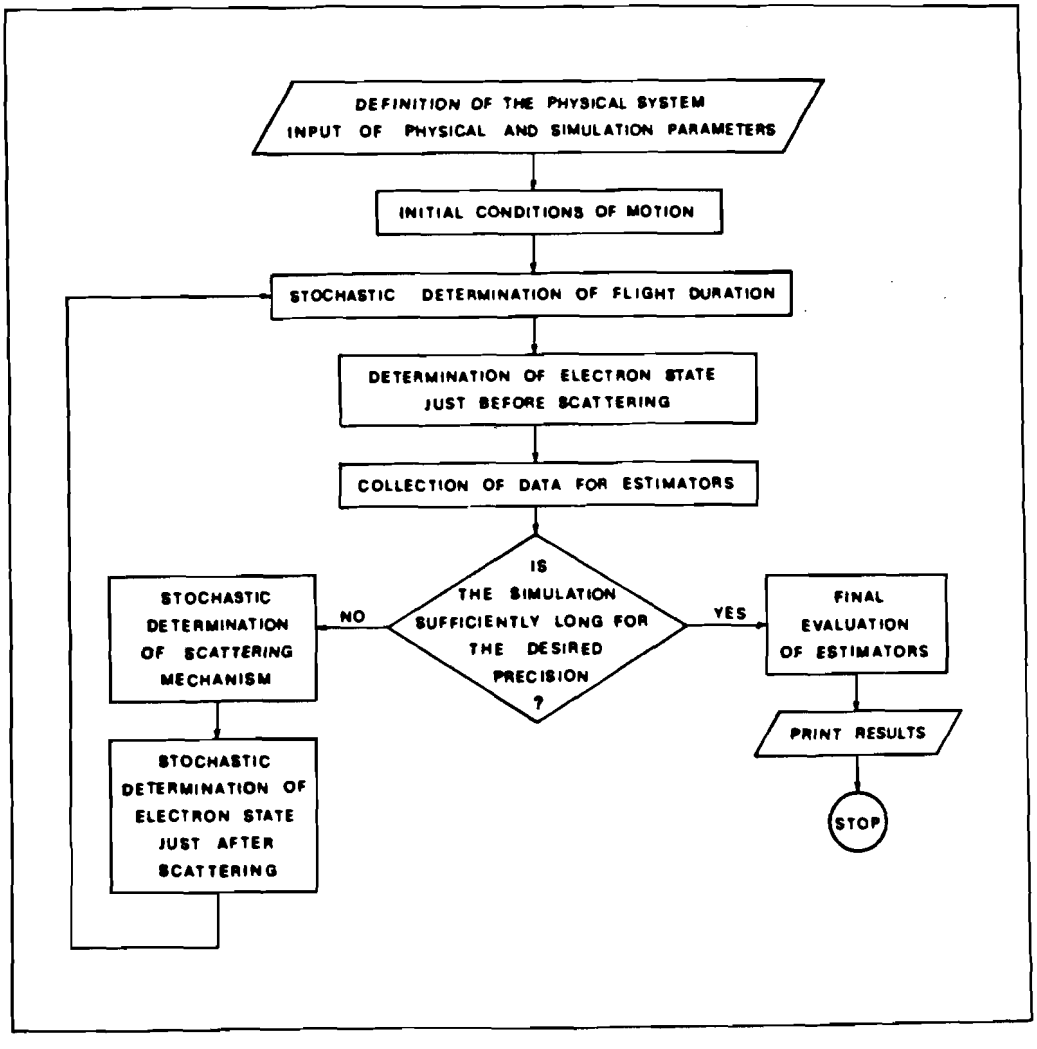

Fig. 2.5.1 Flow chart of a typical Monte Carlo calculation [46].

Chapter 3: Experimental Evidence for Subpicosecond Hot Electron Transport in GaAs

This chapter will review existing experimental evidence for velocity overshoot in GaAs and the relevance of these experiments to the present work. The approaches that will be discussed will include DC IV characterization, mm-wave DC conductivity, time-resolved Franz-Keldish effect, analysis of the operation of hot electron transistors, transient photoconductivity, and subpicosecond reflectivity measurements using optical rectification.

3.1 Transient Franz-Keldysh Effect

As will be discussed in Chapter 5, all-optical pump/probe techniques have been developed primarily for studying transient electron/hole distribution functions. Most of these approaches have taken advantage of bleaching of the optical transmission (absorption) caused by state-filling in the conduction/valence bands. A variation of this experiment, described by Shank et. al. [47], uses a different phenomenon, the Franz-Keldysh effect [48,49], to probe the space-charge field created by electron-hole pairs as they separate in an applied electric field. The magnitude of the space-charge field is dependent upon the electron/hole drift velocities, hence in principle this measurement can yield information about velocity overshoot phenomenon.

An electric field will modify photon absorption in a semiconductor in two ways [50]. It will shift the band edge, so that wavelengths which are below the unperturbed band edge and hence unabsorbed will be absorbed when a field is applied. For wavelengths above the unperturbed band edge, an oscillatory behavior will be impressed upon the absorption versus wavelength, and the period of oscillation may be used as a measure of the applied electric field. The concept of the

Shank et. al. experiment is that the space-charge field of the photoexcited carriers, which opposes the applied electric field, will be apparent as a time-dependent change in absorption near the band edge, and the time dependence will be governed by the evolution of the carrier velocities. Specifically, for constant v_e and v_h the expression for the induced absorption is

$$\frac{\Delta\alpha(t)}{\Delta\alpha(\infty)} = \frac{\int v_e\,dt - \int v_h\,dt \exp(-\alpha_p d)}{d[1-\exp(-\alpha_p d)]} +$$

$$\frac{1-\exp(\alpha_p \int v_e\,dt)}{\alpha_p}\left\{1-\exp(-\alpha_p \int v_h\,dt) + \exp(-\alpha_p d)\right\} \qquad [3.1.1]$$

where α_p is the pump absorption coefficient and d is the width of the region over which the field is applied. At short times the derivative of the above equation is approximately

$$\frac{\partial}{\partial t}\frac{\Delta\alpha(t)}{\Delta\alpha(\infty)} \approx \frac{v_e + v_h}{d} \qquad [3.1.2]$$

The structure that was studied consisted of an AlGaAs/GaAs/AlGaAs p-i-n heterostructure diode. The AlGaAs layers were optically transparent and the "transport" layer of GaAs was undoped and 2um thick. Carriers were excited using a 0.5pS pulse at 8050Å generated from an amplified mode-locked dye laser. The absorption of the sample was measured by a broad-band probe beam produced by continuum generation in a CCl_4 cell. The measurements were performed at 77K.

Induced absorption at a fixed pump/probe delay of 20pS with three different applied fields is shown is Fig. 3.1.1. The oscillation frequency was dependent upon the applied field, as expected, and the period was used to calibrate the measurement. The total absorbance change was obtained by integrating these curves and plotting the

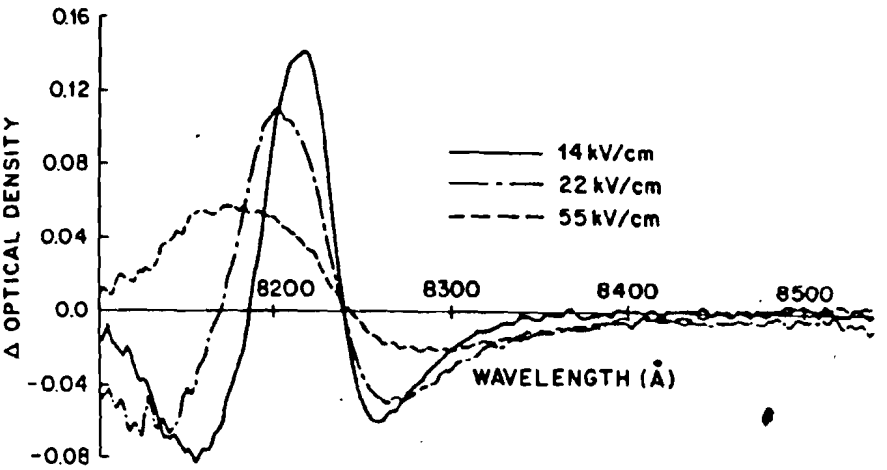

Fig. 3.1.1 Induced absorption at a pump/probe delay of 20 ps for three different applied fields [47].

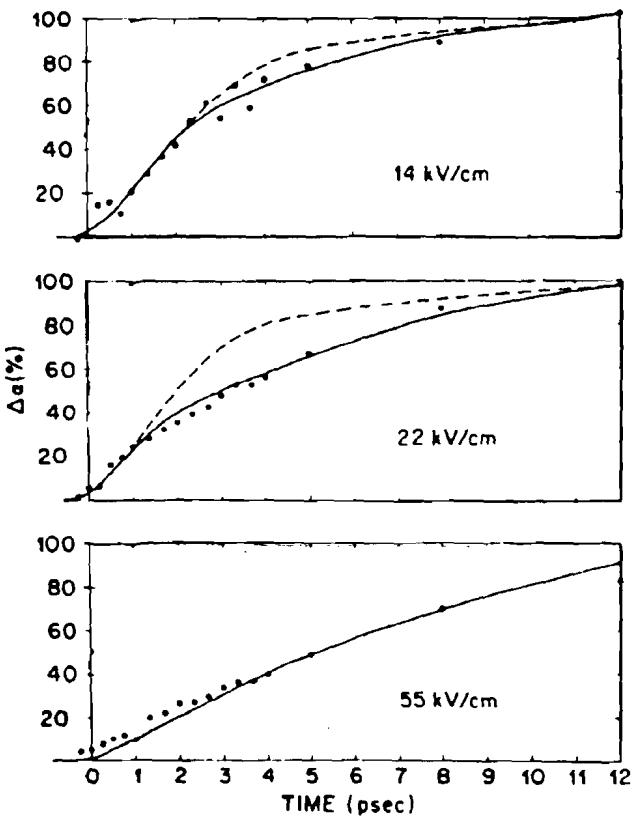

Fig 3.1.2 Total absorbance change for three applied fields. The dotted lines are a one-velocity fit of eq. [3.1.1]; the solid lines are a two-velocity fit [47].

result versus pump/probe delay, as shown in Fig. 3.1.2.

To interpret the data a constant hole velocity of $1x10^7$cm/sec was assumed. The dashed curves in Fig. 3.1.2 are the best fit of the theory assuming a constant electron velocity. The constant-velocity model cannot account for the data at 14 and 22kV/cm. The solid lines are fits of the theory assuming a two-velocity model for the electrons, i.e., a high velocity at short times and a lower (equilibrium) velocity at longer times. The fit for the 14kV/cm data yields an electron velocity of $3x10^7$cm/sec for t<2.5pS and a lower velocity (presumably ~$1x10^7$cm/sec) for longer times. For E=22kV/cm the fit yields $v_e=4.4x10^7$cm/sec for t<1.1pS and $v_e=1.2x10^7$cm/sec for longer times. For the highest field, a very large velocity overshoot is expected, yet the data may be fit by the single-velocity model with $v_e=1.3x10^7$cm/sec. Shank et. al. state that at this extreme field the overshoot takes place so fast that it cannot be resolved in their measurement. The authors further state that the above results are consistent with Monte Carlo calculations, however they do not present those calculations for comparison with their results.

Clearly, evidence of a higher electron velocity at short times has been obtained, but this experiment cannot yield detailed information about the transient drift velocity. In their introduction, Shank et. al. state "a direct measurement of carrier velocity with picosecond resolution would require special transmission line structures and careful contact fabrication techniques." The presumption is that such an experiment would be difficult or impossible to conduct, hence all-optical techniques are preferable. In fact, we maintain that with proper design of transmission lines and contacts significant results may be obtained with electro-optic sampling of voltage transients, as will be discussed in detail in Chapter 4.

3.2 Coherent Time-Domain Infrared Spectroscopy

In conjunction with optical transmission measurements discussed in the previous section, reflectivity measurements can produce useful information about semiconductor carrier dynamics. A novel adaptation of the standard optical reflectivity technique is the use of subpicosecond electrical pulses produced by optical rectification of short laser pulses [51]. This technique allows measurement of the incident and reflected electromagnetic pulses off the face of a semiconductor crystal, and the transient conductivity (and hence mobility) of carriers in the semiconductor may be derived. Details of this approach will be discussed below.

In an electro-optic medium, an applied electric field will rotate the polarization of the molecules and induce a birefringence in the material that can be detected as rotation of polarized light passing through the material. This is the linear electro-optic effect and is the basis for electro-optic sampling, as will be discussed in Chapter 4. In the inverse manner, if a subpicosecond laser pulse is focussed into such a medium a transient dipole moment will be generated which will in turn radiate electromagnetic waves in the far infrared. Due to the additional contribution to the low frequency dielectric response from the infrared lattice vibrations, the velocity of the source exceeds the radiation velocity. This is the condition necessary for Cerenkov radiation; the radiation is emitted in a cone whose angle is determined by the ratio of the velocities. Fig. 3.2.1 illustrates a geometry in which an EM pulse was generated with one laser pulse and measured (through the linear electro-optic effect) using a synchronized probe pulse. The measured electrical pulse, along with its Fourier transform, is shown in Fig. 3.2.2 [52]. This generation technique allows for production of very broad-band EM pulses with frequencies up to several THz (the upper limit in this case is determined by a lattice resonance in lithium tantalate at 6THz).

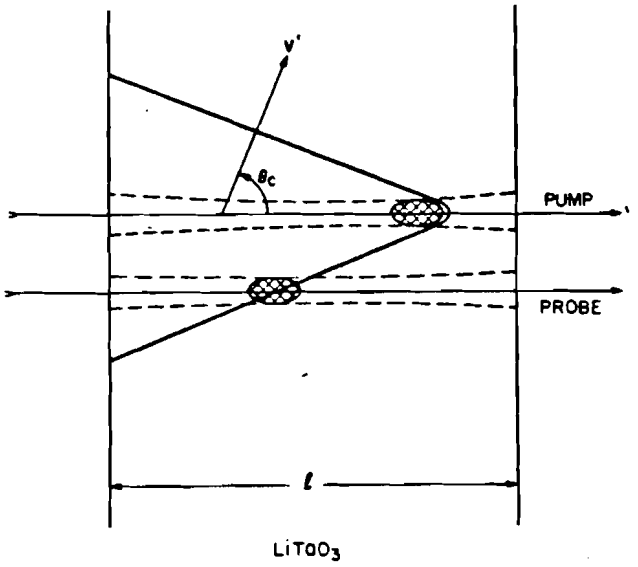

Fig. 3.2.1 Geometry for measuring the EM pulse generated with the inverse electro-optic effect in lithium tantalate [52].

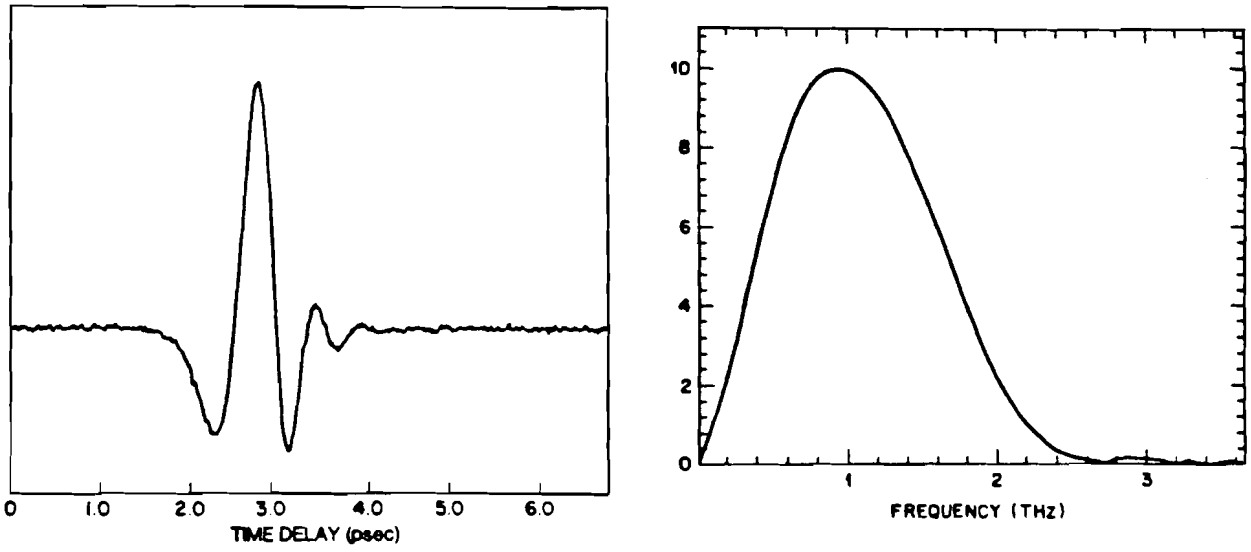

Fig. 3.2.2 EM pulse generated in the geometry of Fig. 3.2.1 and its Fourier transform [52].

In the initial application of this technique, the EM pulses were used to measure the complex dielectric response of various semiconductors at high frequencies [52]. The geometry for this experiment is shown in Fig. 3.2.3. In principle, since the probe

beam measures both the incident and, at a later time, the reflected waveforms, all of the information necessary to compute the real and imaginary parts of the dielectric response function are at hand. However, because the EM waves must propagate through a small but significant distance of lithium tantalate, some distortion and attenuation occurs and the absolute phase information is lost. In order to overcome this difficulty, it is necessary to perform an identical measurement on a reference sample for which the dielectric function is well known. Auston and Cheung chose to use a gold film for the reference. Measured waveforms for the gold sample and for a sample of doped germanium are shown in Fig. 3.2.4. The incident pulse peaks at 1.6ps and the reflected pulse arrives approximately 3ps later. That the reflected waveforms are very different for the two materials is proof that the permitivities are fundamentally different, as expected.

The dielectric permitivity for doped germanium, derived from the

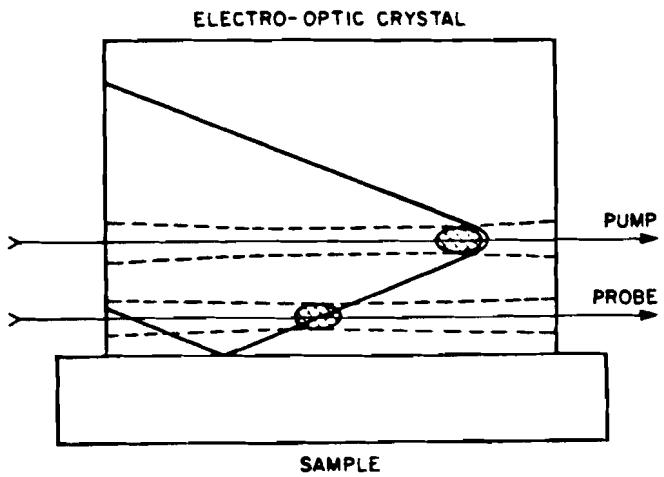

Fig. 3.2.3 Geometry for measuring incident and reflected EM pulses off of a test sample [52].

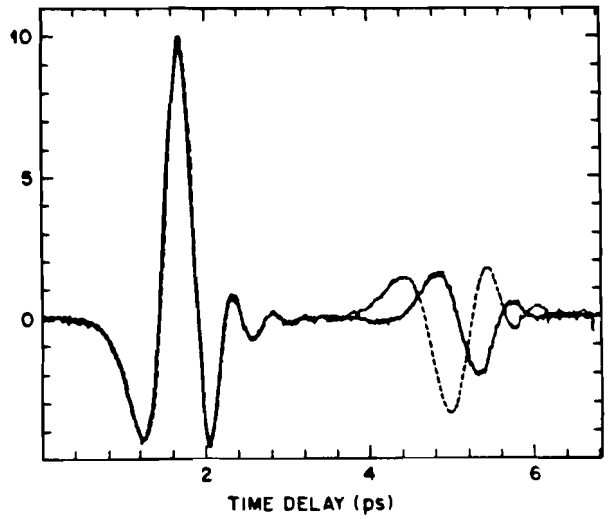

Fig. 3.2.4 Incident and reflected EM pulses off a gold reference sample (dotted curve) and a doped germanium sample [52].

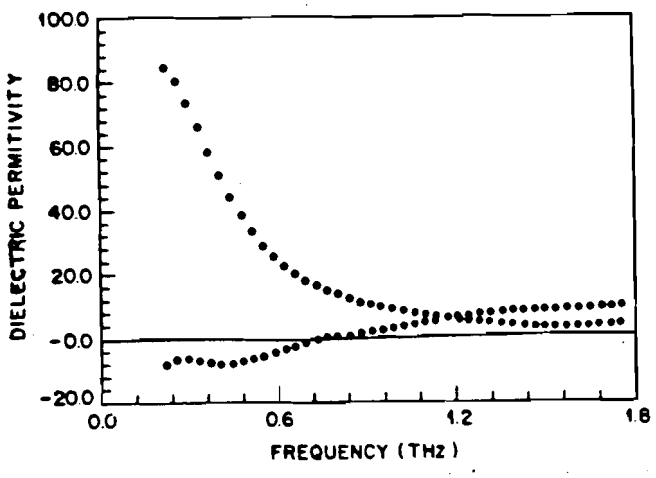

Fig 3.2.5 Real (lower curve) and imaginary (upper curve) parts of the complex permitivity for doped germanium, derived from the data in Fig. 3.2.4 [52].

experimental reflectivity, is shown in Fig. 3.2.5. The permitivity behaves as expected for a solid state plasma, i.e.

$$\varepsilon(\omega) = \varepsilon_s - \frac{n e^2}{m^*} \frac{1}{\omega(\omega + \frac{i}{\tau})} \qquad [3.2.1]$$

where ε_s is the static dielectric constant and τ is the momentum relaxation time. The plasma frequency (the point at which the real part of the permitivity goes to zero) is experimentally determined to be 0.75THz, which yields a momentum relaxation time of 225fs in good agreement with theory.

In order to study hot electron effects with this technique it is necessary to introduce hot carriers into the semiconductor on a short time scale, which is easily accomplished via photoexcitation with a short laser pulse [53]. The geometry, shown

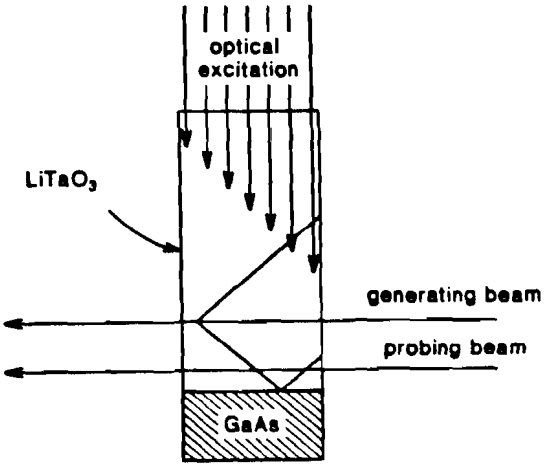

Fig. 3.2.6 Geometry for studying transient conductivity of carriers optically excited in GaAs [53].

in Fig. 3.2.6, is identical to that described above in all other respects. The photoexcitation, generation, and probe beams are all derived from a single amplified dye laser pulse train. The sample investigated consisted of undoped MBE GaAs sandwiched between AlGaAs layers. The photoexcitation of 625nm creates electrons with 500meV of excess energy which eventually cool down to the Γ band edge.

Experimental results are shown in Fig 3.2.7, with the time delay t_{probe} between generation of the EM pulse and probe of the reflected pulse on the horizontal axis and the time delay T_{EX} between photoexcitation and probe on the vertical axis. The curves for $T_{EX}<0$ show the reflectivity of intrinsic GaAs. Note the change of phase of the waveform at t_{probe}~1.5ps as T_{EX} increases; this is evidence of the insulator-to-conductor transition that occurs upon photoexcitation.

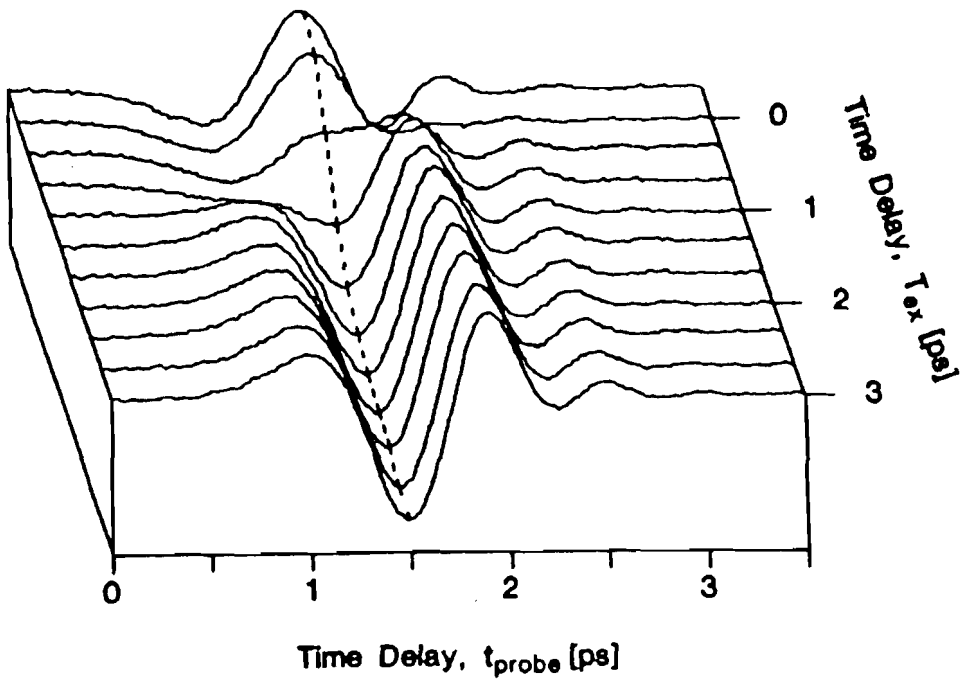

Fig. 3.2.7 Reflected EM waveforms off of photoexcited GaAs. T_{EX} is the photoexcitation/probe delay and t_{probe} is the EM generation/probe delay [53].

Information about the transient mobility of the carriers may be derived from the data as follows: the reflected EM pulse is equal to:

$$E_r(t) = r_0 E_i(t) - Y^{-1} J_s(t) \qquad [3.2.2]$$

$$Y = \left(\frac{\varepsilon_0}{\mu_0}\right)^{\frac{1}{2}} \{ \sqrt{\varepsilon_1} \cos\theta_i + \sqrt{\varepsilon_2} \cos\theta_t \} \qquad [3.2.3]$$

$$J_s(t) = \sigma(t)E(t) = \sigma(t)\{ E_i(t) + E_r(t) \} \qquad [3.2.4]$$

where r_0 is the reflection coefficient of the intrinsic GaAs, J_s is the photoexcited sheet carrier density, ε_1 and ε_2 are the dielectric constants of lithium tantalate and GaAs, and $\sigma(t)$ is the transient conductivity. The above expressions yield equations for the reflected EM field, the conductivity, and the mobility as a function of the transient reflectivity:

$$E_r = \left\{ r_0 - (1 - r_0)\frac{\sigma_s}{Y + \sigma_s} \right\} E_i = r(t)E_i(t) \qquad [3.2.5]$$

$$\sigma_s(t) = Y\frac{r_0 - r(t)}{1 + r(t)} \qquad [3.2.6]$$

$$\mu(t) = \frac{\sigma_s(t)[1 + r(t)]}{n_s q} = \frac{Y[r_0 - r(t)]}{n_s q} \qquad [3.2.7]$$

The resultant mobility curves are shown in Fig. 3.2.8 for three different excitation densities. In all three cases the mobility starts out very low (~500cm^2/Vsec) and takes several picoseconds to increase to its equilibrium value. The initial low mobility is interpreted as that of electrons in the low-mobility L valley; i.e. even though electrons are photoexcited into the Γ valley at t=0 they scatter into the L valley within the first 100 femtoseconds. The long risetime of the mobility is attributed to gradual scattering of the electrons back into the Γ valley and cooling to the band edge through LO phonon emission. This is hot carrier relaxation and will be discussed in detail in Chapter 5. The time scale of several picoseconds is consistent with values obtained from luminescence and transient absorption measurements. The dependence of the risetime on carrier density is presumably due to hot phonon effects.

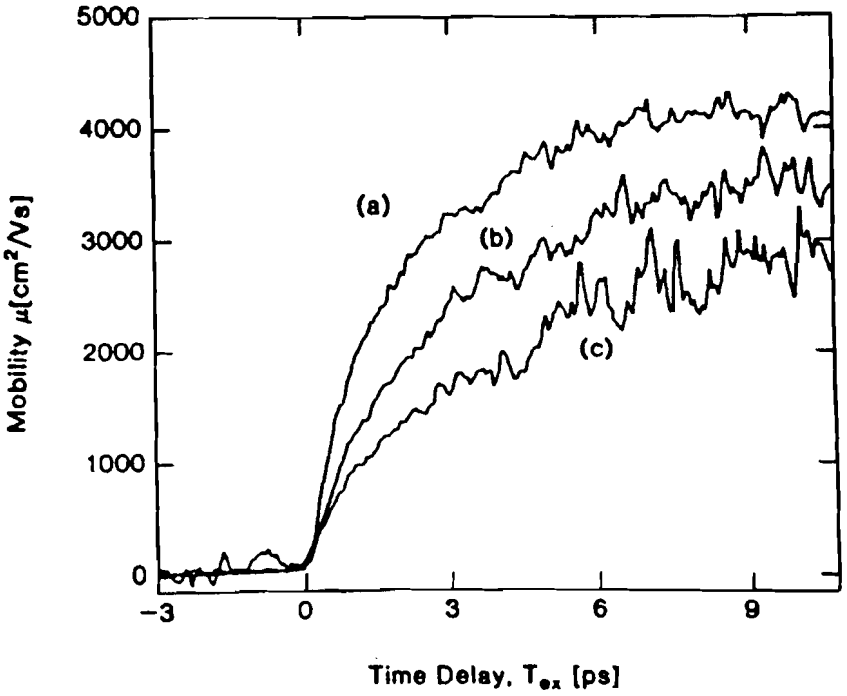

Fig. 3.2.8 Time dependence of the mobility derived from the transient reflectivity data. a)n=$5x10^{17}cm^{-3}$, b)n=$5x10^{18}cm^{-3}$, c)n=$1.2x10^{19}cm^{-3}$ [53].

Though this technique is a potentially powerful tool for studying transient mobility under a variety of experimental conditions, to date it has only been successfully applied to the measurement of hot electron relaxation. One way to study carrier heating effects is to increase the amplitude of the incident EM wave to levels where non-linear response is expected (E_i>3.5kV/cm). An attempt to do this was recently reported [54] with a peak field of 7kV/cm; however, no non-linear effects were observed. This may be due to the fact that E_i is a bipolar field, so that the time-averaged field experienced by the carriers is low. An improved approach would allow for a DC or slowly varying electric field on the sample, perhaps by adding appropriate contacts to the sample geometry.

3.3 AC Conductivity Measurement

One might well expect that a strongly time-dependent phenomenon such as velocity overshoot would have a corresponding characteristic signature in the frequency domain. This is indeed the case, as has been shown by a number of authors [55-57]. To illustrate the connection between time and frequency dependent behavior, the analysis of Teitel and Wilkins [57] will be followed here.

A frequently used approach to describe time-dependent electron velocity and energy is the use of moment equations within the context of the relaxation approximation:

$$\frac{dv}{dt} = \frac{qE}{m} - v\Gamma_m(\varepsilon) \qquad [3.3.1]$$

$$\frac{d\varepsilon}{dt} = qEv - (\varepsilon - \varepsilon_l)\Gamma_e(\varepsilon) \qquad [3.3.2]$$

where ε_l is the equilibrium lattice energy and Γ_m and Γ_e are the momentum and energy relaxation rates which govern the system's approach to equilibrium. Strictly speaking, such an approach is only valid for single-valley conduction bands, but the technique may be extended to multiple valleys by writing down similar equations for each valley and coupling the equations together [28].

The steady-state solutions to the above equations are

$$v_0(E) = \frac{qE}{m\Gamma_m(E)} \qquad \varepsilon_0(E) = \frac{qE_0}{\Gamma_e(E)} + \varepsilon_l \qquad [3.3.3]$$

Hence the relaxation rates which govern the transient behavior are completely determined by the steady-state behavior of $v_0(E)$ and $\varepsilon_0(E)$.

Now consider the response of the system with an applied DC electric field E_0 and an additional small time-dependent perturbation $E_1(t)$ (such as is the usual case in an AC conductivity measurement:

$$E(t) = E_0 + E_1(t) \qquad [3.3.4]$$

$$v(t) = v_0 + v_1(t) \qquad [3.3.5]$$

$$\varepsilon(t) = \varepsilon_0 + \varepsilon_1(t) \qquad [3.3.6]$$

The balance equations may now be written in dimensionless form as

$$\frac{d\tilde{v}}{d\tilde{t}} = \frac{E_1}{E_0} - G_m \tilde{\varepsilon} \qquad [3.3.7]$$

$$\frac{d\tilde{\varepsilon}}{d\tilde{t}} = \frac{E_1}{E_0} + \tilde{v} - G_e \tilde{\varepsilon} \qquad [3.3.8]$$

$$\tilde{v} \equiv \frac{v_1}{v_0} \qquad \tilde{\varepsilon} \equiv \frac{\varepsilon_1 \Gamma_{m0}}{(\varepsilon_0 - \varepsilon_1)\Gamma_{e0}} \qquad [3.3.9]$$

$$\tilde{t} \equiv \Gamma_{m0} t \qquad \Gamma_0 \equiv \Gamma(\varepsilon_0) \qquad [3.3.10]$$

The only two unknowns, aside from Γ_{m0}, in [3.3.7] and [3.3.8] are

$$G_m \equiv (\varepsilon_0 - \varepsilon_1) \frac{\Gamma_{e0}}{\Gamma_{m0}^2} \left(\frac{d\Gamma_m}{d\varepsilon} \right)_0 \qquad [3.3.11]$$

$$G_e \equiv \frac{1}{\Gamma_{m0}} \left\{ \frac{d(\varepsilon - \varepsilon_1)\Gamma_e}{d\varepsilon} \right\}_0 \qquad [3.3.12]$$

If the electric field is purely oscillatory, i.e. has the form $\exp(i\omega t)$, then the AC conductivity may be written as

$$\frac{\sigma(\omega, E_0)}{\sigma_{DC}(E_0)} = \frac{G_e - G_m + i\tilde{\omega}}{(G_e + i\tilde{\omega})(1 + i\tilde{\omega}) + G_m} \qquad [3.3.13]$$

$$\tilde{\omega} \equiv \frac{\omega}{\Gamma_{mo}} \qquad \sigma_{DC}(E) \equiv \frac{n q v_0}{E} \qquad [3.3.14]$$

The behavior of the real part of the AC conductivity as a function of frequency, for

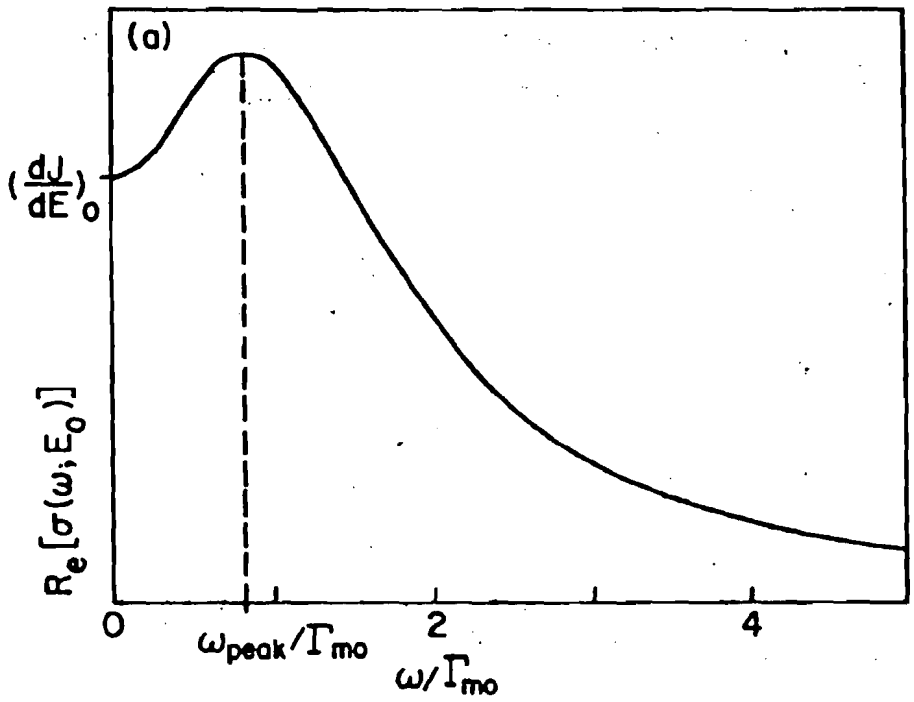

Fig. 3.3.1 Calculated dependence of the AC conductivity on frequency for conditions of small-signal velocity overshoot [57].

typical values of G_e and G_m, is shown in Fig. 3.3.1. An important feature of the conductivity, which will be discussed below, is the maximum at non-zero frequency.

Three measurements are necessary to calculate the three unknowns in the above equations. Measurement of the DC conductivity determines Γ_{m0}:

$$\sigma_{DC}(E_0) = \frac{n q^2}{m \Gamma_{m0}} \qquad [3.3.15]$$

Measurement of the slope of the IV curve (i.e. AC conductivity in the zero-frequency limit) yields the ratio of G_e and G_m:

$$\frac{\sigma(\omega=0, E_0)}{\sigma_{DC}(E_0)} = \left[\frac{dJ/dE}{J/E}\right]_0 = \frac{G_e - G_m}{G_e + G_m} \qquad [3.3.16]$$

Teitel and Wilkins show that a measurement of the peak AC conductivity $Re[\sigma(\omega_{peak}, E0)]$ is sufficient to determine G_e and, with the above expressions,

completely determine the behavior of the system.

The transient velocity is related to the AC conductivity through the transform

$$v_1(t) = \frac{E_1}{nq}\int_{-\infty}^{\infty}\frac{d\omega}{2\pi i}\frac{\exp(i\omega t)}{\omega - i\eta}\ \mu(\omega, E_0) \qquad [3.3.17]$$

The behavior of $v_1(t)$ is therefore completely determined by the poles of $\sigma(\omega)$ and its residues. Teitel and Wilkins draw the important conclusion that " observation of a peak AC conductivity at a non-zero frequency is a sufficient condition for velocity overshoot under identical DC conditions ."

Clearly high-frequency AC conductivity measurements can yield important information about velocity transients. The difficulty in such experiments is that very broad-band high-frequency sources are needed. Allen et. al. [58] have performed measurements of AC conductivity covering the range of 100 to 1200GHz by observing the transmission of far-IR radiation generated using a black-body swept-frequency source. The initial experiments were carried out on a Si MOSFET sample at T=1.5K with an applied DC field of 168V/cm. The measured change in transmission is related to the conductivity through

$$\Delta\sigma(\omega) = \frac{1}{2}\frac{\Delta T}{T}(Y_0 + Y_{Si} + Y_G) \qquad [3.3.17]$$

where Y_0, Y_{Si}, and Y_G are the wave admittances of free space, the Si substrate, and the resistive gate. The deduced AC conductivity versus frequency is shown in Fig. 3.3.2 . Also shown in the figure is the measured DC conductivity, and the dotted line is a fit to theory similar to that discussed above. Even though there is no data for the critical interval between DC and 100GHz, one can conclude, based on the proof of Teitel and Wilkins, that because the AC conductivity is higher than the DC conductivity, velocity overshoot is taking place in the sample. If the frequency-

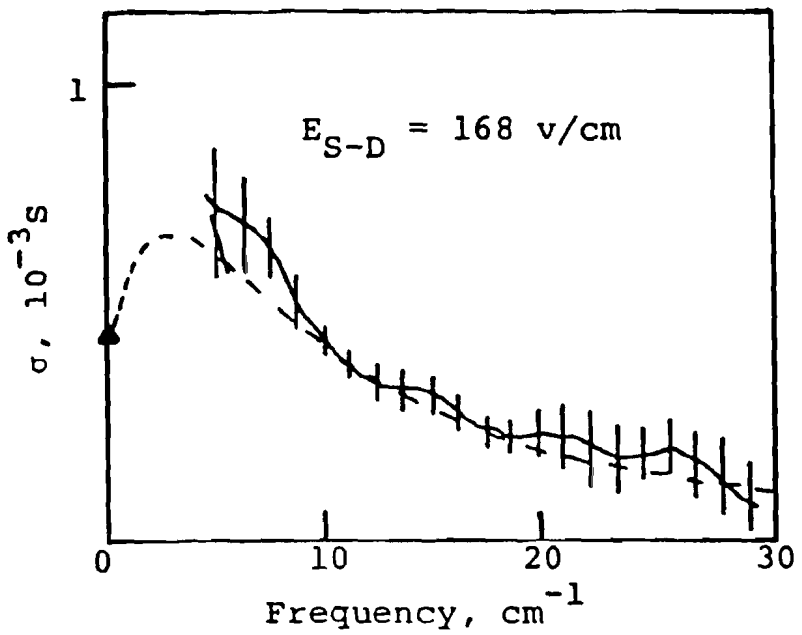

Fig. 3.3.2 Measured behavior of the high-frequency AC conductivity in Si [58]. The arrow indicates the value for the DC conductivity and the dotted line is the extrapolated fit to theory.

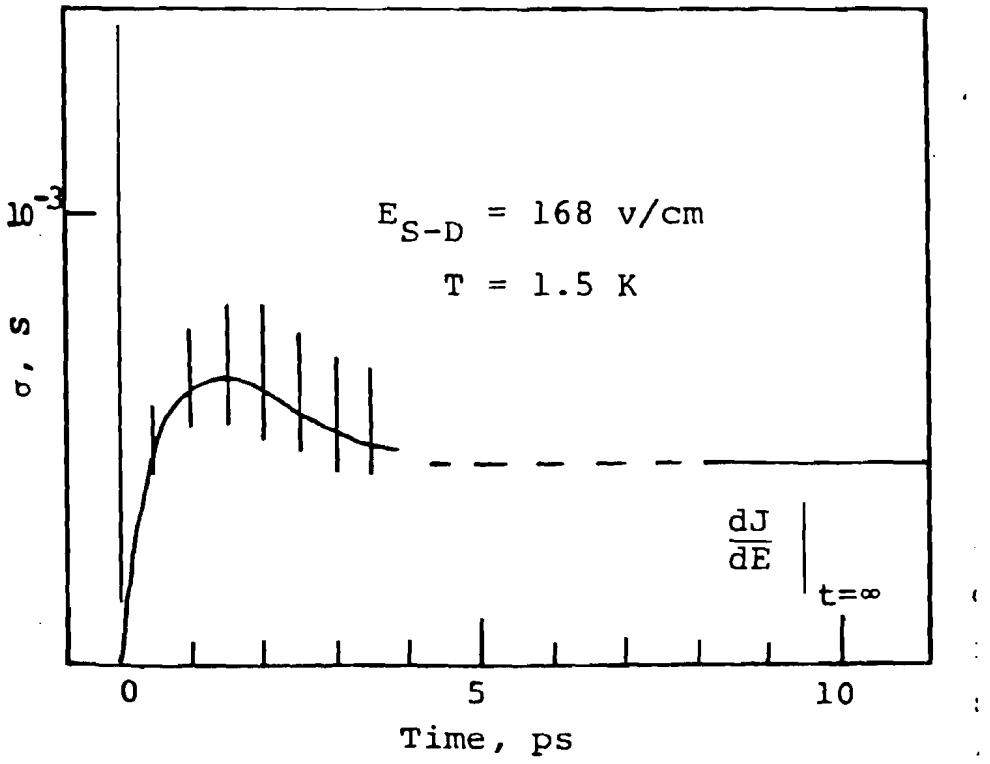

Fig 3.3.3 Time-domain conductivity for Si derived from AC conductivity data [58].

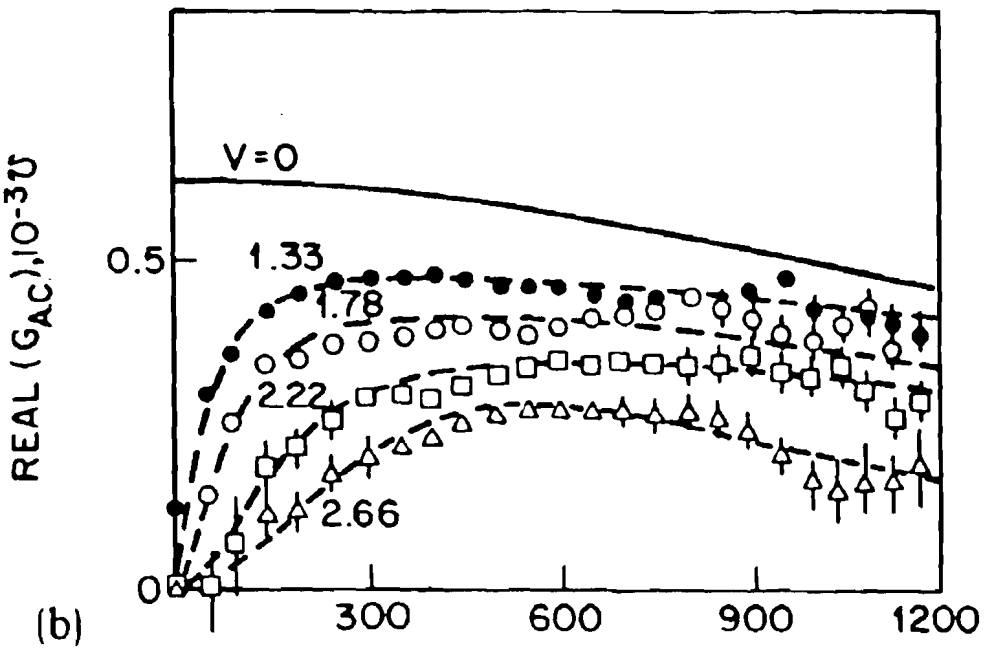

Fig. 3.3.4 Measured GaAs AC conductivity for various applied electric fields [59].

domain data is transformed into the time domain, the conductivity as a function of time is obtained (Fig. 3.3.3). There is some evidence of a slight overshoot at 1.5ps, but interpretation of the data is difficult because of its discrete nature and large error bars.

In a subsequent experiment Allen et. al. [59] measured the far-IR transmissivity of a 2-dimensional array of n^+-n-n^+ GaAs diodes. The measured change in conductance versus frequency and applied field is shown in Fig. 3.3.4. At the highest DC bias of 2.66V (corresponding to a field of 1.33kV/cm) a broad maximum centered at approximately 600GHz is apparent. This is interpreted as small-signal velocity overshoot in the frequency domain. In this case no attempt was made to transform the data into the time domain.

In this section the connection between velocity transients and frequency domain conductivity was developed, and it was shown that a maximum AC

conductivity for non-zero frequency is evidence of velocity overshoot. Some experiments have been performed in the frequency domain which indicate a small-signal velocity overshoot. The primary difficulty in these types of experiments is a practical one, that of being able to measure conductivity over an extremely broad band of high frequencies. As will be discussed in Chapter 4, time-domain sampling techniques now have the temporal resolution to resolve conductivity transients on a subpicosecond time scale, which eliminates the necessity of transforming AC measurements into the time domain.

3.4 DC I-V Characterization of n^+-n-n^+ Devices

A primary application of velocity overshoot has been in the area of short-channel devices. It is often assumed that if the channel length in the device is shorter than the electron mean free path, then the electrons will experience few scattering events, their corresponding transit times will be fast, and the speed of the device (which is intrinsically limited by the transit time) will be enhanced. The simplest device of this type is the two-terminal n^+-n-n^+ structure, shown in Fig. 3.4.1, which was originally developed as a current limiter [60,61]. When a voltage is applied across the device electrons are injected at the cathode, accelerate across the n-type gap, and are collected at the anode. Several authors have attempted to derive information about the average electron velocity during transit by analyzing the DC I-V characteristics of the device as a function of channel length and temperature [62-66]. The representative results of Eastman et. el. [63] and Laval [65] will be discussed below.

According to an analysis by Shur and Eastman [64], the current-voltage characteristic of the device should have a square-root dependence at low fields

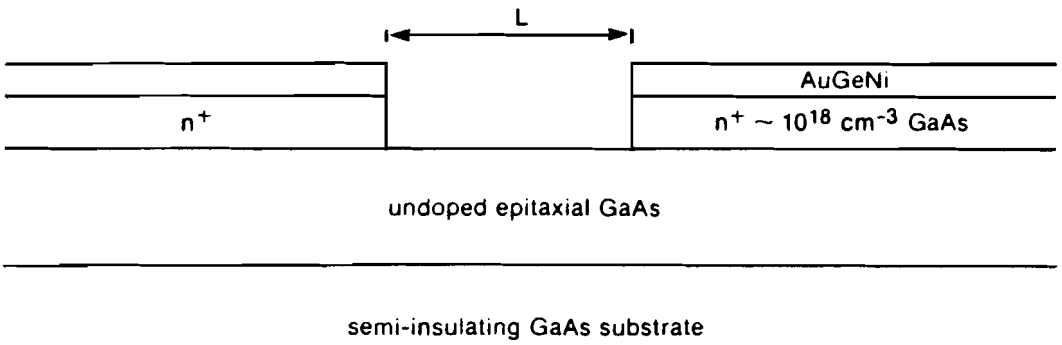

Fig. 3.4.1 Geometry of the n^+-n-n^+ structure.

changing to a 3/2-power-law dependence in the high-field "ballistic" regime. An experimental IV curve for a device with a 0.4um long channel is shown in Fig. 3.4.2. The dotted lines are the asymptotic 1/2 and 3/2 power laws and the open circles are the experimental data. The solid line on which most of the data points lie is the theory of Shur and Eastman. Also shown is the prediction for the current if the electrons were moving at the saturation velocity. Eastman et. al. conclude that because the IV characteristic agrees with the theory and the magnitude of the current is significantly higher than the prediction for saturated velocity, then the current measured was due to enhanced velocities and ballistic transport. The deviation of the data from the theoretical curve above 0.5V is interpreted as the onset of intervalley transfer. These conclusions have been challenged by several authors; the details of their arguments will be discussed at the end of this section.

In a similar experiment but using a different analysis Laval et. al. [65] have studied the IV characteristics of photoexcited current in a n^+-n-n^+ structure. In this case the n-type channel was undoped and the transport electrons were excited with a CW laser source. According to the analysis used the photocurrent is inversely proportional to the transit time τ_n and hence proportional to the average electron

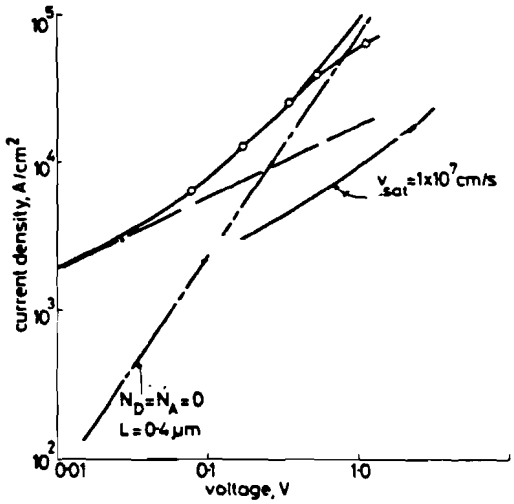

Fig. 3.4.2 Experimental IV characteristic for a n^+-n-n^+ device. The dotted lines are the asymptotic 1/2 and 3/2 power laws; the solid line is the theory of Eastman and Shur. Also shown is the prediction for saturated-velocity current flow [63].

transit:

$$I_{photo} = \frac{q\,n\,S\,L}{\tau_n} = q\,n\,S\,v_{ave} \qquad [3.4.1]$$

where S is the cross-sectional area of the device and L is the channel length. In order to understand how the IV curve is expected to change with channel length, it is necessary to plot the average electron drift velocity versus field for different channel lengths (Fig. 3.4.3), which has been derived from Monte Carlo calculations of the drift velocity versus time [37]. For long channel lengths, the velocity-field curve is reproduced, while as the channel length is reduced the device operates more and more in the "quasi-ballistic" regime with significantly enhance velocities. In the limit of extremely short channels, the "ballistic limit", the electrons will experience few or no collisions and the average velocity will be vary linearly with field.

Fig. 3.4.4 shows Laval's experimental IV curves for a very long channel (L=385um) device. As expected according to the analysis above, the response exhibits negative differential resistance and resembles the standard velocity-field curve

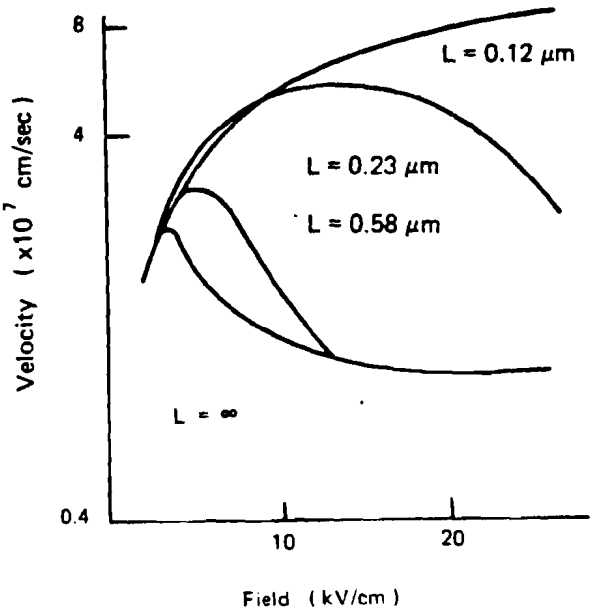

Fig. 3.4.3 Average electron drift velocity during a transit, derived from Monte Carlo calculations, for various channel lengths [37].

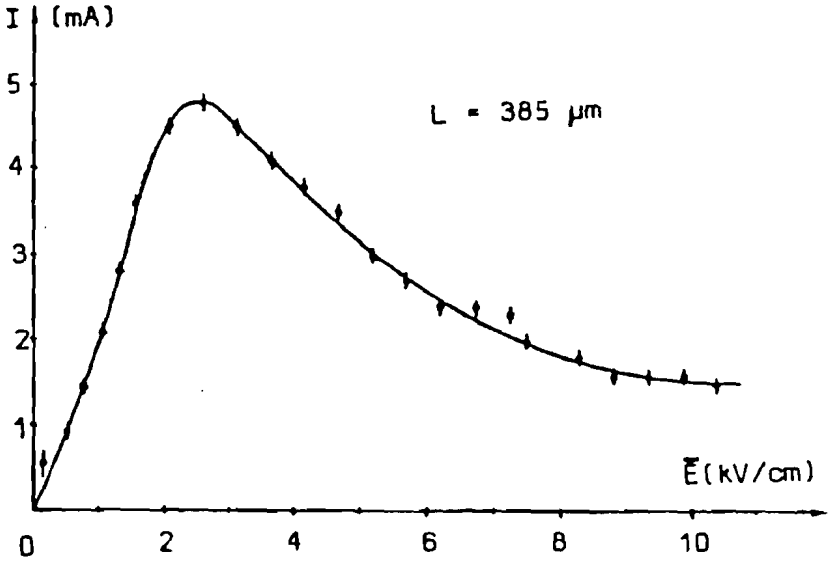

Fig. 3.4.4 Photoconductive IV characteristic for a long-channel (L=385um) n^+-n-n^+ device [65].

for GaAs.

The response for short-channel devices, shown in Fig. 3.4.5, is quite

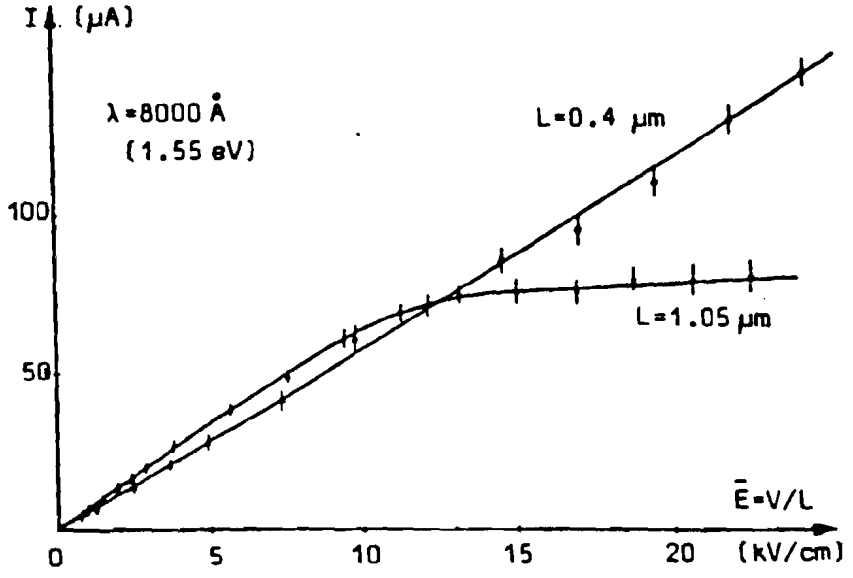

Fig. 3.4.5 Photoconductive IV characteristics for short-channel n^+-n-n^+ devices [65].

different. For the intermediate case of L=1.05um (compare with the curve for L=0.23um in Fig. 3.4.3) the photocurrent saturates, which is attributed to the onset of intervalley transfer and a subsequent reduction of electron mobility. For the shortest channel with L=0.4um the IV characteristic is linear and Laval argues that the device is operating in the purely ballistic regime. Laval does not attempt to explain the discrepancy in length scales between the experimental results (Fig. 3.4.5) and the theoretical predictions (Fig. 3.4.4).

As stated earlier in this section, several authors disagree with the interpretation of these DC experiments. Barker et. al. [67] point out that the simple mean-free-path analysis of Shur and Eastman does not take into account the effects of surface scattering, non-normal electron injection angles, or quantum-mechanical reflections at the contacts. In addition, they argue that in a device in which the internal field is highly non-uniform due to the large steps in doping profile at the contacts the current

is completely determined by space-charge limited flow [67]. In other words, at high field the space charge is depleted and the current is governed by injection at the contacts rather than ballistic transport in the channel. Cook and Frey [68] have examined a number of relaxation time models which included diffusion and space-charge effects, and have observed a variety of non-linear IV characteristics which can be attributed to contact effects or details of the model and are unrelated to ballistic effects. Finally, in a very extensive Monte Carlo study of the evolution of the distribution function of electrons during transit, Baranger and Wilkins [69] show that even though significant numbers of electrons may achieve very high velocities in the channel, the current is determined by boundary effects and therefore is not a sensitive probe of ballistic structure. Clearly, more sophisticated techniques must be developed, such as the energy spectroscopy technique, which measures the energy distribution of electrons swept out of the channel. This technique is the subject of the following section.

3.5 Spectroscopy of Hot Electron Transistors

One practical motivation for studying velocity overshoot and "ballistic" transport is that most semiconductor device speeds are intrinsically limited by the transit time of electrons across the device. This being the case, many devices are designed with very short and/or high-purity transit regions to reduce scattering and increase the net electron velocity. Another way of approaching the question of scattering is this: if electrons are injected with momentum k_i at one end of the device, what does the momentum distribution look like when the electrons leave the opposite end of the device? If there is little or no scattering the momentum distribution will have a sharp peak at the initial $\vec{k}_i$ value; if strong scattering is present the electrons will

have thermalized into a Fermi distribution. This is the concept behind the operation of the Hot Electron Transistor [70,71] which will be described below.

A typical HET, shown in Fig. 3.5.1, is a planar device which consists of an n^+n emitter, a heavily doped transit region sandwiched between two triangular barriers, and an n-type collector region. The device described here is based on the

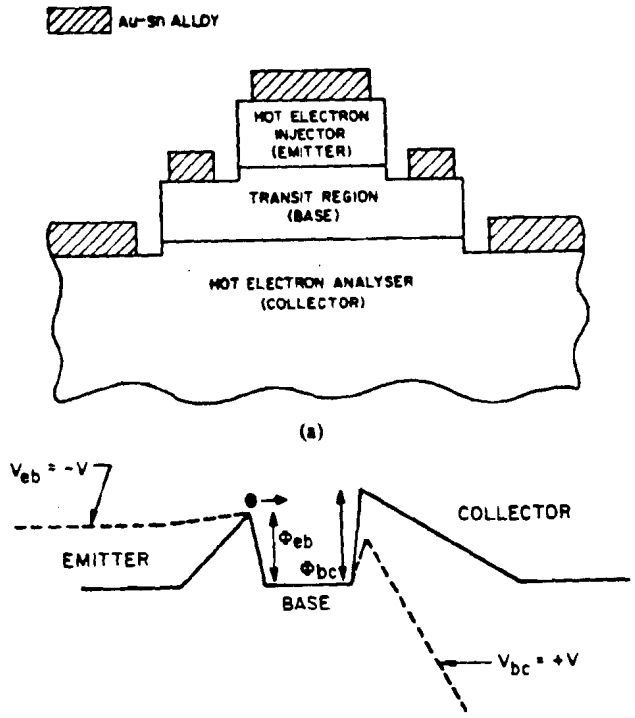

Fig. 3.5.1 Geometry and band structure for a typical Hot Electron Transistor (HET) [71].

GaAs/AlGaAs material system [71]; other devices have also been fabricated using InGaAs/InAlAs [72]. Transport through the device may be controlled in two ways. The emitter bias V_{eb} controls the emitter-base barrier height Φ_{eb} and hence determines the incident momentum of the injected electrons. This is often referred to as a hot electron injector. On the other hand, the collector bias V_{bc} governs the base-collector barrier height Φ_{bc} and therefore serves as an analyzer of the momentum distribution of the electrons leaving the base. It follows that if the collector current as a function of collector bias is measured the full momentum distribution may be obtained.

A typical experiment consists of measuring the momentum distribution for a series of increasingly long base transit regions to obtain information about the effective length (time) scale for scattering. The analysis is as follows: only electrons whose momentum $k_\perp$ is perpendicular to the base-collector barrier Φ_{bc} will cross the barrier and be collected. The total current is the integral over all electrons with the proper momentum [71]:

$$I_c = -\left(\frac{q}{m^*}\right) \int_{k_\perp^0}^{\infty} k_\perp \, n(k_\perp) \, dk_\perp \qquad [3.5.1]$$

$$k_\perp^0 = (2 m^* \Phi_{bc})^{\frac{1}{2}} \qquad [3.5.2]$$

The derivative with respect to V_{bc} is equal to :

$$\frac{dI_c}{dV_{bc}} = \frac{q}{m^*} \frac{d\Phi_{bc}}{dV_{bc}} \frac{dk_\perp^0}{d\Phi_{bc}} \, n(k_\perp^0) \, k_\perp^0 \qquad [3.5.3]$$

$$\Phi_{bc} \approx V_{bc} \quad \Rightarrow \quad \frac{dI_c}{dV_{bc}} \approx n(k_\perp^0) \qquad [3.5.4]$$

Therefore by differentiating the collector current I_c with respect to V_{bc} the momentum distribution function at the base-collector junction is obtained.

Some experimental results by Hayes and Levi [71] are shown in Fig. 3.5.2. The momentum distribution as a function of energy and base region width is plotted. Also shown are the incident electron energies and the Fermi energies (at the extreme right of each plot). The change in the spectra with increasing base width is an indication of strong scattering. At the shortest base width of 650Å there is a broad peak of electrons around the initial energy and a sharper peak near the Fermi energy. Even for this short a transit region many electrons have scattered out of the initial state. For long transit regions all of the electrons have scattered out of the initial state

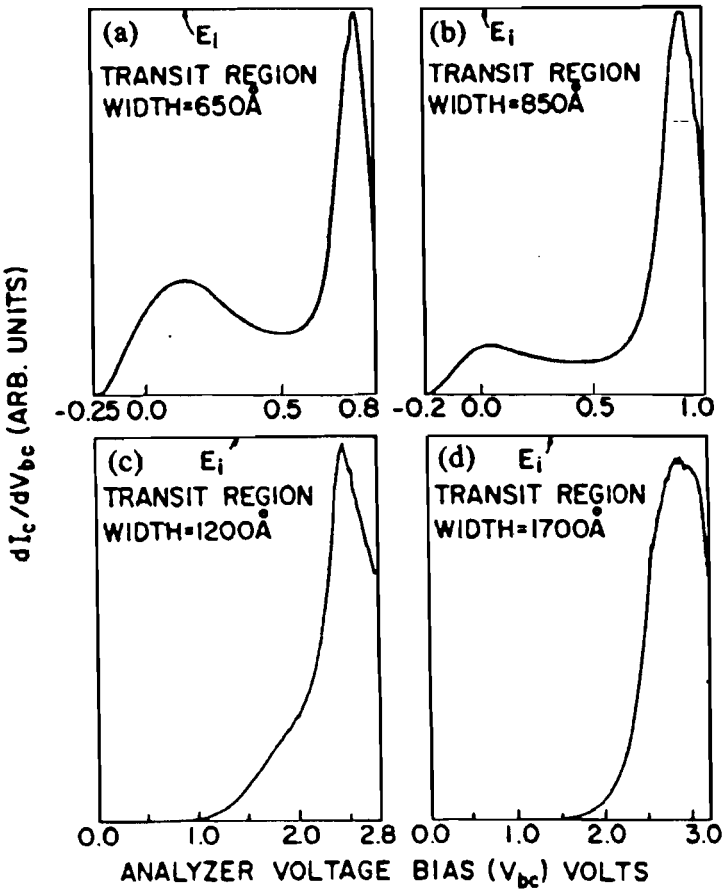

Fig. 3.5.2 Measured energy spectra of carriers swept out of the HET base for various base widths. For each curve the injection energy is indicated by an arrow and the Fermi energy is at the right extreme of the plot [71].

and the distribution is thermalized.

Several Monte Carlo studies of transport in these structures have recently been published [73-77]. Along with the usual impurity,carrier-carrier, and carrier-phonon scattering mechanisms two new mechanisms, due to the heavy doping of the base region, must be included in the calculation. The first is scattering of injected electrons off of electrons in the Fermi sea in the base, which will tend to cool the injected distribution and heat the Fermi distribution. The second is the collective oscillatory mode of the n^+ gas, referred to as the plasmon mode [78,79]. For a doping of $\sim 10^{18}/cm^3$ the plasmon mode energy is very close to that of the LO phonons, so that

the plasmons and phonons must be treated as a coupled system. Long et. al. [73] have performed the simulation with all of the above mechanisms included and have also modeled the particular experimental conditions of Hayes and Levi discussed above. The calculated momentum distribution is shown in Fig. 3.5.3 along with the experimental results for the shortest base width. The general features of the calculation are in good agreement with the experimental results.

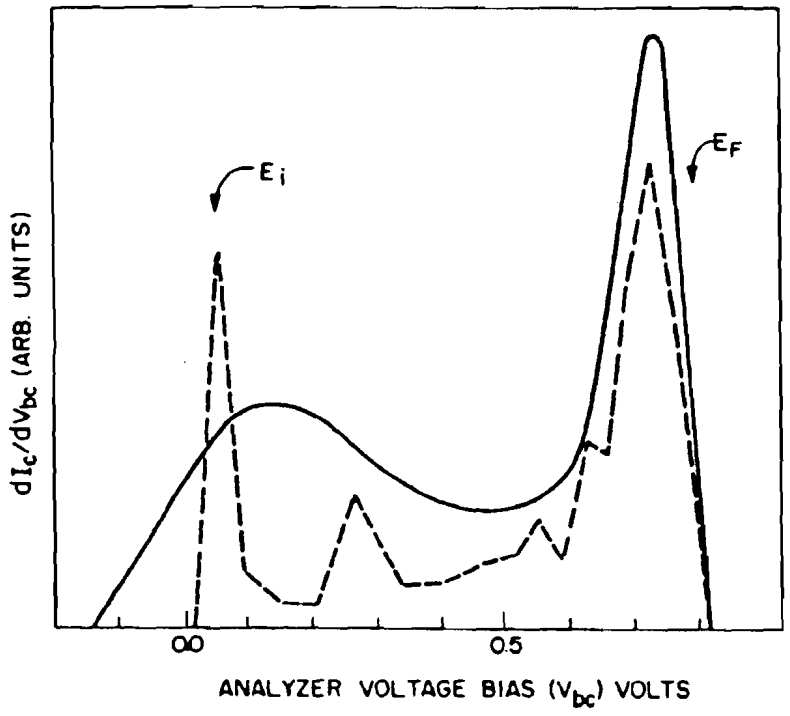

Fig. 3.5.3 Monte Carlo calculation (dotted line) and measured energy spectrum (solid line) for electrons transiting a 650Å base region [73].

A different analysis of the HET operation can yield information about <u>where</u> the injected electrons are scattering to, i.e., intervalley transfer from the Γ valley into the L and X valleys [80,81]. Consider again the band diagram of Fig 3.5.1. Electrons are injected into the Γ valley in the base region with a well-defined momentum k_i. If k_i is above the threshold for L valley transfer then injected electrons will scatter into

the L valley; similarly if k_i is above the threshold for X valley transfer electrons will scatter into the L valley and the X valley. When electrons scatter into the upper valleys not only do they lose energy due to their increased effective mass but their momentum will be randomized as well. Recall from the discussion above that if electrons do not have the proper momentum $k_\perp$ they will not get past the base-collector barrier and hence will not contribute to the collector current. Therefore if the collector current efficiency $\alpha = I_c/I_e$ is measured as a function of the injected electron energy (determined by V_{eb}) then the thresholds for L and X valley transfer may be obtained.

Experimental results obtained at T=4.2K for the transfer ratio α versus V_{eb} are shown in Fig. 3.5.4 [81] Two features are apparent. First α shows a clear peak at V_{eb}=350mV and a shoulder at V_{eb}=500mV. The first peak is attributed to the threshold for L valley transfer, in relatively good agreement with the reported value of

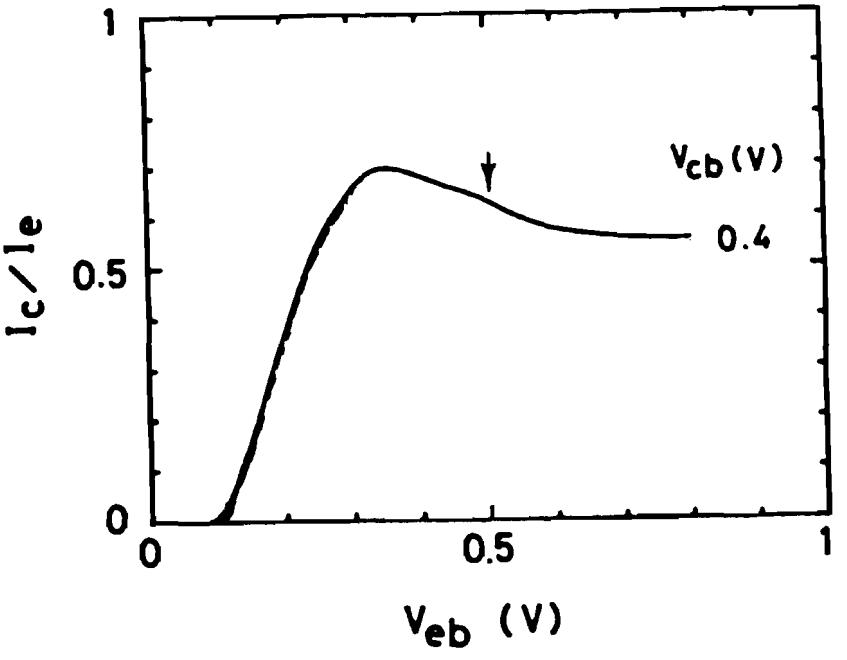

Fig. 3.5.4 Transfer ratio for an HET. The arrow indicates the change in slope which reflects the threshold for Γ-X transfer [81].

296meV [82]. The second feature, which is a change in the rate of decrease in α rather than a true peak, indicates the threshold for electron transfer into the X valley, also in good agreement with the reported value of 462meV [82].

Spectroscopy of the hot electron transistor is a very useful tool for understanding scattering mechanisms operant in short-channel devices. However, specific information about electron velocities in the channel is not obtained. In addition,the usual argument about the validity of transposing DC measurements into the transient regime, discussed in the previous section, also applies here. To date, the response of the hot electron transistor has not been measured in either the frequency or time domain. In particular, it should be possible to time resolve the onset of intervalley scattering by measuring the collector current and pulsing the emitter bias in much the same way that the permeable base transistor has been characterized on a picosecond time scale [83].

3.6 Transient Photoconductivity

The concept of the use of transient photoconductivity to study hot electron transport will be introduced here; it will be discussed in detail in Chapter 4. The concept is a hybrid optoelectronic approach, bringing together the advantages of using ultrashort dye laser pulses with the necessity of having contacts on the semiconductor sample to establish a well-defined field and measure current flow through the sample. The basic device under test is a simple photoconductive switch, which consists of a sample of bulk GaAs with two ohmic contacts, which is incorporated into a high-speed transmission line. According to the analysis by Auston [84], when a DC bias is applied and the switch is "closed" using a short pulse of light (which generates photocurrent), a transient voltage is launched in both directions on the transmission

line away from the switch. The transient voltage is equal to the convolution of the transient photoconductivity of the switch with the gap capacitance C_g. The transient photoconductivity is equal to

$$\sigma_{photo}(t) = \frac{n_e(t)ev_e(t) + n_h(t\_ev_h(t)}{E} \qquad [3.6.1]$$

where n_e and n_h are the photoexcited electron and hole densities and v_e and v_h are the respective drift velocities. Therefore, in a situation in which n_e, n_h, and v_h are approximately constant and the circuit response Z_0C_g is small relative to the time scale of interest, the transient voltage follows the transient electron velocity. With proper design these conditions may be satisfied in a simple photoconductive switch.

Once the voltage waveform has been generated it must be measured. There are two techniques currently available for characterizing subpicosecond electrical transients: electro-optic sampling [85] and Auston sampling [84]. The first will be described in Chapter 4 as the approach followed in this work. The second has been used by Hammond [86] to measure the transient voltage waveform as a function of DC bias voltage generated by a GaAs photoconductive switch.

The test structure used by Hammond is shown in Fig 3.6.1. This is the electrode pattern fabricated on the top surface of a GaAs wafer; the back surface was uniformly metallized and the top and bottom metallizations comprise three microstrip transmission lines. The gap formed by the upper transmission line and the central symmetric transmission line is the photoconductive switch which launches a waveform in both directions onto the central microstrip away from the switch. The transient voltage serves as a transient bias across the lower "sampler" gap. If the sampler gap is photoexcited with a laser pulse synchronous with the pump laser pulse, and if the sampler gap has been ion bombarded so that its impulse response is

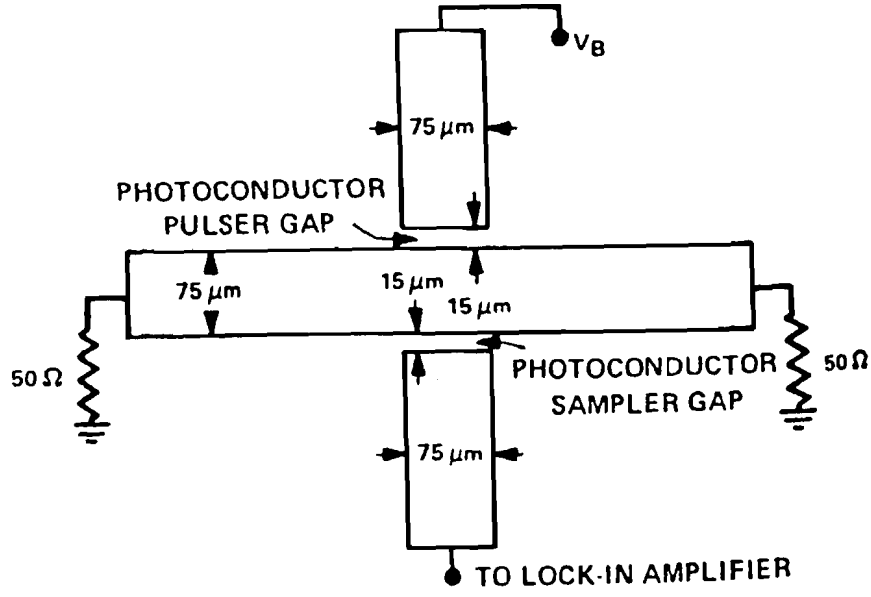

Fig. 3.6.1 Microstrip photoconductive pulser/sampler geometry used to generate and measure transient current waveforms [86].

very fast, then a measurement of the current flowing through the sampler gap as a function of pump/probe delay will yield a measure of the voltage (or current) waveform generated by the first switch.

Experimental results of Hammond are shown in Fig. 3.6.2. Temporal resolution was limited in that experiment by the device structure to 6ps. At low electric field the current rises smoothly to a constant value. At the intermediate field of 6.7kV/cm there is a 20% overshoot in the photocurrent. For the high field case the photocurrent recovers its low field behavior with no overshoot. Hammond argues that these results are consistent with the Monte Carlo electron drift velocity calculations of Ruch [5] (see Fig. 1.2). At low field Ruch predicts a steady rise of the drift velocity with no overshoot, in agreement with the low field experimental result. At moderate field Ruch predicts a 50% overshoot in the drift velocity with a duration of 4ps. This

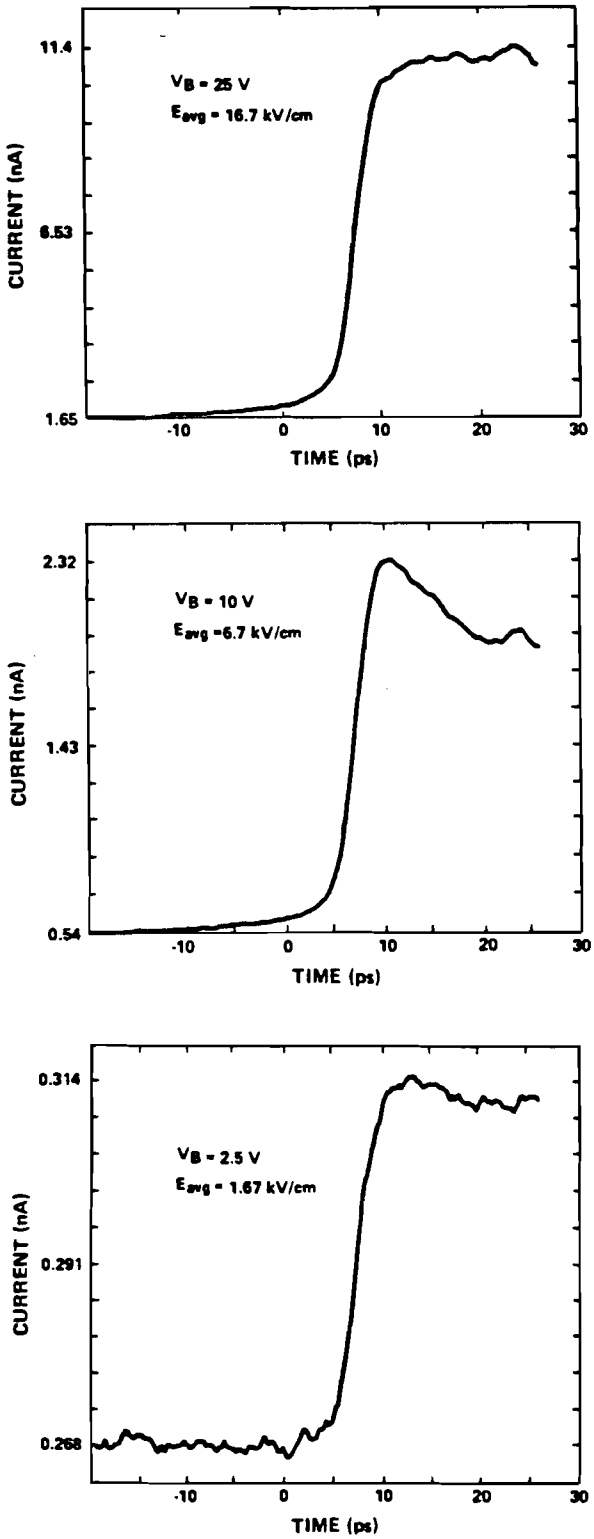

Fig..3.6.2 Transient current waveforms, obtained by Auston sampling, for three different applied fields [86].

agrees qualitatively with the experimental result when the limited temporal resolution is taken into account, which will effectively broaden and flatten the overshoot. The high-field prediction is a 350% overshoot with a duration of 3ps. According to Hammond this is too fast an event to be even partially resolved with a 6ps temporal resolution, which is why no photocurrent overshoot is observed at high field.

Quantitative interpretation of the data is prevented by several difficulties. First of all, it is not strictly valid to use Ruch's calculations for these experimental conditions because Ruch assumed that the electrons are initially at the band edge. As will be discussed in the next chapter, if the electrons start out with a large excess energy, as is the case when the excitation wavelength is 620nm, then the dynamics are quite different and the net amount of velocity overshoot is significantly reduced. Secondly, Hammond's use of annealed metallic contacts on semi-insulating GaAs do not insure good ohmic contacts to the semiconductor (see Appendix A1). As Hammond points out, fabrication of good n^+ contacts would give more confidence that the electric field in the sample was uniform. In addition, semi-insulating GaAs is usually heavily compensated, and it has been shown that compensation tends to reduce the degree of velocity overshoot [87]. Finally, the temporal resolution is not satisfactory. A much improved temporal resolution of a few hundred femtoseconds may be achieved by reducing the photoconductor dimensions and using electro-optic sampling, as will be detailed in the next chapter.

4.1 Theory of Transient Photoconductivity

The theory of the transient response of a photoconductive switch, developed by Auston [84] and mentioned briefly in the previous chapter, will be discussed in detail here. It will be shown that it may be extended into the regime of non-stationary transport through the use of Monte Carlo theory.

The approach of Auston is to model the photoconductive switch as a photoconductive element in parallel with a capacitance. There are two contributions to current flow in the circuit, particle and displacement current. Photoexcited particle current flowing through the device will change the voltage on the contacts, and this varying voltage will cause a displacement current to flow through the capacitance. If the photoconductor is imbedded in a transmission line then standard circuit analysis yields relationships between the charge, the incident, reflected, and transmitted voltage waveforms $V_i(t)$, $V_r(t)$, and $V_t(t)$, and the gap conductance G(t):

$$\frac{dq}{dt} + \frac{1}{2 Z_0 C_g}[1 + 2 Z_0 G(t)]\, q(t) = \frac{V_i(t)}{Z_0} \qquad [4.1.1]$$

$$V_r(t) = \frac{q(t)}{2 C_g} \qquad [4.1.2]$$

$$V_t(t) = V_i(t) - \frac{q(t)}{2 C_g} \qquad [4.1.3]$$

where Z_0 is the transmission line impedance and C_g is the gap capacitance. The integral of eq. [4.1.1] yields

$$q(t) = \frac{1}{Z_0}\int_{-\infty}^{t} dt'\, V_i(t) \exp\left\{ \int_{t}^{t'} \left[\frac{1 + 2 Z_0 G(t'')}{2 Z_0 C_g} \right] dt'' \right\} \qquad [4.1.4]$$

which in principle gives the explicit transient solution when substituted into eq. [4.1.3]; in practice the integral is difficult to evaluate for realistic conditions.

One simplifying assumption that is valid for the cases under study here is the

small-signal approximation, which assumes that the transmitted voltage $V_t(t)$ is much smaller than the incident voltage $V_i(t)$ (this is true when the photoexcitation intensity is relatively low). In this case the exponential in eq. [4.1.4] may be expanded; the first two terms are:

$$q(t) = \frac{1}{Z_0}\int_{-\infty}^{t} dt'\, e^{-\gamma(t-t')}\, V_i(t')$$

$$- \frac{1}{Z_0 C}\int_{-\infty}^{t} dt'\, g(t') \int_{-\infty}^{t'} dt''\, V_i(t'')\, e^{-\gamma(t-t')} \qquad [4.1.5]$$

$$\gamma \equiv \frac{1}{2 Z_0 C} = \frac{G_0}{C_g} \qquad G(t) = G_0 + g(t) \qquad [4.1.6]$$

Here the conductance G has been separated into a DC component G_0 (dark current) plus a time-dependent term g(t) (photocurrent). The first term in eq. [4.1.5] is the charging of the capacitance by $V_i(t)$ and the second term is the discharging through the conductance g(t). Substituting eq. [4.1.5] into eq. [4.1.3] and assuming that the incident voltage is a DC bias yields an extremely useful expression for the transmitted transient voltage:

$$V_t(t) = \left(\frac{Z_0 G_0 V_b}{1 + 2Z_0 G_0}\right)\left\{1 + \frac{1}{2Z_0 G_0 C_g}\int_{-\infty}^{t} dt'\, g(t')\, e^{-\gamma(t-t')}\right\} \qquad [4.1.7]$$

The first term is simply the dark current contribution, while the second term consists of a convolution of the time-dependent gap conductance with the gap capacitance. This is one of Auston's most important conclusions, that the gap capacitance plays a significant role in the transient switch response and may limit that response if the device is not properly designed.

So far the analysis has been quite general without reference to a specific

semiconductor. In order to extend it to a real situation it is necessary to derive an expression for the conductance g(t). In the previous section it was shown that in general the photocurrent is the product of the photogenerated carrier density, the carrier drift velocity, and the carrier charge. In Auston's analysis, in which it is assumed that the carrier velocities have reached equilibrium, the expression for the conductance is

$$g(t) = \frac{1}{V_b^2}\int d^3\vec{x}\,(n e \mu_n + p e \mu_p)\,|\vec{E}|^2 \qquad [4.1.8]$$

where n and p are the electron and hole densities, μ_n and μ_p are the respective mobilities, V_B is the bias voltage, and E is the applied electric field. If the laser photoexcitation is so short as to be considered a delta function then the density may be calculated using

$$n = p = \frac{(1-R)\,\alpha\,\varepsilon\, e^{-\alpha z}}{\hbar\omega} \qquad [4.1.9]$$

where R is the reflectivity, α is the absorption coefficient, ε is the incident optical pulse energy, and $\hbar\omega$ is the photon energy.

Eq. [4.1.8] is only valid for the case of constant carrier densities and constant and well-defined (field-independent) mobilities, but may be readily extended to other cases. If one is interested in relatively long-time behavior, the decay of n and p due to recombination (and perhaps other processes) may be included by inserting n = n(t) and p = p(t). For the important case of field-dependent mobilities, the field dependence $\mu_n = \mu_n(E)$ and $\mu_p = \mu_p(E)$ may be included. Finally, to apply the expression to very short times when the transient carrier velocities are strongly time and field dependent, eq. [4.1.8] must be written explicitly in terms of the velocities:

$$g(t) = \frac{1}{V_b^2}\int d^3\vec{x}\left\{ n e v_n(\vec{E},t) + p e v_p(\vec{E},t) \right\} E \quad [4.1.10]$$

$$= \frac{A}{V_b}\left\{ n e v_n(\vec{E},t) + p e v_p(\vec{E},t) \right\} \text{ for spatially independent variables}$$

A is the cross-sectional area. Equations [4.1.10] and [4.1.7] show that at short times, when the carrier density is approximately constant, the transient voltage waveform is a convolution of the gap capacitance with the transient carrier velocities. Put another way, if the gap capacitance is small, then any strong time-dependent behavior of the carrier drift velocity will be reflected in qualitatively similar behavior in the transient voltage response. Hence measurement of the voltage waveform may be a sensitive probe of ultrafast carrier dynamics, and in particular if the hole velocities are relatively time independent (as will be shown in a later section), then the measurement will yield direct information about quasi-ballistic electron transport and velocity overshoot. This work will be limited to a qualitative study of these effects in GaAs through comparison of photoconductively-generated voltage waveforms with calculations of the transient electron velocity under similar conditions; a quantitative comparison would require evaluation of the full spatial integral in eq. [4.1.10] and is beyond the scope of this work. This approach, the substitution of velocity transients calculated via Monte Carlo calculations into the Auston analysis to arrive at a realistic particle current and corresponding voltage transient, has been discussed by Grondin and Kann [88] and Caruso [89].

4.2 Description of the Electro-Optic Sampling Technique

The electro-optic sampling (EOS) technique has been chosen as the tool for measuring photoconductively generated transient voltages for a number of reasons. The primary reason is that of temporal resolution; this technique is capable of 100fs resolution if lithium tantalate is used, and could achieve even higher speeds if other electro-optic materials were utilized. Another reason is the flexibility and non-invasiveness of the technique. A number of embodiments have been developed, including ones that require little or no special modification of the device under test and which can be set up relatively easily. The technique is insensitive to wavelength over a wide band giving the experimentalist complete freedom to choose the most appropriate laser for the research at hand. The development of the technique and its different embodiments will be discussed below.

The EOS concept is based on the linear electro-optic effect. When an electric field E is applied to a transparent medium, a distortion of the electron charge clouds occurs if the medium is crystalline. This leads to a macroscopic polarization P in the medium that is in general a nonlinear function of the field. The polarization is usually written as a series expansion in the field:

$$P = \chi_1 \varepsilon_0 E + \chi_2 E^2 + \chi_3 E^3 + ... \qquad [\,4.2.1\,]$$

X_1 is the linear susceptibility which is responsible for the linear index of refraction. If the material lacks a center of inversion symmetry then the field produces an index change or birefringence which is linear in the applied field Specifically, the phase retardance δ introduced into a plane wave propagating through the medium by a voltage ΔV is given by

$$\delta = \pi \frac{\Delta V}{V_\pi} \qquad [\,4.2.2\,]$$

where V_π is the "half-wave voltage" of the material determined by its crystalline structure. If an analyzer, placed after the electro-optic medium, is used to measure the degree of polarization in a particular direction, then the intensity of the transmitted light will be

$$I = I_0 \sin^2 (\frac{\delta}{2}) \qquad [\ 4.2.3\ ]$$

This relationship is shown in Fig. 4.2.1. If the medium is optically or electrically biased at the half-wave point, then a small change in electric field will result in a linear change in transmission. Hence, after a DC calibration, measuring the intensity modulation of the probe beam will yield a direct measurement of the unknown electric field.

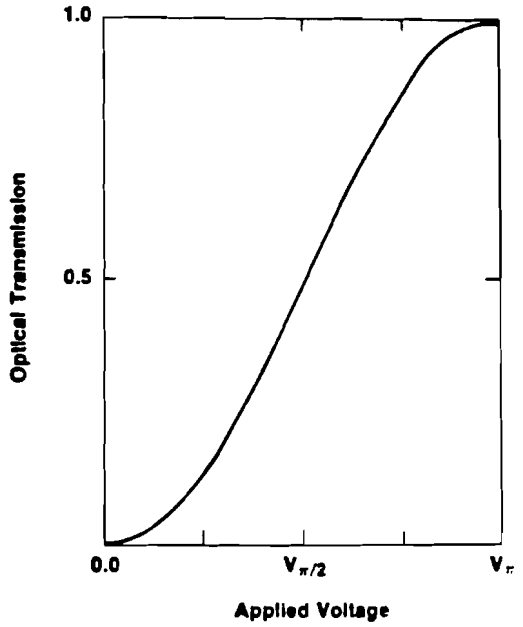

Fig. 4.2.1 Transmission curve for an electro-optic modulator.

The original EOS test geometry, developed by Valdmanis et. al. [85], is shown in Fig. 4.2.2. In this case the GaAs photoconductive switch is the device under test. In some manner the unknown transient electric field must be coupled into the electro-optic medium. In this first experiment this was accomplished by fabricating a transmission line on lithium tantalate and electrically connecting the photoconductive switch to the transmission line. One laser pulse was used to "close" the photoconductive switch, launching a transient voltage onto the transmission line which then propagates away from the switch. A second synchronized laser pulse is focused into the transmission line and samples a narrow slice of the transient waveform. The pump and probe pulses are actually pulse trains that are synchronized, so that by changing the pump/probe delay and measuring the modulation of the probe beam as a function of delay the unknown transient voltage as a function of time is obtained. A typical waveform sampled using the microstrip geometry of Fig. 4.2.2 is shown in Fig. 4.2.3 [85].

Valdmanis pioneered the sampling technique and demonstrated useful applications in discrete device testing, characterization of pulse propagation on transmission lines, and measurement of high-speed connector bandwidths [90]. He

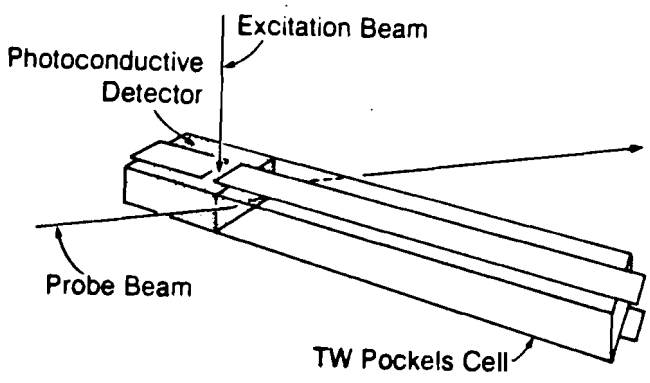

Fig. 4.2.2 Microstrip electro-optic sampling geometry [85].

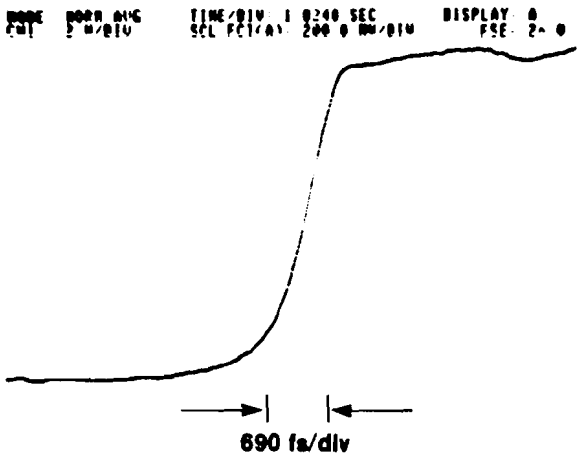

Fig. 4.2.3 Typical transient voltage waveform obtained with the microstrip sampling geometry [85].

also showed that under most experimental conditions the temporal resolution is determined by the particular sampling geometry and not by the intrinsic response of the electro-optic medium. Specifically, the temporal resolution τ_{exp} is the sum-of-squares convolution of four factors:

$$\tau_{exp} = [\, 2\,\tau_l^2 + \tau_0^2 + \tau_e^2 + \tau_i^2 \,]^{\frac{1}{2}} \qquad [\, 4.2.4 \,]$$

where τ_l is the pump/probe laser pulsewidth, τ_0 is the transit time of the optical probe pulse across the electric field lines, τ_e is the electrical transit time across the probe beamwaist, and τ_i is the intrinsic electro-optic response. τ_0 is determined by the transverse width and the separation of the transmission line electrodes, and τ_e is determined by the optical beam spot size. Valdmanis showed that by reducing the thickness of the sampling microstrip from 500um to 100um and reducing the probe beam waist from 110um to 15um the temporal resolution could be dramatically

improved from 2.4ps to 0.85ps.

τ_o is the dominating factor in the microstrip geometry. Because it is not feasible to fabricate microstrips thinner than 100um it is necessary to use a different geometry to further improve the temporal resolution. Mourou and Meyer [91] repeated the experiment using a coplanar strip transmission line, shown in Fig. 4.2.4. In this case τ_o is governed by the penetration depth of the field into the substrate which scales with the separation between the lines. Using a 50um strip width and spacing they observed a 0.46ps risetime. Further improvements in the temporal resolution may be realized by reducing the probe beam spot size to 5um, reducing the stripline dimensions to 10um, and reducing the laser pulsewidth to 50fs. Using these parameters and assuming that the intrinsic response of lithium tantalate is 50fs [51], eq. [4.2.4] yields a practical resolution limit of 151fs. All of these refinements are necessary in order to resolve velocity overshoot phenomena on a time scale of a few

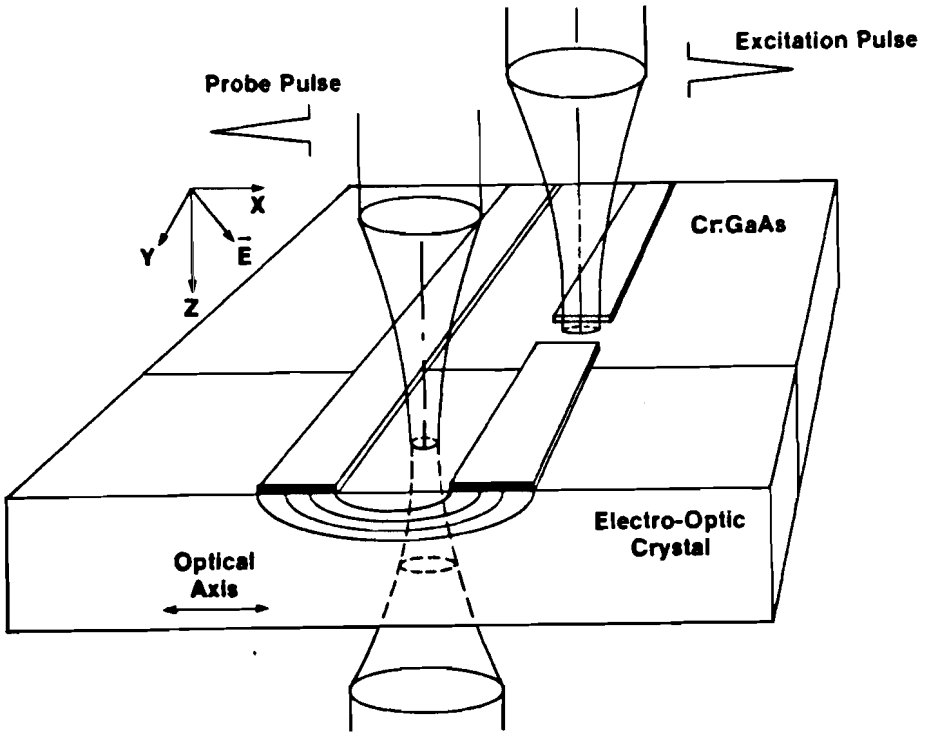

Fig. 4.2.4 Coplanar stripline sampling geometry [91].

hundred femtoseconds.

The EOS technique only requires that some field lines from the device under test extend into the electro-optic medium. It is not strictly necessary to fabricate a separate electro-optic transmission line and then have to worry about efficiently coupling the electrical signal into it (a non-trivial problem). Fig. 4.2.5 demonstrates several EOS embodiments that have been developed. "In-situ" EOS, (c) in the figure, may be used if the substrate of the device under test is itself electro-optic. GaAs, InP, and CdS are examples of technologically important semiconductor materials that are also electro-optic (Si is a notable exception because of its inversion symmetry). Weingarten et. al. [92] and Jain et. al. [93] have shown that this approach may be used to test internal nodes on GaAs IC's. The drawback to this approach is that the probe wavelength must be sub-bandgap, which for GaAs requires near-IR light. Though picosecond and subpicosecond near-IR lasers have been developed, a stable source of sub-100fs near-IR laser pulses free of temporal wings has yet to be demonstrated.

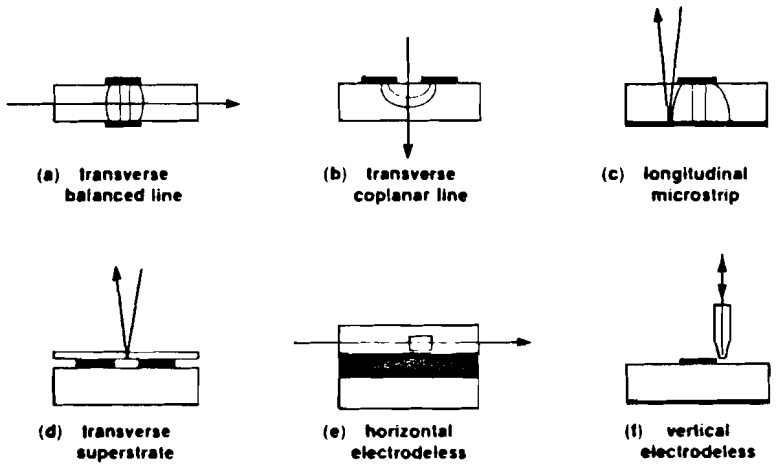

Fig. 4.2.5 Embodiments of the electro-optic sampling technique.

The electro-optic superstrate geometry, Fig. 4.2.5(d), was first described by Meyer and Mourou [94] as a way of performing two-dimensional mapping of transient electrical fields on the surface of a circuit or sample. A high-reflectivity dielectric coating is required in this case on the surface of the EO medium in proximity to the sample. Fringing fields from the sample substrate extend into the superstrate. The probe beam is focused into the area of interest, passes through the fringing field, is reflected off of the HR coating, passes again through the field and exits the sampling crystal. Two-dimensional mapping is achieved simply by scanning the location of the probe beam to different x and y positions of interest. This is the primary geometry used in this work and will be further detailed in the following section. One disadvantage to this geometry is due to the high dielectric constant of lithium tantalate (40), which may tend to load certain circuits under test. To minimize this loading, the size of the superstrate may be reduced, resulting in the so-called "finger-probe" geometries shown is Fig. 4.2.5 (d) and (e). Valdmanis [95] and Nees and Mourou [96] have used these geometries to measure transient waveforms on GaAs and Si integrated circuits.

4.3 Predictions of the Monte Carlo Theory

The Monte Carlo model used here is a standard one that has been applied to the study of transport in GaAs. The band structure includes three nonparabolic valleys (Γ, L, X) in the conduction band and a single parabolic heavy hole band. The light hole band and split-off hole band have been neglected due to the low density of states in those bands. Scattering from elastic acoustic phonons, inelastic optical phonons, and ionized impurities have been included. All simulations for conditions of the

transient photoconductivity experiment have been run with T=300K and have assumed a density of $n=p=1x10^{17}cm^{-3}$. Osman and Ferry [18] have shown that at this moderate density electron-hole scattering may be neglected. Photogeneration of the electron/hole gas is assumed to be a delta function in time and in energy (determined by the wavelength of photoexcitation). One subtlety of the photogeneration process is that, unlike carrier injection from contacts, this generation process results in an initial state of the carriers which has no predetermined net momentum. The calculation therefore initializes the carriers with a fixed energy but with a k-vector chosen at random.

The simulation models transport in the bulk without detailed consideration of what happens when carriers reach the contacts. This is justified if the transit time of carriers across the device is much longer than the time scale of interest (the "long device" limit). For the case of interest here electrons moving at $v_e=1x10^7cm/sec$ cross a 10μm gap in 100ps. Only the first 3ps of transport is considered here so the assumption is well justified.

The contribution to the photocurrent due to the holes is considerably less than that for the electrons. The hole effective mass is much larger than the electron mass, hence the hole velocities are much smaller. A steady-state calculation of hole velocities by Brennan and Hess [97] indicates that the equilibrium hole velocity at E=10kV/cm is only $v_h=2x10^6cm/sec$, a factor of 5-10 times smaller than the electron velocity. The transient hole velocity is also expected to experience overshoot [18,24] but the degree of overshoot would have to be 5:1 or greater to compete with the electron overshoot. There is no reason to expect the hole overshoot to be this large. In addition, the hole overshoot takes place on a faster time scale because the density of states is higher and hence scattering rates are larger than for the electrons. Hence any hole transients are expected to have subsided within the first 100fs. For these reasons hole velocities

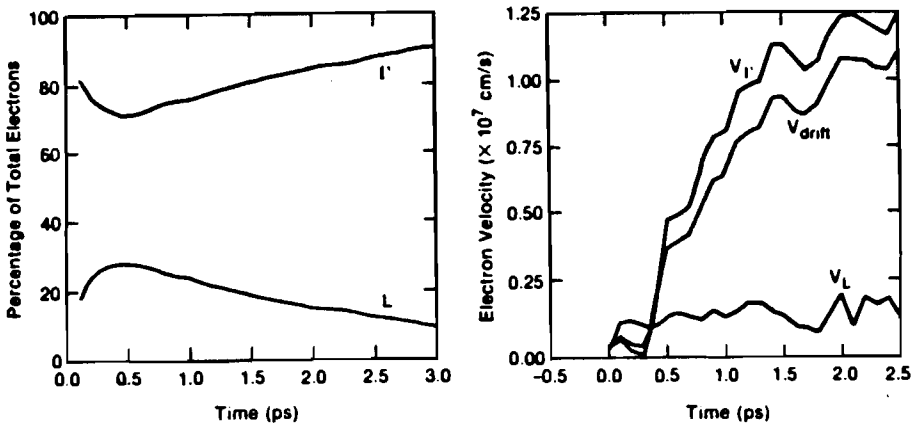

Fig. 4.3.1 Transient Γ and L valley populations and velocity calculations for λ_{ex}=620nm and E=2kV/cm.

have been neglected in the following calculations.

A calculation of the electron drift velocity and the relative populations in the Γ and L valleys for λ_{ex}=620nm and E=2kV/cm is shown in Fig. 4.3.1. At this photoexcitation wavelength the electrons have an excess energy of 519meV, well above the threshold for Γ-L scattering (290meV). Intervalley scattering is very efficient so that in the first 100fs 20% of the electrons have already scattered into the L valley. The electrons in the Γ valley relax down toward the band edge, but as long as their energy is above 290meV they continue to scatter into the L valley. After 500fs the energies of the Γ-valley electrons have fallen below the intervalley scattering threshold, and the population in the Γ valley begins to rise again as electrons that initially scattered to the L valley begin to scatter back into the Γ valley. At equilibrium about 90% of the electrons reside in the Γ valley.

This behavior is reflected in the net drift velocity of the electrons, also shown in Fig. 4.3.1. The drift velocity follows the velocity of the Γ-valley electrons with

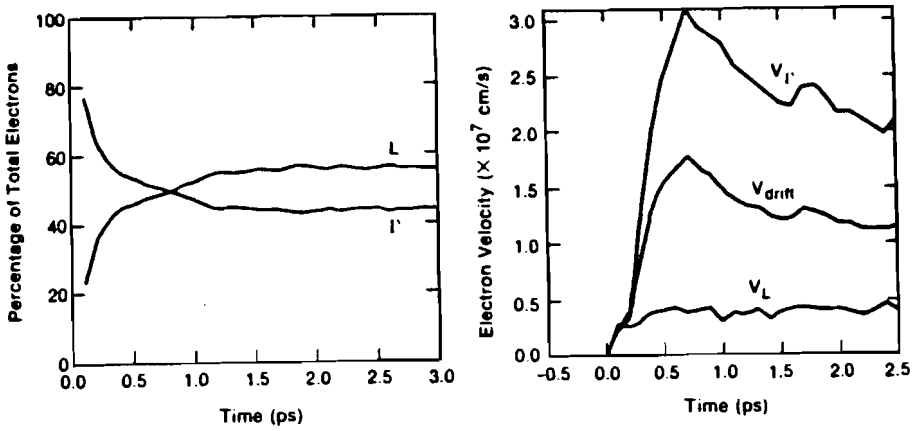

Fig. 4.3.2 Transient Γ and L valley populations and velocity calculations for λ_{ex}=620nm and E=10kV/cm.

only a small contribution from the L-valley electrons (at no time are there more than 25% of the electrons in the L valley). Hence for this photoexcitation wavelength and applied field the electron drift velocity is expected to rise gradually to a constant value in approximately 2ps with no velocity overshoot.

The situation is quite different for the high-field case. shown in Fig. 4.3.2. In this case the relaxation of the photoexcited electrons toward the band edge competes with the electron heating from the applied field. More electrons remain above the intervalley transfer threshold and hence more get scattered into the L valley. After 1ps more than 50% of the electrons have scattered into the L valley, and at equilibrium 55% of the electrons are in the L valley and 45% reside in the Γ valley. Therefore the equilibrium drift velocity is the average of the velocities in the two valleys and is significantly reduced. This large percentage of electron transfer to the sideband and the subsequent slowing of electrons in the L valley due to lower mobilities is the source of velocity overshoot in GaAs. The degree of overshoot in this case is only 1.5:1 because electrons were initially above the intervalley transfer threshold and

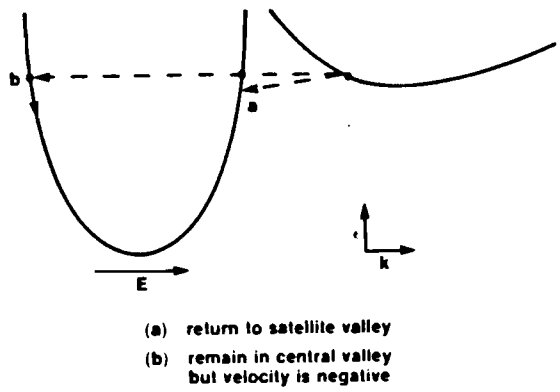

Fig. 4.3.3 Schematic diagram of the Jones-Rees effect [98].

began scattering out of the Γ valley immediately. It will be shown that the closer electrons are photoexcited to the band edge, the more dramatic will be the degree of velocity overshoot.

Consider again the low-field calculations of Fig. 4.3.1. One anomalous detail of the transient drift velocity is the delay in onset during the first 300fs. At first this feature was thought to be insignificant and due to numerical noise, but it was found repeatedly for several different low-field calculations. In fact it is a signature of the Jones-Rees effect [98] and its potential role in transient photoconductivity measurements has been discussed by Grondin and Kann [88]. The phenomenon is shown schematically in Fig. 4.3.3. At t=0 states (a) and (b) are equally populated by the laser excitation. Electrons initially at point (b) will cool down toward the band edge and will have a negative velocity. Electrons generated at point (a) will be accelerated by the field and will scatter into the L valley and slow down. Therefore at low fields and short times the electrons will either have a negative or a small positive velocity and the net drift velocity will be close to zero.

For high fields, as already discussed above, many more electrons scatter into the L valley and the initial even distribution between states (a) and (b) is randomized very quickly. This is shown more clearly in Fig. 4.3.4 in which the total number of electrons with negative velocity is plotted for the first picosecond of transport. The contribution from negative-velocity electrons is lower at high field and therefore the drift velocity rises without any delay. Hence the prediction of the Monte Carlo theory is that there will be a delay in the onset of the photoconductivity for low field relative to the onset at high field.

Most of the calculations of velocity overshoot published to date have assumed that the electrons were initially at the band edge, and the degree of overshoot predicted was on the order of 3:1. This initial condition is the optimal condition for velocity overshoot because the electrons have the maximum amount of time to accelerate in the applied electric field before they gain enough energy to scatter to the sideband. For reasons to be discussed in the next section the experiment could not be performed

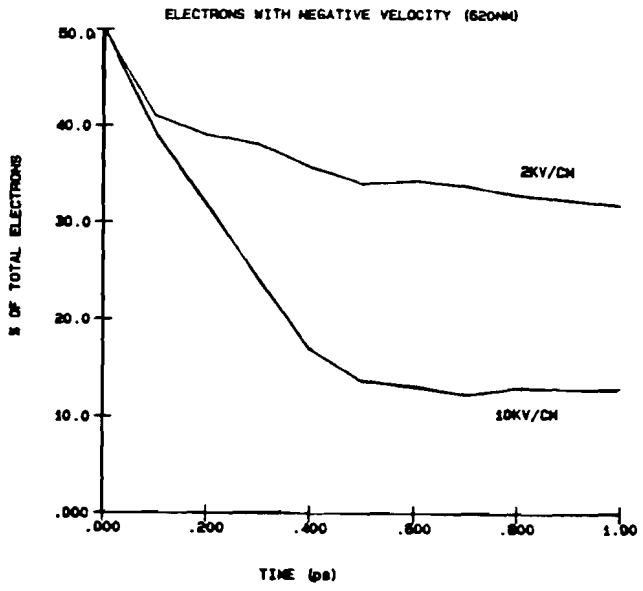

Fig. 4.3.4 Calculation of the total number of electrons with negative velocity for conditions of low and high fields.

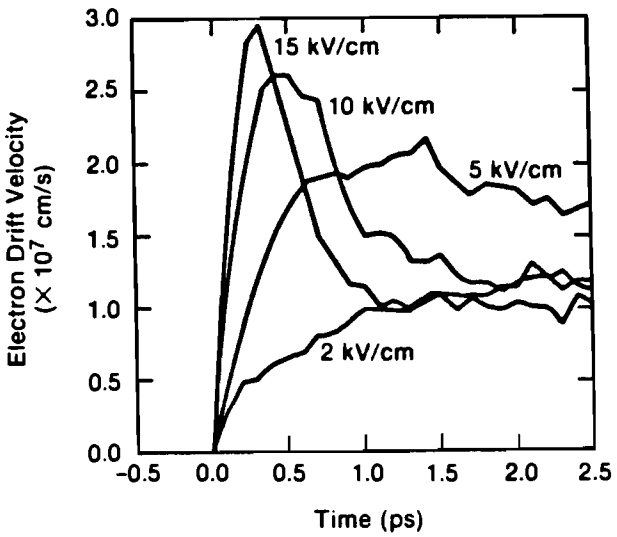

Fig. 4.3.5 Predicted transient electron drift velocity for λ_{ex}=760nm and several different applied fields.

with band edge photoexcitation (871nm) but could be performed at an intermediate wavelength of λ_{ex}=760nm. In this case the electrons have an excess energy of 188meV, well below the threshold for intervalley transfer. Monte Carlo drift velocity calculations for λ_{ex}=760nm and several different applied fields are shown in Fig. 4.3.5. Note that, as expected, for E=10kV/cm the degree of overshoot is enhanced to 2.5:1 and for the extreme field of 15kV/cm the overshoot is 3:1.

This section has outlined the Monte Carlo simulations of the transient electron drift velocity that have been carried out for the experimental conditions of interest in this work. The following section will describe the transient photoconductivity experiments that have been performed and will compare these predictions with the experimental results.

4.4 Experimental Observation of Velocity Overshoot and the Jones-Rees Effect

This section will detail the photoconductivity experiments that have been performed which constitute a time-resolved measurement of velocity overshoot and the Jones-Rees effect. Included in this discussion will be the development of different sampling geometries and fabrication techniques and the study of various forms of GaAs and contact metallizations to optimize the magnitude and reproducibility of the overshoot effect.

4.4.1 Sample Fabrication

This section will describe the procedures that were used to fabricate photoconductive switches imbedded in transmission line structures that yielded the experimental data that is outlined in sections 4.4.3 and 4.4.4.

The first geometry that was studied was the coplanar stripline structure (Fig. 4.2.4). The fabrication of the structure went as follows. A batch of GaAs and $LiTaO_3$ pieces were cut and polished to form plates of approximately the same dimensions (typically 10x10x0.5 mm). All cutting, grinding, and polishing of samples was carried out at the Optical Fabrication Facility at the University of Rochester. One edge of each piece was ground and polished very carefully to achieve maximum flatness and smoothness. These respective flat edges of the two materials were then butted together, and the two pieces were mounted on a flat glass plate using ultra-violet-cured cement; the two pieces were pressed together during the cure to insure a very close fit. Next the two materials were ground and polished simultaneously to an optical finish to insure a smooth contour from one material to the other. The pieces were examined under a high-power microscope to determine the closeness of the fit between the GaAs and $LiTaO_3$. The pieces with the best fit and the lowest number of chips at the interface were then selected for further processing.

Several different photolithographic procedures were investigated for the fabrication of the coplanar striplines and photoconductive switches. All the photolithography fabrication was performed using the facilities of the Microelectronic Engineering Department at Rochester Institute of Technology. Initially a "wet-processing" technique was used which involved evaporating the desired metal onto the GaAs/$LiTaO_3$. surface, patterning photoresist on top of the metal as an etch pattern, etching the metal, and finally removing the photoresist. Two problems were encountered with this approach. First, the gold etchant that was used appeared to slightly etch the GaAs surface, which was undesirable. Secondly, for unknown reasons the etchant preferentially attacked the metal at the GaAs/$LiTaO_3$ interface first, which usually meant that there would be no metal remaining at the interface by the time the rest of the pattern was well defined. This resulted in transmission lines which were consistently discontinuous across the interface. For these reasons this approach was abandoned. Continuity of the lines across the interface was determined using a wafer probe station, tungsten probes with 5μm tips mounted on micromanipulators, and an ohmmeter connected between the two probes.

To achieve continuous transmission lines across the GaAs/$LiTaO_3$ interface the "lift-off" photolithographic process [127, 128] was evaluated. The advantage of this approach is that no chemical etching is required. The procedure is shown in Fig. 4.4.1. The samples were cleaned, and the photoresist was spun on, baked, and exposed in the desired pattern. After development of the resist the resultant patterned resist had a characteristic reverse bevel profile (Fig. 4.4.1(c)). Then the desired metal was evaporated on. Because of the beveled cross-section, a clean break occurs between metal on top of the photoresist and the metal on the substrate (Fig. 4.4.1(d)) as long as the photoresist thickness is much larger than the metal thickness. The final step is to remove the photoresist with an appropriate solvent.

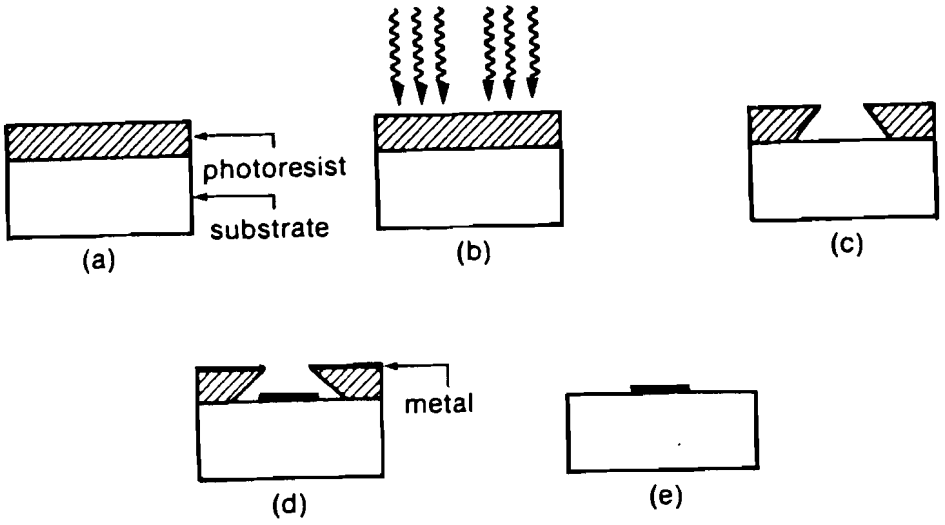

Fig. 4.4.1 Lift-off photolithographic process: (a) deposition of photoresist; (b) photoresist exposure; (c) developed photoresist with reverse bevel profile; (d) metallization; (e) final metal pattern after photoresist removal.

Details of the optimized lift-off process are as follows:

1) Clean Sample: 15 minutes ultrasonic acetone, 15 minutes ultrasonic methanol, blow dry.

2) Photoresist Adhesion Promoter: Shipley HMDS, spun on @ 3000rpm for 60 seconds.

3) Apply Photoresist: Shipley AZ5214, spun on @ 3000rpm for 30 seconds (thickness=1.5um).

4) Pre-bake: 90±5°C for 30 seconds on a temperature-controlled hotplate.

5) Expose: 45mJ UV exposure with photolithographic mask aligner.

6). Post-exposure Bake: 125±1°C for 30 seconds on a temperature-controlled hotplate.

7) Flood Exposure: 200mJ UV exposure with photolithographic mask aligner.

8) Develop Photoresist: Shipley AZ424K developer diluted 1:1 with water for 20 seconds, deionized water rinse for 5 minutes, blow dry.

9) Metallization

10) Liftoff: soak for one hour in Shipley AZ1500 thinner, with ultrasonic agitation for 5 seconds every 15 minutes.

This procedure resulted in very uniform structures with line dimensions down to 10μm. It was found that 50μm-wide lines could be reliably fabricated continuously across the GaAs/$LiTaO_3$ interface. Only approximately 15% of the 20μm lines were continuous across the interface, and only 1-2% of the 10μm lines were continuous.

Thermally evaporated metallizations were performed in a standard bell-jar evaporator pumped down by a diffusion pump and cold trap. The typical background pressure in the growth chamber was $5x10^{-7}$T. The substrates were unheated during growth. The Ni, AuGe, Au, and In deposition rates were determined by test runs on glass substrates. The thickness of the test films were measured with a DEKTAK profilometer. During evaporation metal thicknesses were controlled with a quartz-crystal thickness monitor.

A metallization that was used frequently (henceforth referred to as the "standard AuGeNi metallization") consisted of 200ÅNi/500ÅAuGe/2000ÅAu. After evaporation and subsequent removal of the excess photoresist and metal, the samples were annealed in a small furnace through which dry nitrogen gas flowed. The behavior of the contacts did not depend critically on the annealing process as long as the anneal cycle was longer than ten minutes and the anneal temperature (monitored with a thermocouple) was above 385°C. This corresponds to the NiAuGe eutectic temperature.

The above procedure describes the process that was used for the initial

experiments on Bridgeman-grown Cr-doped GaAs samples. One modification was introduced for the second set of measurements on undoped LEC GaAs. A major cause of poor ohmic contacts is the presence of an oxide layer between the metallization and the GaAs substrate, and GaAs normally has a native oxide unless it is purposefully removed. An "oxide strip" step was added just prior to evaporation of the metal. The solution for the oxide strip consisted of 2% ammonium hydroxide/ 0.7% hydrogen peroxide/ 97.3% H_2O. The amount of H_2O_2 was adjusted to achieve a pH of 8.5, which was measured with a calibrated pH meter. Steps in test GaAs samples were etched and the step height was measured with the profilometer. The etch rate was determined to be 25±1Å/second. The prepared samples were dipped in the etchant for 2-4 seconds, rinsed for one minute in deionized water, blown dry with dry nitrogen, and then were loaded immediately into the evaporation chamber.

The third and final set of photoconductivity measurements utilized a different sampling geometry and epitaxial GaAs. The reflection-mode sampling geometry is shown in Fig. 4.4.3. This geometry eases the fabrication constraints because the sampling crystal and photoconductive switch are produced separately. Consequently the difficulty of having to fabricate continuous lines across the GaAs/$LiTaO_3$ interface is eliminated.

The sampling crystals were constructed as follows. Thin (0.5mm) slices of $LiTaO_3$ were cut from a 2" diameter boule using a slow-speed diamond saw. Next these wafers were thinned by lapping to the desired thickness of 200um and both faces of the wafer were polished to an optical finish. The polished wafers were sent to the Virgo Corporation, a commercial coating house, where one surface of each wafer was coated with a broad-band multiple-stack high-reflectivity dielectric coating (R>99% @ 620±50nm or 760±50nm). The final step was to dice the wafers into 3mmx3mm pieces using a diamond wafer saw.

The epitaxial GaAs consisted of 500Å $10^{18}cm^{-3}$ n^+-GaAs/ 2 μm undoped ($5x10^{14}cm^{-3}$) GaAs grown on semi-insulating substrates. MBE GaAs wafers obtained from Cornell University and Epitronics Corporation were studied as well as MOCVD GaAs wafers from Spire Corporation. Metallizations were patterned on the wafers using the lift-off process described above into 50, 20, and 10μm coplanar striplines with a variety of gap lengths for the photoconductive switches. In addition, test pads were fabricated along one edge of each chip in the form of 100μmx100μm squares with separations of 10, 20, 50, and 100μm for the purpose of evaluation of the contacts. The final step was to remove the thin n^+-GaAs layer everywhere except under the metallization by using the calibrated GaAs etch. In most cases the standard NiAuGe evaporated metallization described above was used; in addition, 2 wafers of MBE GaAs were sent to MIT Lincoln Laboratories after the photoresist had been patterned for a sputtered NiAuGe metallization. Sputtered metallizations have been shown in some cases to form superior ohmic contacts relative to evaporated metallizations [129]. No significant difference was observed between the two types of metallization in the DC I-V behavior or the transient response. The final fabrication step involved dicing the wafers into 5mmx5mm chips using a diamond wafer saw.

For all three sets of measurements the samples were mounted similarly on machined brass blocks with high-speed OSSM connectors attached. The samples were mounted with silver paint or silver epoxy. Electrical connections were made using silver paint for the load and bias ends of the transmission lines first to intermediate bias pads (gold-plated alumina) and then to the connectors. In the case of the reflection-mode geometry a small (50μm diameter) hole was scratched in the HR coating prior to mounting the sample crystal to allow for passage through the crystal of the pump beam to the photoconductive switch (note: this detail is not shown in Fig. 4.4.3). The crystal was then mounted with the HR coating face-down on the GaAs

substrate. The crystal was positioned carefully under a microscope to align the hole in the coating over the desired switch, and then the corners of the crystal were tacked down with silver paint.

4.4.2 Experimental Procedures

This section will discuss the specific electro-optic sampling techniques, described in general in section 4.2, that were used to acquire the experimental results that will be presented in the following sections.

There were two sampling geometries that were utilized, shown in Fig. 4.4.2, which will be referred to as the transmission and reflection-mode geometries. The

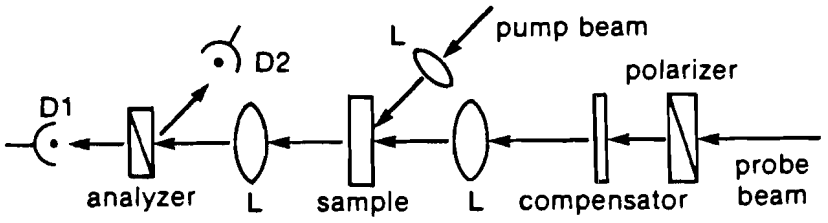

Transmission Mode

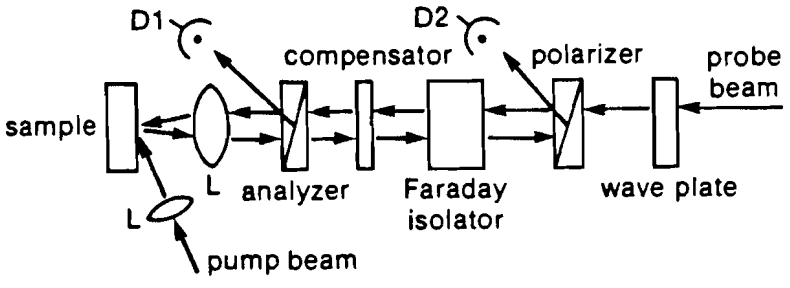

Reflection Mode

Fig. 4.4.2 Transmission-mode and reflection-mode sampling geometries; L=lense, D=detector.

sample geometries for these respective experiments are shown in Figs. 4.2.4 (transmission) and 4.4.4 (reflection).

For the transmission-mode geometry the experiment was set up as follows. The direction of the polarizer was set 45° relative to the optical axis of the $LiTaO_3$ sampling crystal. This is the alignment for maximum electro-optic efficiency. The analyzer was adjusted to extinguish the probe beam when the sample and compensator were not in the beam. The sample was then placed at the focus of the 20X objective L1. The sample was mounted on a precision three-axis manual translation stage in order to position the probe spot accurately. Not shown in the figure is a beamsplitter to the right of L1 and an off-axis telescope which allowed the sample to be viewed through the objective down the probe beam-line. Next the Soleil-Babinet compensator was introduced into the probe beam. This was used to compensate for the static birefringence of the $LiTaO_3$ crystal and to optically bias the crystal to its half-wave point. This guaranteed that the optical response was linear in the applied electric field. This condition corresponded to equal signal levels on detectors D1 and D2. The detectors were large-area EGG FND-100 p-i-n photodiodes biased at -90V. The focusing lense for the pump beam, with a typical focal length of 20mm, was mounted on a separate x-y-z translation stage to allow for precision positioning of the focussed pump beam on the photoconductive switch.

In the original configuration developed by Valdmanis [90] the output of the detectors D1 and D2 were fed into a PAR model 116 differential pre-amplifier and then into a PAR model 124A lock-in amplifier. Modulation was impressed on the signal of interest either with a mechanical chopper in the pump beam or via modulation of the DC bias on the photoconductive switch. The lock-in amplifier was synchronized to the modulation frequency of 1kHz. The output of the lock-in went into a EGG PAR model 4203 signal averager.

An optical delay line in the pump beam was mounted on a Klinger 8μm/step stepper which was run by a Klinger CC1.1 stepper controller. The controller sent a signal which drove the x-axis of the signal averager, while the lock-in output was displayed on the y-axis. The time-base of the signal averager was calibrated by measuring the clock rate of the signals being sent to the delay line and knowing that 8μm/step corresponds to 26.67fs/step double-pass using the speed of light. The delay line was scanned for the desired number of (equivalent) picoseconds, then it was returned to its original position and another scan was initiated. Depending upon the amplitude of the signal being measured, typically 1-100 scans at 10 seconds/scan would be accumulated corresponding to $1\text{-}100\text{x}10^7$ laser shots. Voltage calibration was achieved by applying a known voltage at the lock-in frequency directly to the sampling crystal and recording the corresponding offset signal on the lock-in. Using this arrangement Valdmanis was able to demonstrate a sensitivity of 1mV with an integration time of 1000 seconds. Sensitivity is specified in this case as the signal level when S/N=1.

The primary source of noise in this system is the amplitude noise of the dye laser, which is governed by the 1/f noise spectrum of the argon pump laser. The noise spectrum of the dye laser rolls off to a constant level above 3MHz. Therefore if the experiment could be performed at a lock-in frequency above 3MHz the sensitivity should be significantly improved. This was first attempted with a PAR high-frequency lock-in, but it was found that the front-end detection electronics in this instrument were inferior to the low-frequency instrument. As a result only a small improvement in signal/noise was observed [130, 131]

An improved scheme was developed by J. Chwalek at the Laboratory for Laser Energetics involving the use of RF mixers [130]. An HP3326A 2-channel frequency synthesizer was used as an ultra-stable frequency source. One frequency,

f_1=3.56MHz, was used to drive the modulation of the experimental signal, either using a Chronetics pulse generator to modulate the photoconductive switch bias or an Intra-Action AOM-80 acousto-optic modulator to modulate the intensity of the probe beam. The second frequency, f_2=3.5625MHz, was mixed with the detector signals D1 and D2 using separate matched RF mixers. The output of the two mixers was then fed into the differential amplifier input of the low-frequency lock-in amplifier, which was set to measure a modulated signal at the difference frequency f_1-f_2=2.5kHz. This allowed the experiment to be modulated at a high frequency but also allowed exploitation of the high-Q electronics of the low-frequency lock-in. This arrangement has demonstrated a sensitivity of 150μV with a single 10-second scan. With longer integration times this sensitivity could be reduced to less than 50μV. This is the detection scheme that was used to acquire the data that will be discussed in the following sections. One other improvement in the experiment involved the addition of an ATT PC computer by which the data could be stored on floppy disks for future reference. Eventually this computer will be programmed to emulate the signal averager and control the delay line for fully automated data acquisition.

All of the detectors and electronics were identical for the experiments that utilized the reflection-mode geometry (Fig. 4.4.2). The only difference, aside from the obvious one in configuration, was the addition of a Faraday isolator. Dye lasers are very sensitive to reflections external to the laser cavity and can become unstable if the cavity is not isolated from stray reflections from external optics. The reflection-mode experiment was performed at near-normal incidence to the sample, so that it was relatively easy for stray reflections and scattered light to propagate back into the laser cavity. This was prevented with a Faraday isolator. A rod of Faraday material was mounted in the center of a strong magnet. The strength of the field and the length of the rod were designed were designed to introduce a 45° Faraday rotation into the

polarized probe beam as it passed through on its way to the sample After reflection off of the sample the beam passed back through the isolator where it gained another 45° rotation. Its polarization was then orthogonal to the polarizer and the beam was rejected into detector D2. Use of the Faraday isolator eliminated any problems with laser instabilities due to reflections.

4.4.3 CPM (λ_{ex} = 620nm) Results

The initial set of measurements were carried out using the coplanar stripline geometry (Fig. 4.2.4). This geometry was chosen for its improved temporal resolution, as discussed in section 4.2.

One of the requirements of this geometry is that bulk (boule-grown) GaAs be used because there is considerable grinding and polishing of the material during fabrication (a thin epitaxial layer would not survive this treatment). Because it is also necessary to use semi-insulating material (so that the dark current is small relative to the photocurrent) the two options are to use either Cr-doped Bridgeman material or undoped LEC GaAs. The Bridgeman growth process is the older technique in which a quartz ampoule containing arsenic and gallium is passed horizontally through a zone furnace. Chromium impurities are introduced which act as deep electron traps to increase the resistivity. The first experiments utilized Cr-doped GaAs because it was relatively inexpensive and readily available. In this case no dependance of the transient photoconductivity on the applied electric field was observed and in particular no photocurrent overshoot was observed. This was presumably due to two reasons. The first is that Bridgeman material is of relatively poor quality and the Cr impurities and lattice dislocations act as scattering centers and traps that severely limit the

mobility of the electrons. The other is that all metallizations tested (including evaporated Au, AuGeNi, and In, both annealed and unannealed) resulted in non-reproducible non-ohmic contacts. This was reflected in highly non-linear DC I-V characteristics which varied strongly from one test pattern to the next on a chip and from chip to chip from the batch (the relationship between the I-V characteristic and the quality of the metal-semiconductor contact is discussed in Appendix A1).

The next step was to utilize undoped LEC GaAs and to incorporate a step prior to metallization to remove the GaAs surface oxide. LEC stands for the Liquid Encapsulated Czochralski growth technique. In this technique a seed crystal is pulled slowly from a GaAs melt. The melt is "encapsulated" with a layer of molten B_2O_3 to prevent arsenic loss. With this technique semi-insulating material can be obtained without the addition of impurities; instead, a deep donor level known as EL2 is introduced which depends on the melt stoichiometry. In this case the contacts were more reproducible and the best contacts were obtained using annealed evaporated In. Even in the best case, however, the DC I-V characteristics varied significantly from one photoconductive gap to the next on a chip and from one chip to the next. The variations ranged from quasi-linear I-V characteristics to curves that exhibited strong diode-like behavior. Best-case transient voltage waveforms for these samples are shown in Fig. 4.4.3. This was the first instance of an observed photocurrent overshoot that was present at high fields but not at low fields. The overshoot appeared on samples from the batch that exhibited quasi-linear I-V characteristics but did not appear on samples which demonstrated highly nonlinear DC I-V response. Two difficulties were apparent during the experiment. First, the shape of the voltage transient was strongly dependent upon the illumination of the gap, which is an indication of poor contacts [84]. Secondly, the risetimes of the transients were unexpectedly long, on the order of 1.5ps, which can only partially be explained by

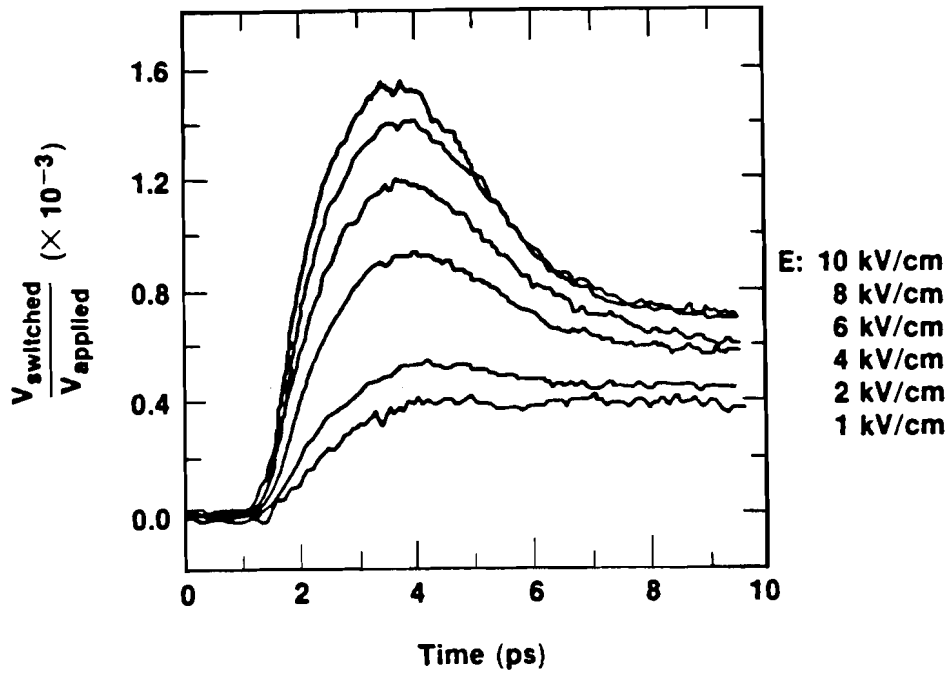

Fig. 4.4.3 Transient voltage waveforms obtained using the coplanar strip geometry with semi-insulating LEC GaAs and annealed In contacts.

the relatively large linewidths and line separation (50 μm) of the geometry used. Some of this slow response is also likely due to contact effects.

As shown in section 4.2, improvements in the temporal resolution would require using smaller stripline dimensions. However, it was found that the difficulty in fabricating continuous transmission lines across the GaAs/$LiTaO_3$ interface increased dramatically as the linewidth was reduced. Yields for 20μm linewidths were extremely low and for 10μm linewidths or smaller were essentially zero.

At this point it was decided to make two significant changes in the experiment. This first was to perform the experiment in the reflection-mode geometry, which was described in section 4.2 and is shown in more detail in Fig. 4.4.4. This geometry has

several advantages and one disadvantage. One advantage is that it separates the photoconductive switch fabrication from the sampling crystal fabrication, each of which can be done independently with standard procedures and very high yields. In particular, the coplanar strip linewidths on the GaAs may be made as small as practicable with the lithography at hand. Another advantage is that the probe beam may be moved arbitrarily close to the switch, thereby minimizing any distortion of the voltage waveform due to modal dispersion on the transmission line. The disadvantage is that the probe beam must pass through the fringing field twice which yields an effective optical transit time τ_0 that is twice that of the transmission geometry. Fortunately this is easily compensated for by sufficient reduction of the stripline dimensions.

The second change in the experiment is made possible by the transition to the reflection-mode geometry. Because grinding and polishing of the GaAs is no longer necessary, very high-quality MBE or MOCVD GaAs may be used which will have

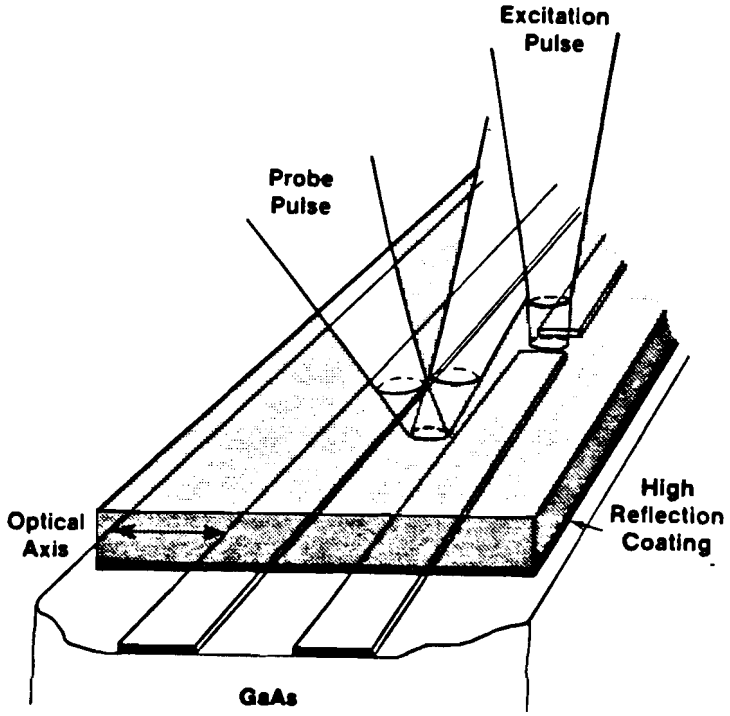

Fig. 4.4.4 Reflection-mode electro-optic sampling geometry.

extremely low impurity concentrations and correspondingly high electron mobilities. The use of epitaxial GaAs has an additional advantage in terms of ohmic contact formation. As discussed in Appendix A1, ohmic contacts require a heavily doped n^+ region between the metal and the semiconductor to serve as a source of electrons to the semiconductor. It is clear that the heavier and more uniform the doping the better the contact will be. Such a layer is easily incorporated into an epitaxial growth process as a cap layer and a very high-quality n^+-n interface is assured.

As expected, it was found that the uniformity and quality of the contacts increased dramatically with the utilization of epitaxial GaAs. The I-V curves were linear to fields as high as 50kV/cm with at most ± 5% variation of the I-V response for many samples across a wafer. The best metallization was found to be sputtered or annealed NiAuGe annealed in an argon atmosphere at 400°C for 10-15 minutes.

Experimental photoconductive transients for these samples are shown in Fig. 4.4.5 [99]. For this measurement the coplanar linewidths and separation were each 50μm, the gap length was 10μm, the pump and probe beam diameters were 10μm, and the propagation distance from the gap to the probe point was 20μm. The pump and probe pulsewidths were 65fs and the laser wavelength was 620nm. Although the data was taken with uniform illumination of the gap, it was found that the shape of the voltage transient did not depend critically on how the gap was illuminated.

The transient response of five samples each from a wafer of Cornell MBE GaAs and a wafer of Spire MOCVD GaAs were studied. The data of Fig. 4.4.5 is a representative set for a particular sample from the MBE wafer. All ten samples exhibited very similar overshoot behavior. The amplitude of the voltage transient varied with illumination, depending upon how much light was coupled into the photoconductive switch. Maximum switching occurred when the gaps were uniformly illuminated. The magnitude of the overshoot did not depend upon

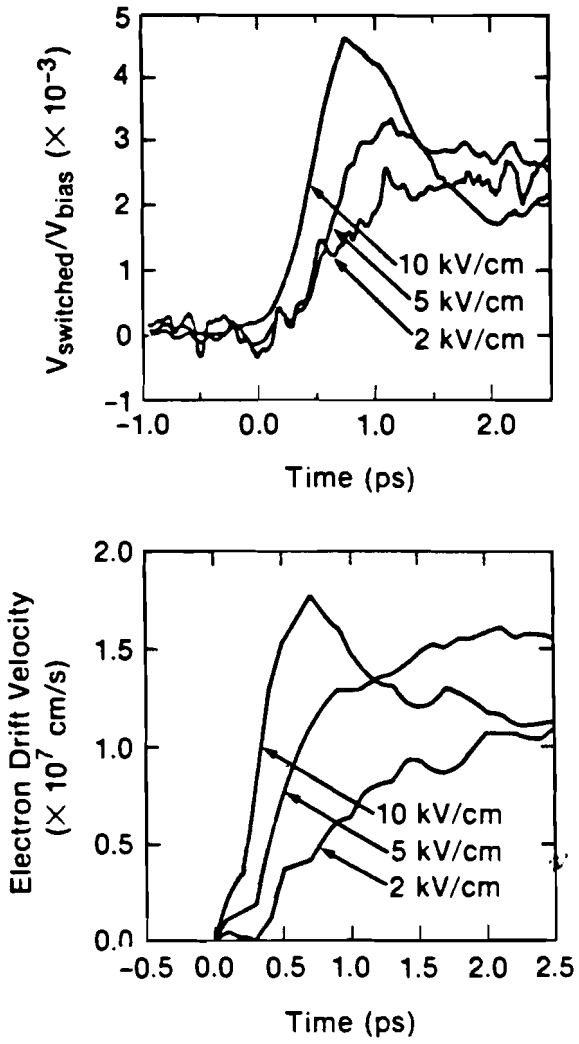

Fig. 4.4.5 Transient photoconductivity data and Monte Carlo drift velocity calculations for λ_{ex} = 620nm [99].

illumination. For the five MBE samples the degree of overshoot with E=10kV/cm was 2.10±.20 and for the five MOCVD samples the same result was 1.9±.23. The MOCVD samples displayed a slightly reduced degree of overshoot but the difference between the two samples is not statistically significant.

Also shown in the figure are Monte Carlo calculations of the electron drift velocity for the particular experimental conditions of electric field, temperature

(300K), excitation wavelength (620nm), and density (10^{17} cm^{-3}). All of the qualitative features of the theory are reproduced in the experimental results. These features include a decreasing risetime with increasing field and a moderate overshoot that occurs at the extreme high field. Note also that the magnitude of the high-field overshoot prediction of 1.6 is in qualitative agreement with the measured overshoots of 2.10±.20 and 1.9±.23. In section 4.2 it was shown that the temporal resolution for the sampling system with this geometry is under 200fs. The measured response is a convolution of the transient drift velocity with the system response. Because the system response is considerably faster than the predicted velocity transient the measurement should reflect the inherent velocity response with only slight instrumental broadening. Therefore, because considerable care has been taken to optimize the temporal resolution and to fabricate reproducible ohmic contacts on high-quality epitaxial GaAs, the conclusion is that this measurement constitutes the first subpicosecond time-resolved observation of velocity overshoot in GaAs.

Another phenomenon predicted by the Monte Carlo theory and discussed in the previous section is the Jones-Rees effect [98]. The signature of this effect is a delay in the onset of the drift velocity for low fields when electrons are photoexcited at or above the intervalley transfer threshold. In the experiment this should be apparent as a delay in the onset of the photoconductivity at low fields. The effect should be observed for excitation wavelengths shorter than 700nm.

Referring again to the data in Fig. 4.4.5 there is a shift that is apparent between the 10kV/cm and 5kV/cm curves. There is no visible shift between the 5kV/cm and 2kV/cm curves but this may be obscured by the relatively large noise level on the low field data. One way of quantifying the onset time of the photoconductivity is by measuring how long it takes for the transient voltage to reach 10% of its peak value at each field. These measurements are shown in Table 4.4.1

TABLE 4.4.1

Measurement of Jones-Rees Effect

compare t_{onset} (10% of peak)

	2kV/cm	5kV/cm	10kV/cm
Monte Carlo Predictions	0.4±.05	0.30	0.10pS
Photoconductivity Data	0.33±.05	0.31±.03	0.12±.02pS

and are compared with the relevant Monte Carlo predictions. The experimental values in the table are averaged over all ten MBE and MOCVD samples. For the high- and medium-field cases the agreement is very good, and for the-low field case the agreement is within the uncertainty of the data and the calculation (low-field Monte Carlo calculations suffer from numerical instabilities). This constitutes the first time-resolved measurement of the Jones-Rees effect in GaAs.

4.4.4 Near-IR (λ_{ex} = 760nm) Results

It was shown in section 4.3 that velocity overshoot increases as the photoexcitation energy approaches the bandgap because the electrons will spend a longer time in the central valley and therefore will have gained more energy from the field before scattering to the sideband. In an effort to measure an enhanced overshoot the transient photoconductivity experiment was repeated using the same optimized

samples as above but with photoexcitation and probing accomplished using a near-IR dye laser running at 760nm. Details of this laser source may be found in Appendix A2. Note that for absolute optimization of velocity overshoot a short-pulse high-repetition-rate laser running at 850nm should be used. At the time of this writing a laser with these properties has yet to be developed.

Transient photoconductivity data with 760nm excitation at the high and low

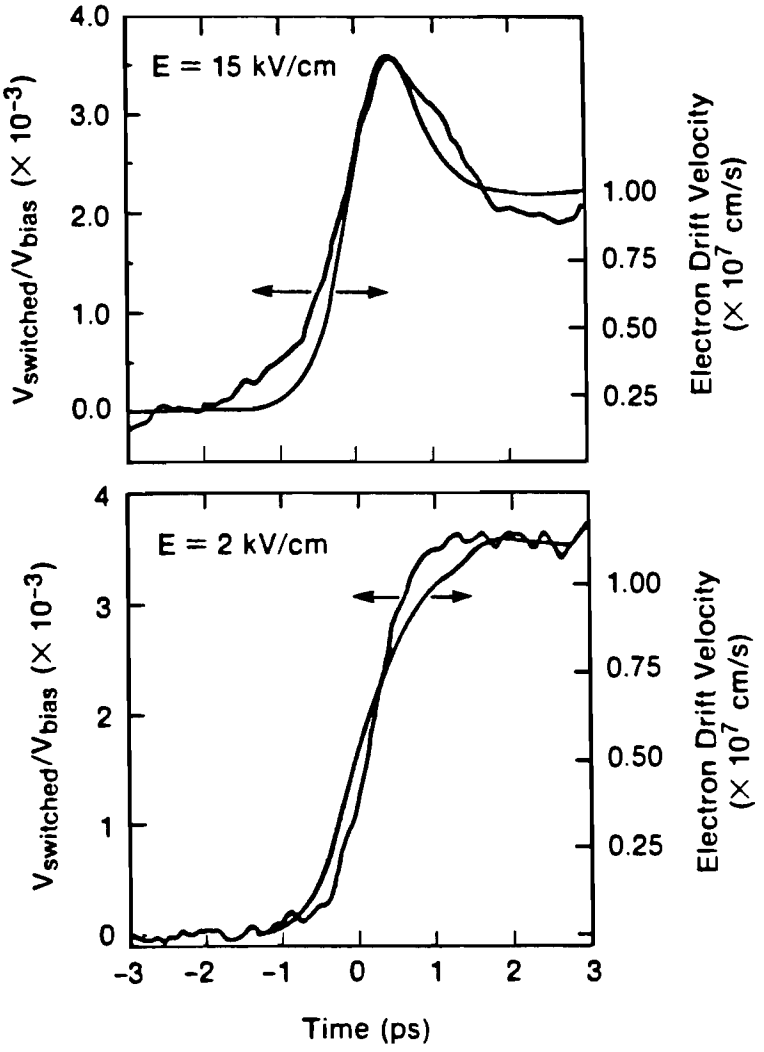

Fig. 4.4.6 Transient photoconductivity data and Monte Carlo electron drift velocity simulations for λ_{ex} = 760nm. Note that the Monte Carlo curves have in this case been convolved with a 500fs system response [99].

fields of 15kV/cm and 2kV/cm are shown in Fig. 4.4.6. The data is a representative set from one of the MBE samples. Note that once again a very significant photocurrent overshoot is apparent at high field but not at low field.However, for the high field case the degree of overshoot is much smaller and the risetime of the photocurrent is considerably slower than what is predicted by the Monte Carlo theory (Fig. 4.3.5). In this case the limited temporal resolution is understood. The near-IR laser produces pulses only as short as 300fs. Recall that the laser pulsewidth enters into the calculation of the temporal resolution twice, once for the probe pulse and once for the excitation pulse (eq. 4.2.4). In this case the non-negligible laser pulsewidth dominates the temporal resolution and therefore the full velocity overshoot cannot be resolved. Fortunately, since the temporal resolution is well known it is still possible to compare the data with the Monte Carlo predictions as long as the finite system response is taken into account. Specifically, if the theoretical predictions of Fig. 4.3.5 are convolved with the system response of 500fs then a realistic estimate of the amount of overshoot that may be observed in this measurement is obtained. These curves are also plotted in Fig. 4.4.6. Once again very good agreement between the experimental results and the (convolved) theoretical predictions is found.

For this experiment only the five MBE samples were studied. As was the case for the 620nm experiment, the amplitude of the transient voltage was found to vary with the illumination of the gap, and maximum switching was found for the case of uniform illumination. The degree of overshoot did not depend upon the illumination. The average of the five samples yielded an overshoot of 1.8±.25 in good agreement with the (convolved) Monte Carlo prediction of 1.64.

For this wavelength, as explained in the previous section, no Jones-Rees effect is expected. Unfortunately the question of whether or not there is a delay in the onset of the photoconductivity cannot be answered because the temporal resolution is

insufficient to resolve such a delay.

In this section the development of optimized samples, contacts, and sampling geometries to achieve a reproducible measurement of photocurrent overshoot has been described. Very good qualitative agreement has been obtained between transient photoconductivity results and Monte Carlo calculations of the transient electron velocity. In the next chapter an all-optical experiment will be described which is designed to measure not electron velocities but the electron distribution function. These two complementary approaches will yield a complete picture of the dynamic behavior of electrons in GaAs during heating by an applied electric field.

5.1 Review of Published Transient Absorption Studies

This section will review the body of work that has been published to date by various investigators on the study of relaxation of non-thermal carrier distributions probed via transient absorption spectroscopy. The different experiments have in common that they all studied the evolution of carriers photoexcited with a picosecond or subpicosecond laser source as the carriers move toward equilibration with the lattice. When performed under varying conditions of pump intensity, wavelength, and sample temperature these results yield important information about electron-electron, electron-hole, and electron-phonon scattering rates. The distinction between these previous experiments and the present one described in the following sections is that an electric field has been applied so that carriers experience heating as well as cooling to the lattice. The final steady state is therefore characterized by an electron temperature T_e which is not equal to the lattice temperature T_L. The details of this heating are critical to subpicosecond transport and velocity overshoot phenomenon, as will be discussed later in this chapter.

One of the limitations of this technique in the past has been the availability of subpicosecond laser sources at a pump and/or probe wavelength necessary to study a particular aspect of the problem. Because of this many of the experiments performed to date have been designed around a particular laser wavelength at hand. This situation is changing as subpicosecond continuum sources are developed in parallel with tunable dye lasers whose wavelength range may be changed through judicious selection of laser dyes. These developments will eventually result in the full realization of the potential of absorption spectroscopy techniques and the extension of these techniques to the study of transport in AlGaAs, InP, various new alloy materials, quantum wells, and other systems.

One of the first time-resolved absorption studies was carried out by von der

Linde and Lambrich [100]. In this work 25ps excitation pulses from a mode-locked Nd:YAG laser were used to create carriers in bulk GaAs via two-photon absorption. This resulted in an initial electron distribution with a large excess energy of 716 meV. The relaxation of this distribution to the band edge was measured with absorption at several wavelengths produced with a tunable optical parametric oscillator. Experimental results of induced absorption versus pump-probe delay obtained at T=7K are shown in Fig. 5.1.1. The data shows that the distribution has not completely relaxed even after 250ps. To interpret the data the authors assumed that immediately after excitation electron-electron scattering was efficient enough to produce a Fermi distribution with an elevated temperature T_e. This hot distribution then cooled down to the lattice temperature via LO phonon emission . Using the temperature T_e and the phonon relaxation time τ_{LO} as parameters to fit the theory to the data the authors obtained the temperature evolution of the distribution shown in

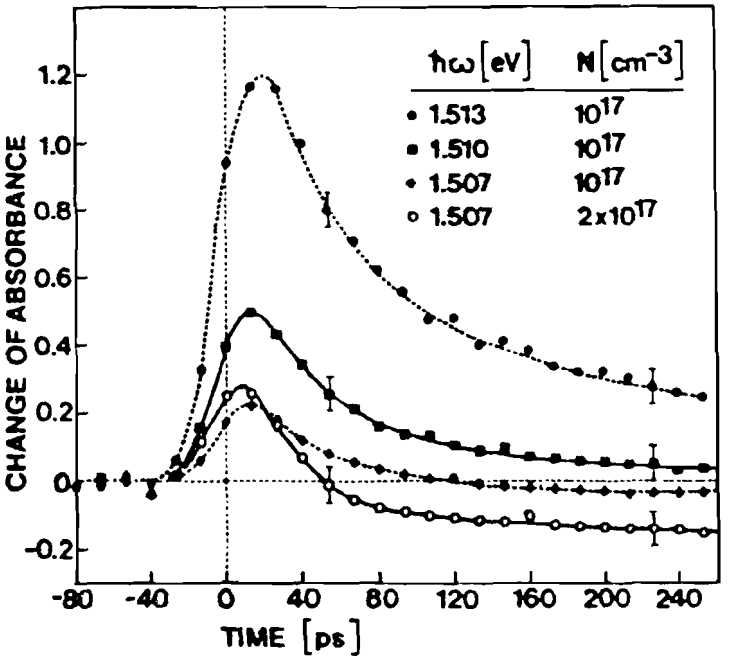

Fig. 5.1.1 Induced absorbance versus time for λ_{ex}=1.06μm and T_L=7K, with different probe wavelengths near the band edge [100].

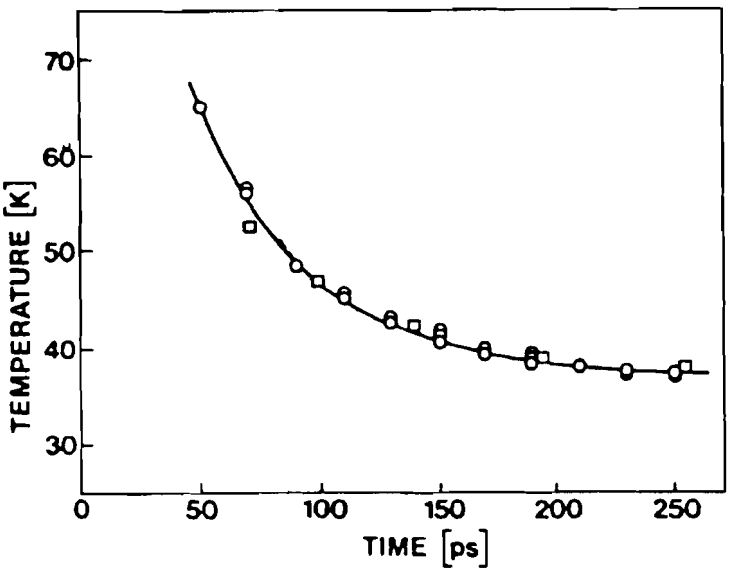

Fig. 5.1.2 Temperature evolution of the distribution derived from the data in Fig. 5.1.1 [100].

Fig. 5.1.2. The resultant value of τ_{LO} of 0.11ps is in good agreement with theory.

A significant improvement in the experiment was introduced by Leheny et. al. [101] with the utilization of a subpicosecond continuum probe. This allowed the transient absorption to be measured for a band of wavelengths near the band edge with improved temporal resolution. If the time-dependent transmission is plotted as a difference spectrum with respect to the unperturbed (t<0) data then the resultant function is approximately equal to the joint electron/hole distribution function $f_e + f_h$ (this will be discussed in detail in the next section). The results of Leheny et. al. for T_L=10K and λ_{ex}=750nm are shown in Fig. 5.1.3. The first panel is the unperturbed transmission spectrum, and the other panels show the difference spectrum for various pump-probe delays. The tail in the spectrum at higher energies which gradually disappears corresponds to electrons high in the band which gradually cool to the band edge.

Leheny et. al. also assumed that the carrier distribution could be described

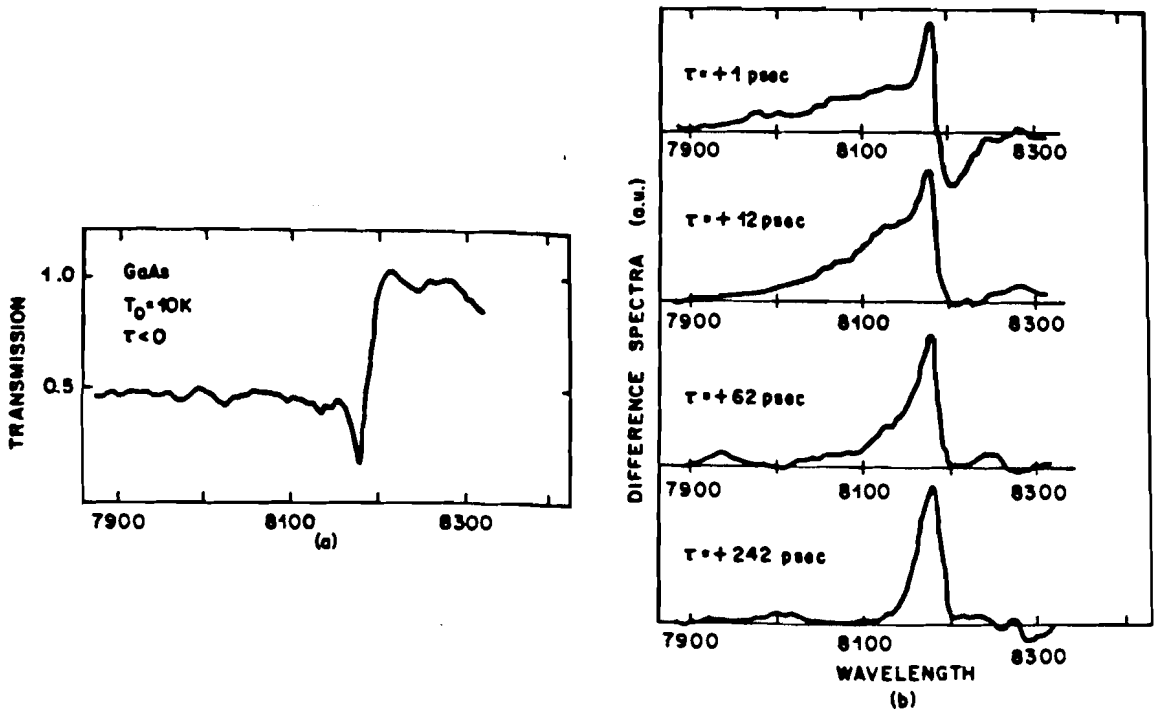

Fig 5.1.3 Transmission spectra for various pump-probe delays obtained with λ_{ex}=750nm, T_L=10K, and n=7x10^{16}cm^{-3} [101].

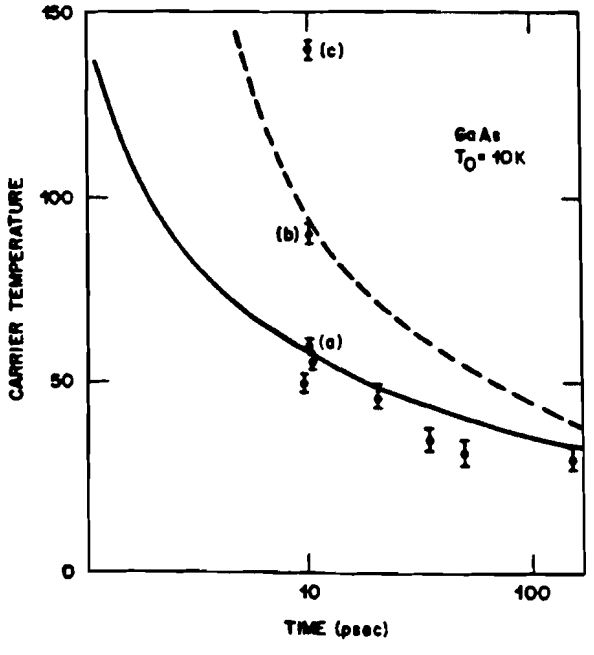

Fig.5.1.4 Temperature evolution of the distribution derived from the data in Fig. 5.1.3. (a) n=7x10^{16}cm^{-3}; (b) n=3x10^{17}cm^{-3}; (c) n=1x10^{18}cm^{-3}. The dashed line is the prediction if the LO phonon scattering rate is reduced by a factor of 5 [101].

with a Fermi function. The evolution of the fitted Fermi temperature is shown in Fig. 5.1.4. The authors found that the distribution cooled more slowly for higher excitation densities (points (b) and (c) in the figure). The dashed curve is the predicted cooling curve if the LO phonon emission is reduced by a factor of 5, which is consistent with the predicted screening of the phonons due to electron-phonon coupling at higher densities. At the highest density of $n=1x10^{18}cm^{-3}$ (point (c)) the distribution has a high energy tail which cannot be fit with a simple Fermi function.

A similar experiment was performed by Oudar et. al. [20] and subsequently analyzed in detail by Collet et. al. [102]. In this case carriers were photoexcited near the band edge (λ_{ex}=814nm) with a 0.5ps narrow-bandwidth (5meV) pump pulse, and a 0.1ps continuum probe pulse was used to measure the induced absorption. The evolution of the difference spectra, obtained at T_L=15K, is shown in Fig. 5.1.5. The peak in the data at t=0.6ps corresponds to the temporal peak of the excitation pulse. This feature is referred to as dynamic spectral hole burning because the presence of a peaked distribution of carriers bleaches the optical transmission at the peak of the distribution. At t=1.8ps the peak is nearly washed out and at t=4.2ps the carriers have relaxed to a quasi-Fermi distribution. Note that the excitation wavelength was chosen so that the initial energy of the electrons (19meV) would be insufficient to create LO phonons (ε_{LO}=37meV) and hence the dynamics in this case are dominated by carrier-carrier scattering.

The theoretical description of the experiment utilized a moderately sophisticated model of the dynamic plasma that included electrons and holes, electron-electron and electron-hole interactions, LO phonons (including hot phonons), and screening of the plasma dielectric function. There were no phenomenological fitting parameters in this model. The theoretical results are plotted in Fig. 5.1.5 as triangles (quasi-static screening) and solid circles (static screening). As can be seen in the

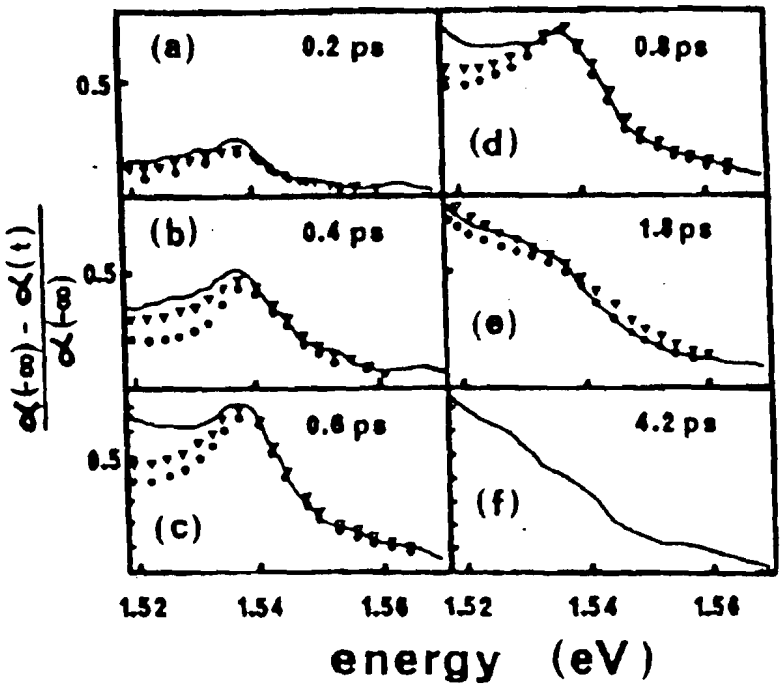

Fig. 5.1.5 Evolution of the distribution function with λ_{ex}=814nm and T_L=15K. The points are the theoretical predictions discussed in the text [102].

figure, the fit is quite reasonable. The authors were able to draw several important conclusions from their analysis: (1) holes gain energy from the electrons during the transient and have not equilibrated with the electrons even after 1.4ps; (2) hot phonon effects are not important for these experimental parameters; and (3) the static approximation for the dielectric function is a good approximation.

Recent improvements in CPM laser design to achieve pulses as short as 27fs [103] have led to transient absorption studies with femtosecond resolution. One such experiment by Rosker et. al. [104] measured the femtosecond absorption dynamics of electrons in AlGaAs, GaAs, and a multiple quantum well structure, using a single-wavelength (630nm) transmission correlation technique. This technique measures the rate of scattering out of the initial photoexcited state (and perhaps scattering back into that state at later times). Typical room-temperature results are shown in Fig. 5.1.6 (in each case the dashed line is the pulse autocorrelation of 50fs). The difference in

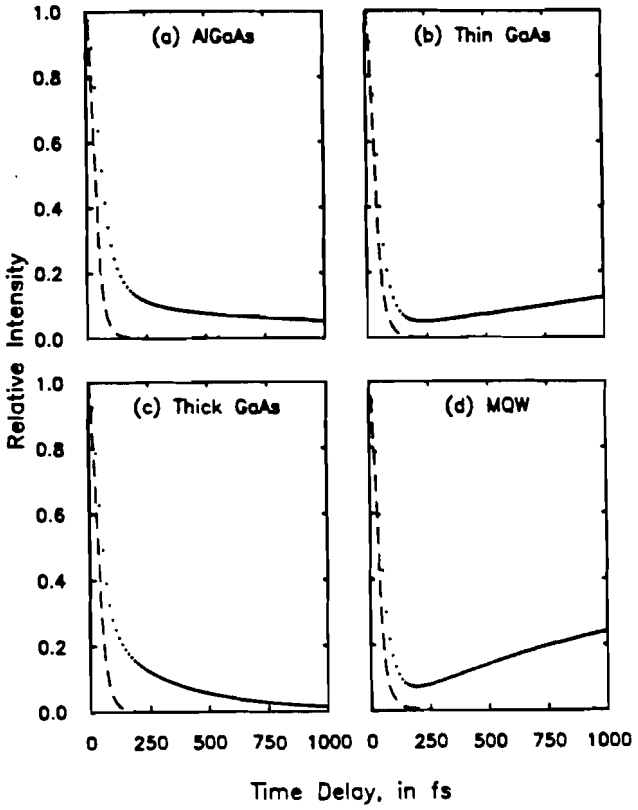

Fig. 5.1.6 Room-temperature transient absorption for different samples obtained with the single-wavelength (630nm) transmission-correlation technique [104]

response between the thin (0.3μm) and thick (1.1μm) GaAs samples was attributed to uniform and non-uniform excitation densities respectively. Through careful analysis of the data the authors were able to show that for all cases the response was the sum of three exponential terms. For the thin GaAs sample these terms were two decaying exponentials with time constants of 34fs and 160fs and an increasing exponential with a time constant of 1.7ps. The fast component is attributed to intervalley scattering, in reasonable agreement with predictions based on estimates of the deformation potential constant, with a possible additional contribution from electron-electron scattering. The intermediate time constant is assigned to polar optical phonon scattering within the Γ valley and the 1.7ps increase in transmission is attributed to electrons returning to the Γ valley from the L valley. Wise et. al. [105] have also carried out an extension of

this work to lower temperatures which enables distinctions between the intervalley and carrier-carrier scattering contributions to the fast decay component.

Another study of femtosecond absorption was carried out by Schoenlein et. al. [106] with similar excitation conditions (625nm) but in this case a continuum probe, which gives a more complete picture of the distribution relaxation to the band edge. Room temperature experimental results for a thin GaAs sample probed at various wavelengths from near the band edge to 2.14eV are shown in Fig. 5.1.7. Several features are apparent. The short peak in the data from 2.14eV to 1.88eV indicates the spectral width of the excitation peak and is another example of spectral hole burning. This feature is spectrally broader than the pump bandwidth because optical transitions from both the heavy and light hole bands are allowed. This data also shows an increase in the transmission at 1.78-1.94eV after 1.5-2ps, again indicating return of electrons from the L to the Γ valley, consistent with the data of

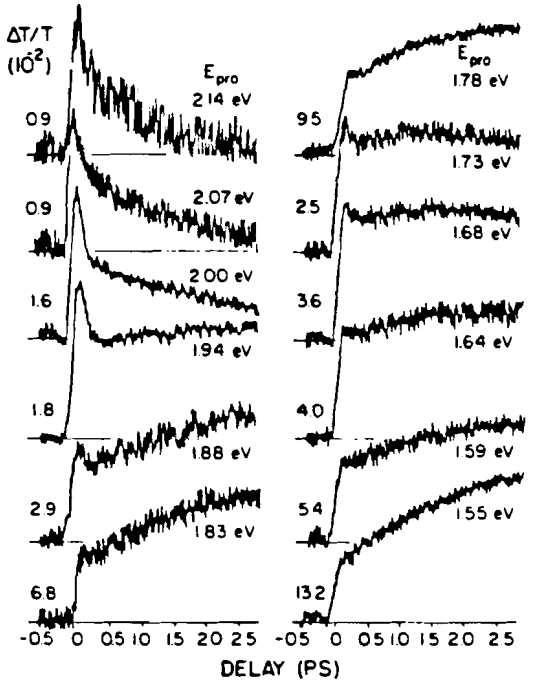

Fig. 5.1.7 Transient absorption data for λ_{ex}=625nm, probed at numerous wavelengths with a continuum probe [106].

Rosker et. al. discussed above. Another small but sharp peak is apparent at 1.73eV and 1.68eV which is attributed to spectral hole burning due to the optical transition from the split- off hole band to the conduction band. The rising absorption near the band edge reflects the time necessary for most of the hot electrons to cool through LO phonon emission.

Finally, the transient absorption has been measured by Knox et. al. [21] and modeled by Bailey et. al. [107] for a room-temperature AlGaAs/GaAs quantum well. In this case a 50fs continuum probe was used and excitation was accomplished with a 100fs pump pulse 20meV above the band edge. As in the experiment of Oudar described above, this excess energy is insufficient for LO phonon emission and therefore the dynamics are determined by carrier-carrier interactions only. The experimental results are shown in Fig. 5.1.8 for a concentration of $2x10^{10}cm^{-2}$ and

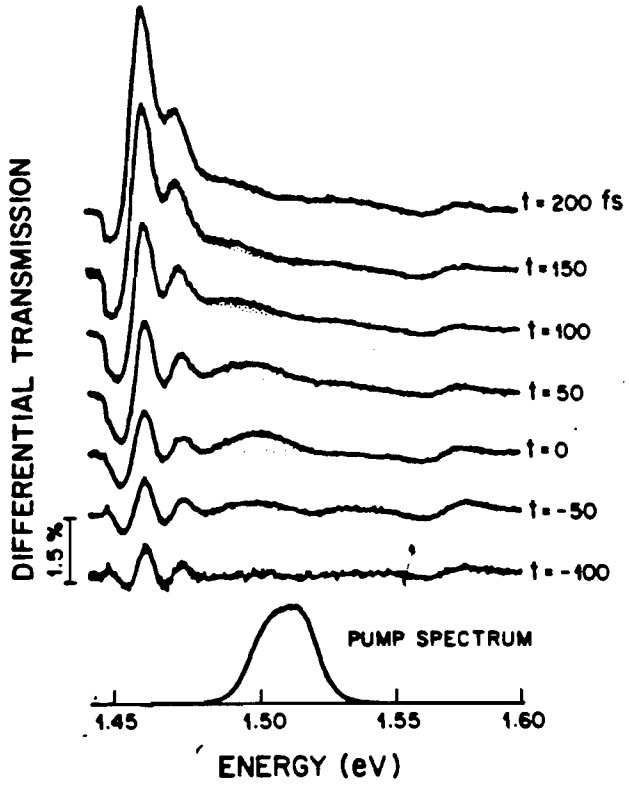

Fig. 5.1.8 Room-temperature transient absorption spectra for near-band edge excitation in a AlGaAs/GaAs multiple quantum well structure [21].

various pump-probe delays. In the unperturbed (t<-100fs) spectrum the first two peaks correspond to the n=1 light and heavy hole excitons, and the small feature at 1.58eV is the n=2 heavy hole exciton. The photoexcited distribution is scattered out of its initial state within 50-100fs and relaxes to the band edge, indicated by bleaching of the n=1 exciton absorption, in approximately 150fs. The model of Bailey et. al. is a Monte Carlo simulation that includes polar optical phonon, ionized impurity, electron-hole, and electron-electron scattering mechanisms. The model reproduces the fast (50-100fs) relaxation out of the initial state and shows that this rate, governed by electron-electron scattering, is density dependent above concentrations of $4x10^{10}cm^{-2}$. An additional feature of the theory predicts that for low densities the initial relaxation is slower, on the order of 200fs, which remains to be experimentally verified.

This section has reviewed the published studies of hot electron relaxation probed with transient absorption spectroscopy. Experiments have been carried out under various conditions of pump intensity and wavelength, temperature, and temporal resolution, yielding an important body of information regarding carrier-carrier and carrier-phonon scattering and screening. The rest of this chapter will describe a modification of this system with the application of an electric field, which serves as an additional source of energy and momentum for the carriers and resembles more closely the environment experienced by hot carriers in many semiconductor device structures.

5.2 Monte Carlo Model of the Dynamic Electron Distribution Function

The use of transient absorption techniques to measure the shape of the dynamic electron distribution function is based upon the bleaching of optical transmission due to the presence of excess carriers in the conduction and valence bands. The dynamic absorption coefficient may be written as [21]

$$\alpha(t) = \alpha_0 \{ 1 - f_e(t) - f_h(t) \} \qquad [5.2.1]$$

where α_0 is the unperturbed (time-independent) coefficient and f_e and f_h are the respective photoexcited electron and hole distribution functions. The transmission of a thin sample, neglecting interference effects, may be written as

$$T = (1 - R)^2 e^{-\alpha L} I_0 \qquad [5.2.2]$$

where R is the reflection coefficient, L is the sample thickness, and I_0 is the incident intensity. For small changes in transmission the exponential may be expanded and it is easily shown that the differential transmission has the form

$$\frac{\Delta T}{T} = \frac{T - T_0}{T_0} \approx (\alpha_0 L)(f_e + f_h) \qquad [5.2.3]$$

Therefore if the transmission data is plotted in this way the shape of the joint distribution function is obtained directly.

Recall that from the discussion in Chapter 4 that during velocity overshoot electrons are accelerated in the Γ valley under the applied field and eventually scatter into the L valley when they have gained sufficient energy. In terms of the energy distribution this implies that the distribution will develop a high-energy "tail". The measurement of the arrival time at high excess energies for electrons accelerated from the band edge amounts to a measurement of the scattering time into the L valley, which is of fundamental importance to velocity overshoot theories.

The Monte Carlo model is identical to that described earlier with a few

modifications. Due to experimental limitations transient absorption experiments tend to be performed at higher densities than transient photoconductivity measurements (as high as $n=5x10^{18}cm^{-3}$), which requires the inclusion of electron-electron and electron-hole scattering effects. The finite spectral width of the excitation pulse (10meV) has been included in the initial distribution. The excitation wavelength for the experiments is 830nm, which generates electrons with an excess energy of 60meV. This corresponds to approximately two LO phonon energies above the band edge. The holes are initialized with an energy of 7meV below the valence band edge. The sample is assumed to be at T=300K in all cases. The electron and hole distribution functions will be calculated as a function of pump/probe delay, carrier density, and applied field.

A calculation of the relaxation of the hole distribution with $n=10^{17}cm^{-3}$ and E=0 is shown in Fig. 5.2.1. The very nonthermal initial distribution is randomized quickly and after 200fs has evolved into a quasi-Fermi distribution. Note that all of

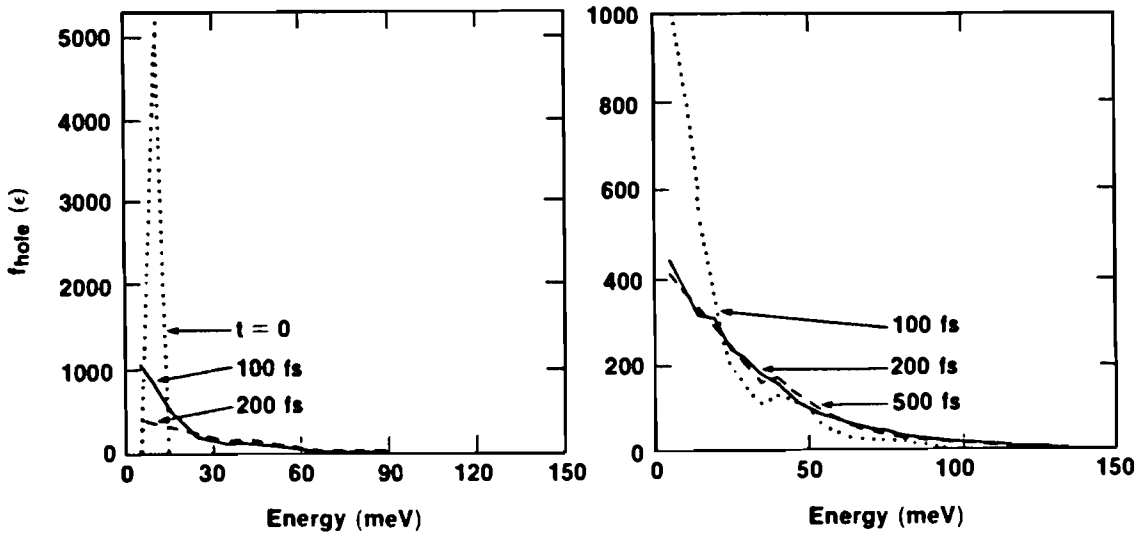

Fig. 5.2.1 Calculated evolution of the hole distribution with E=0 and $n=10^{17}cm^{-3}$.

the important dynamics take place within 50meV of the band edge. The experiment is focussed on detecting changes in the tail of the distribution (above 100meV), where the hole contribution is negligible, so the remainder of this discussion will be limited to the electron distribution.

Relaxation of the electron distribution function under the same conditions is shown in Fig. 5.2.2. The initial (t=0) distribution has two peaks due to simulated photoexcitation from both the light hole and heavy hole bands. It should be noted that the calculation assumes isotropic valence bands, whereas in GaAs the hole effective masses are anisotropic [97]. The effect of a range of hole masses is to broaden the initial photoexcited electron distribution. Therefore the calculation will underestimate the width of the initial experimental distribution. At t=100fs the distribution has two peaks, one at the initial photoexcitation energy and one at ε=30meV. The lower-energy peak is at exactly one LO phonon energy below the initial peak, indicating that LO phonon emission is a dominant scattering mechanism during the first 100fs. After 200fs both peaks have been smeared out by electron-electron and electron-hole

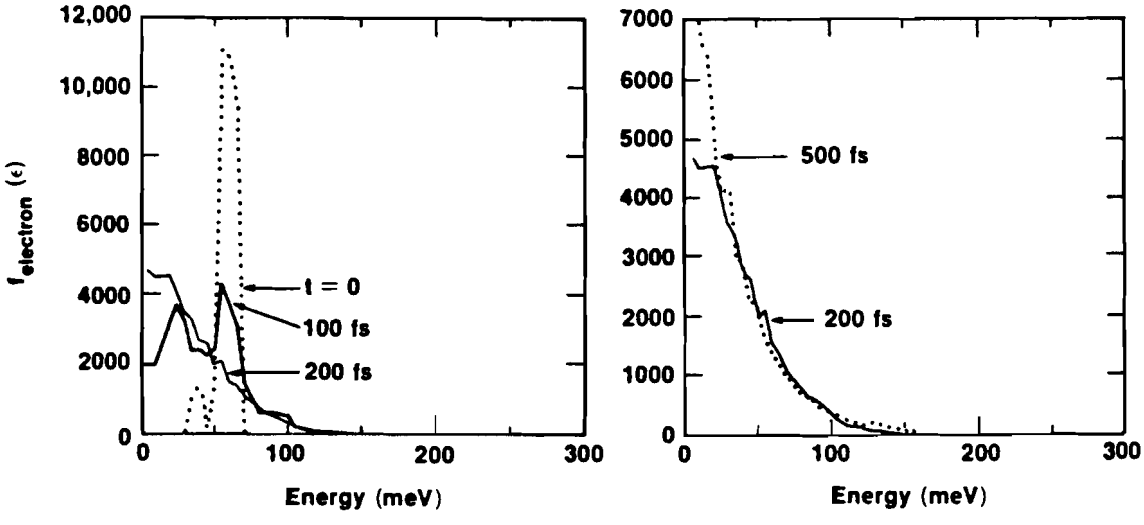

Fig. 5.2.2 Simulated evolution of the electron distribution for E=0 and $n=10^{17}cm^{-3}$.

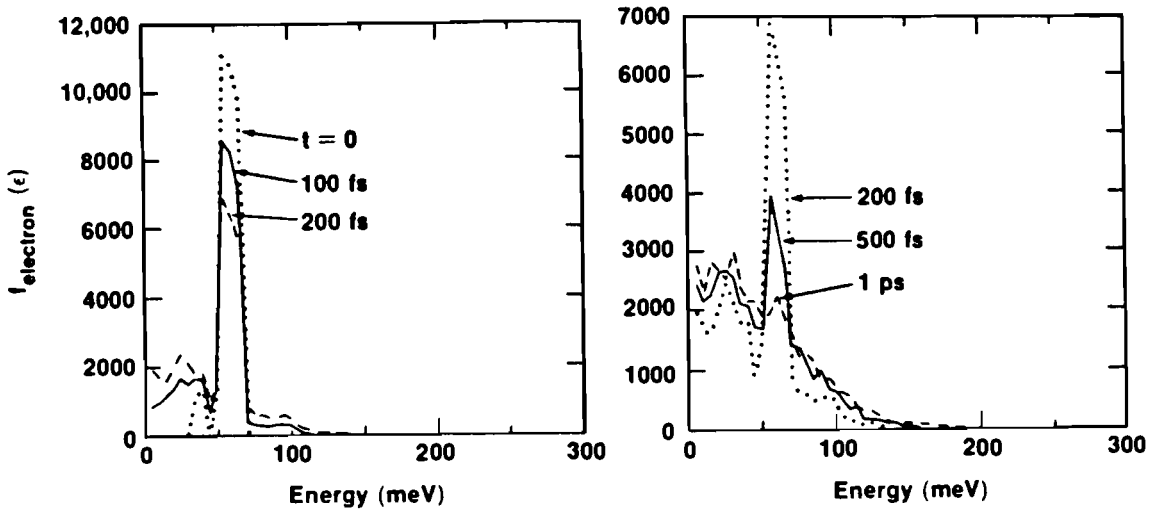

Fig. 5.2.3 Calculated evolution of the electron distribution,E=0 and $n=2x10^{18}cm^{-3}$.

scattering and the distribution is nearly thermalized. This 200fs time scale for thermalization is consistent with calculations of Collet [102] and Bailey [107] discussed in the previous section.

A simulation for the same conditions but with a moderately high carrier density of $n=2x10^{18}cm^{-3}$ is shown in Fig. 5.2.3. The behavior is significantly different. In particular, the initial peak persists for up to 500fs and no LO phonon peak is apparent. The persistent peak is due to two factors. First, at a density of $2x10^{18}cm^{-3}$ the electron gas is moderately degenerate, and the scattering rate out of the initial state is limited by the number of states available to scatter into. Secondly, electron-hole scattering transfers energy to the hole distribution and prevents the immediate build-up of a high-energy tail. In this case the electrons are thermalized in approximately 1ps. As will be discussed in the next section, no such long-lived non-thermal peak has been observed in the experiments. The experiments were consistently conducted at as low a density as possible, estimated to be $n=2x10^{17}cm^{-3}$, in order to avoid degeneracy and electron-hole effects. For these reasons the

remainder of the discussion will be limited to densities on the order of $10^{17}cm^{-3}$.

Next, a DC electric field is turned on in the simulation. Calculations for the high-field case of E=10kV/cm are shown in Fig. 5.2.4. As expected, the applied field has a dramatic effect on the evolution of the distribution. A high-energy tail begins to form immediately and there is no LO-phonon peak. After 500fs the tail continues to grow and significant numbers of electrons have energies as high as 300meV, sufficient to scatter into the L valley (recall that for E=0 there were essentially no electrons with energies higher than 150meV). Beyond t=1ps the distribution continues to shift as electrons scatter back and forth between the Γ and L valleys, and equilibrium is reached after 2-3ps.

A different way to visualize the dynamics of the distribution function is to look at the distribution at discrete energies above the band edge as a function of time. This corresponds to performing the experiment with discrete probe wavelengths rather than with a continuum probe, which will be discussed in the next section. Three probe wavelengths of interest are λ_{probe}=870nm, 780nm, and 750nm, corresponding approximately to respective energies of 100, 150, and 200meV above

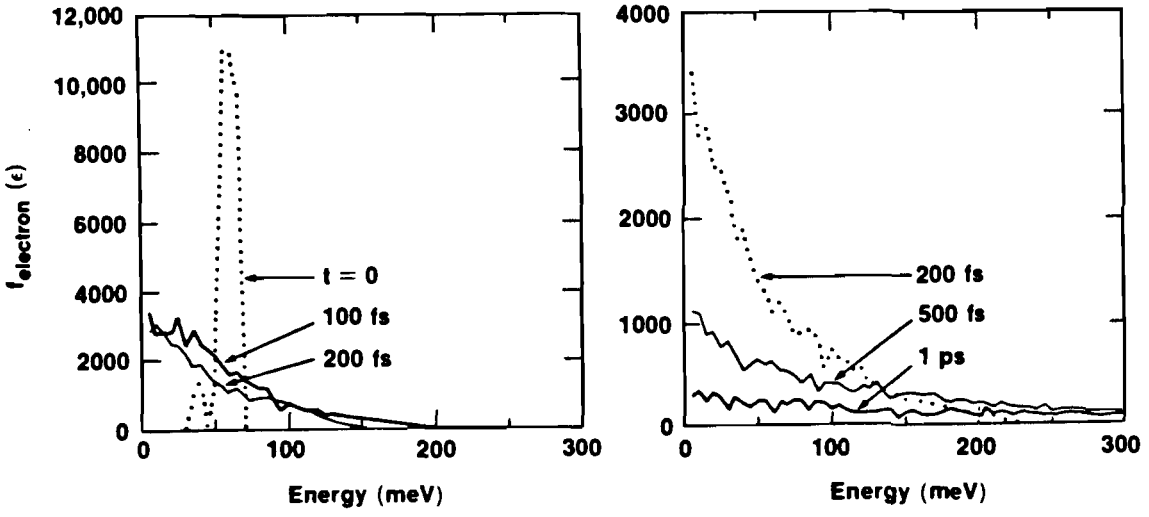

Fig. 5.2.4 Simulated evolution of the electron distribution function, including heating by the applied electric field, for $n=10^{17}cm^{-3}$ and E=10kV/cm.

the band edge. In the following plots the distribution function at these wavelengths will be weighted with the absorption coefficient ($\alpha(100meV)=10^4cm^{-1}$; $\alpha(150meV)=1.2x10^4cm^{-1}$; $\alpha(200meV)=1.34x10^4cm^{-1}$), in accordance with eq.[5.2.2] to allow for more direct comparison with the experimental results.

The data of Fig. 5.2.2 ($n=10^{17}cm^{-3}$, E=0) is replotted in Fig. 5.2.5 for these three probe wavelengths to demonstrate the advantage of this perspective. It can be seen immediately from this graph that there are fewer electrons at higher energies and that they arrive later the further one probes from the band edge. As already discussed, with no applied field there are extremely few electrons with energies as high as 200meV.

Fig. 5.2.6 simulates the same conditions but with the addition of the high applied electric field (E=10kV/cm). Two effects are apparent. A "population overshoot" occurs at all three wavelengths as electrons are accelerated up from the band edge, arrive at the probe energy, and sweep past to move to higher energies.

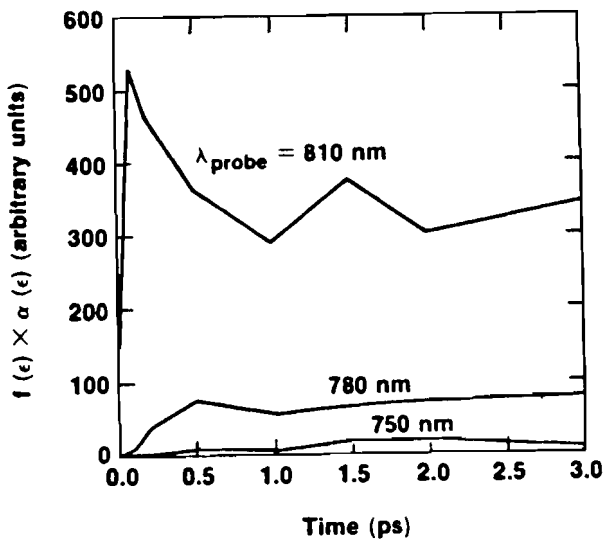

Fig. 5.2.5 The calculations of Fig. 5.2.2 ($n=10^{17}cm^{-3}$, E=0) are replotted for three discrete energies of interest as a function of pump/probe delay. The data is also weighted with the absorption coefficient.

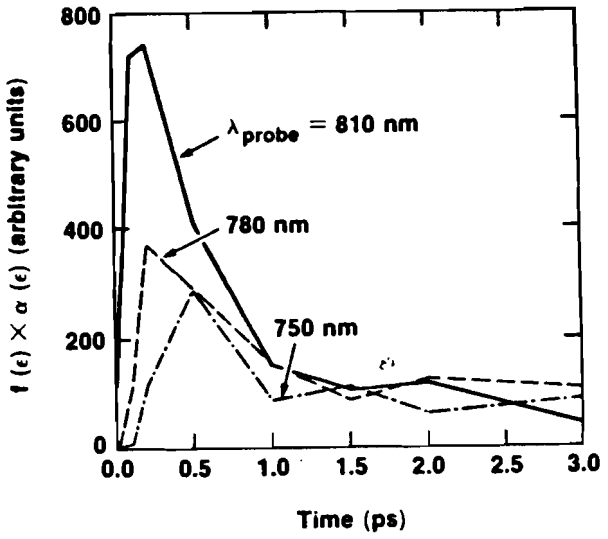

Fig. 5.2.6 Evolution of the electron distribution function at discrete energies for $n=10^{17}cm^{-3}$ and E=10kV/cm.

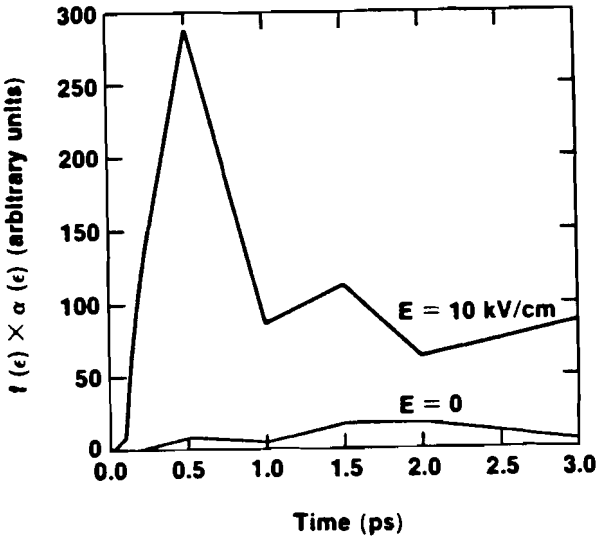

Fig. 5.2.7 Comparison of the time dependence of the electron distribution function at ε=200meV for high field and zero field conditions.

Again a delay is seen as the arrival of the electrons is probed further from the band edge. Also note the very significant number of electrons in this case at ε=200meV (probe=750nm) This is emphasized in Fig. 5.2.7, which compares the distribution function at 200meV with and without the applied field. Essentially all of the electrons at this or higher energies have arrived there because of heating from the applied field.

In summary, Monte Carlo calculations predict that an applied electric field should have a dramatic effect on the evolution of the electron distribution function. A high-energy tail is expected to develop as electrons gain energy from the field. In particular, it should be possible to measure to measure a transient absorption above 200meV which is significantly enhanced when a high electric field is applied.

5.3 Experimental Results: Subpicosecond Heating and Thermalization of the Electron Distribution Function.

This section will describe the transient absorption experiments that have been performed with an applied electric field. The experiment will be described in two modes, with a continuum probe and with discrete probe wavelengths. The experimental results will be compared with the theoretical predictions of the previous section.

5.3.1 Preparation of Transient Absorption Samples

For theses measurements epitaxial MBE GaAs wafers were obtained from Cornell University and Spire Corporation which consisted of 500Å 10^{18} n^+-GaAs/ 5000Å undoped GaAs/ 2μm undoped $Al_{0.6}Ga_{0.4}As$ grown on a semi-insulating GaAs

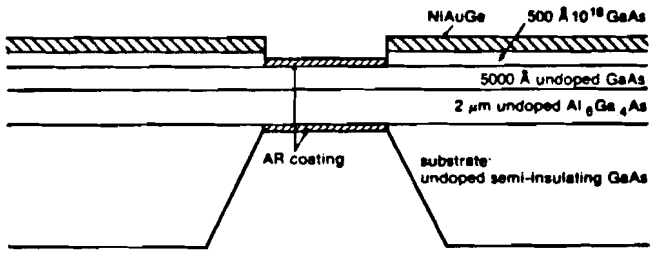

Fig. 5.3.1 Sample structure for the transient absorption spectroscopy experiment.

substrate. The AlGaAs serves as structural support for the thin undoped GaAs layer; it is optically transparent at the wavelengths of interest here. The final sample structure after fabrication is shown in Fig. 5.3.1. The fabrication steps will be described below.

The first step was to dice the wafers into squares of 4x4 or 5x5 chips, each chip having dimensions of 5mmx5mm. The edges of the 4x4 or 5x5 squares would serve later in the process as registration marks for patterning of the back surface. NiAuGe lines 100 and 200μm wide were fabricated on the "top" surface of the samples using the liftoff process previously described. Each line had a 100μmx100μm or 200μmx200μm gap in the middle of the line. The metal pattern was utilized as an etch mask to remove the n^+-GaAs layer between the lines using the calibrated GaAs etch. The NiAuGe was then annealed for ten minutes at 400°C. It should be noted that the metallization on the front surface was designed only to provide a DC bias to the sample. Unlike the photoconductivity experiment, in this

case it is not necessary to propagate voltage waveforms in a high-speed transmission line, which is why the single line/gap pattern was utilized.

The next step was to thin the thickness of the sample from initially 500μm down to approximately 50-75μm by lapping the back side of the pieces. Then the back sides were coated with photoresist and large (0.5mmx0.5mm) windows were imaged in the resist using the edge of the samples for registration. This assured that the holes etched up through the substrate would line up with the gaps on the top surface. The calibrated GaAs etch, which selectively etches GaAs and not AlGaAs, was used to etch the holes through the back side, stopping at the AlGaAs layer. In order to insure uniform etching, the samples were mounted on a teflon magnetic stirrer which rotated the samples in a beaker while a continuous flow of etchant was pumped onto the sample through a pipette. In this way all of the samples on a 4x4 or 5x5 square etched through to the AlGaAs layer at the same time. Completed etching was indicated when the etched windows became partially transparent, demonstrating an orange color when illuminated from the back side.

The last step was to add an anti-reflection coating to both surfaces of the sample. This is necessary because the reflectivity of GaAs in th visible band is ~30%, which not only yields optical losses but can also result in significant interference effects in the sample. Dielectric coatings were designed at the Optical Coating Facility at the University of Rochester which consisted of a quarter-wave layer of magnesium fluoride (thickness=1090Å) on top of a quarter-wave layer of zinc sulfide (thickness = 650Å). The coatings were sputtered onto one surface, the samples were removed from the chamber and turned over, and then the opposite surfaces were coated. This resulted in reflection losses of less than 2% from either surface from 600 to 900nm.

The samples were mounted on glass slides in which 5mm holes had been drilled. The particular chip and gap of interest was aligned over the hole and the

sample was tacked down using silver paint or photoresist. This prevented any losses or reflections of the pump or probe beams due to glass interfaces. The voltage bias and load were provided through coaxial cables attached to the glass slides and connected to the sample with silver paint.

5.3.2 Description of Data Acquisition Techniques

This section will describe the details of the techniques that were used to acquire the transient absorption data that will be discussed in the following sections. First the techniques for measuring a broad-band spectrum will be presented, and then the approach used to perform transient absorption experiments at discrete wavelengths with improved sensitivity will be discussed.

Data acquisition throughout these experiments was achieved using a PDP/11-23 computer.For broadband spectrum acquisition, the computer was interfaced with the optical multichannel analyzer (OMA) controller via a DMA parallel interface board. The delay line stepper was controlled via RS232 communications. Data was stored using 32-bit double precision on 8" floppy disks. All of the programs for these experiments were written at the Laboratory for Laser Energetics in the FORTH language.

The spectrometers used in these experiments were Instruments SA .32 meter monochromators in the Czerny-Turner configuration, utilizing 300-line gratings. The detectors were Hammamatsu type RO66 head-on 1.5"-diameter extended-red photomultipliers which were connected for pulsed operation (e.g. hot cathode biasing). For the broad-band spectra an EGG PARC 1420R-1024-G OMA with an extended-red gated intensified microchannel plate was used. This OMA had 700

active intensified channels with a corresponding resolution of 8Å.

The discrete pump/continuum probe arrangement is shown in Fig. 5.3.2. Not shown in the diagram are Uniblitz mechanical shutters that were placed in both the pump and probe beams to enhance sensitivity in the following way. Noise in these measurements is due to laser amplitude fluctuations and dark-current noise in the detectors, both of which can be subtracted out to some degree. In order to achieve this the following sequence was programmed for the OMA:

1) open both shutters; reset array; accumulate 1 scan; store in first memory register.

2) close pump shutter; reset array; accumulate 1 scan; subtract

3) close probe shutter; reset array; accumulate 1 scan; add

4) open pump shutter; reset array; accumulate 1 scan; subtract

5) switch to second memory register

6) open probe shutter; reset array; accumulate 1 scan

7) close probe shutter; reset array; accumulate 1 scan; subtract

Steps 1-4 resulted in a measurement of ΔT=(pump on - pump off) with the dark noise and scattered pump light subtracted out, which was stored in register #1. The transmission of the probe beam with the dark noise subtracted out was performed in steps 6 and 7 and the result was stored in register #2. The PDP then read the two registers and divided channel 1 by channel 2 to arrive at $\Delta T/T$. Each scan was an integration over 0.1 seconds (100 laser shots). The sequence was typically repeated 4000 times for an average of 4×10^6 laser shots per point in the averaged spectrum. This was done for a particular fixed pump/probe delay. The delay was then changed by stepping the delay line a known distance and the measurement was then repeated. In this way the entire spectrum of the probe beam could be accumulated for a series of pump/probe delay times.

There are two difficulties with the above sequence, having to do with short-term and long-term laser stability. Because each step in the program has a duration of 0.1 seconds, laser fluctuations on a time scale shorter than that cannot be subtracted out. On the other hand, during the one hour that it took for a measurement at a single pump/probe delay, the temperature of the Nd:YAG pump or amplifier may have drifted, which could cause drift in the amplitude or shape of the continuum spectrum. This limited the reproducibility of this technique from one long scan to the next to $\Delta T/T=\pm 1\%$. This aspect of reproducibility will be discussed further in the next section.

The principle of probing at discrete wavelengths and corresponding experimental results will be presented in section 5.3.4. The modified arrangement, showing only the probe beam, is detailed in Fig. 5.3.6. Instead of an OMA, two matched spectrometers were used, and the mechanical shutters were eliminated. Because the probe transmission was being measured at a single wavelength data acquisition could occur at a high repetition rate, specifically the laser repetition rate of 1kHz. This meant that long and short-term laser fluctuations could be subtracted out and normalized on every laser shot, which resulted in an order of magnitude improvement in sensitivity. The PMT outputs were integrated with a Lecroy 2249W gated AD integrator; the gate was synchronized to the laser pulse train with a Chronetics delayed pulse generator.

The response of the two detectors had to be carefully matched. This required that the two detectors monitor precisely the same portion of the white-light spectrum. The wavelength calibration was carried out using interference filters, and the spectrometer slit widths were matched. The detector signal levels were adjusted by placing appropriate neutral density filters in front of the spectrometers. In addition, both PMT's were biased with the same voltage supply at -1100V so that bias-related

noise would track in both detectors.Tracking of the two detectors was characterized by accumulating a scatter-plot of the amplitude of one detector signal versus the other. Optimized sensitivity could be achieved by insuring that the two detectors tracked each other to within ±5%. It should be noted that this is close to the detector shot-noise limit; if a higher photon flux is allowed on the photomultipliers in order to reduce the shot noise, the PMT's will begin to saturate.

The experiment proceeded as follows. For each pump/probe delay 1000 laser shots were averaged and then the stepping motor was advanced to the next position. For each position the computer read the signal from the two detectors, subtracted them, multiplied the result by a large constant (because the difference was a small number), and then divided by the reference level. The result was later converted into an absolute $\Delta T/T$. A typical scan consisted of 50 pump/probe delays separated by an (equivalent) time-step of 30fs. Each scan was then repeated 20-40 times and the scans were accumulated and averaged to average out long-term drifts in the laser. The resultant data was an average of $2\text{-}4\text{x}10^4$ laser shots averaged on a shot-to-shot basis.After storing an averaged scan the applied field was changed to a different value of interest and the procedure was repeated. As will be discussed in section 5.3.4, this approach resulted in improved reproducibility and a sensitivity of $\Delta T/T=1\text{x}10^{-3}$.

5.3.3 Continuum Probe Results

The dye laser and regenerative amplifier utilized to generate the white-light continuum for this experiment will be described in Appendix A2. The output of the laser system is a train of high peak-power pulses with energies of 10uJ/pulse, a wavelength of 620nm, a duration of 100fs, and a repetition rate of 1kHz. These

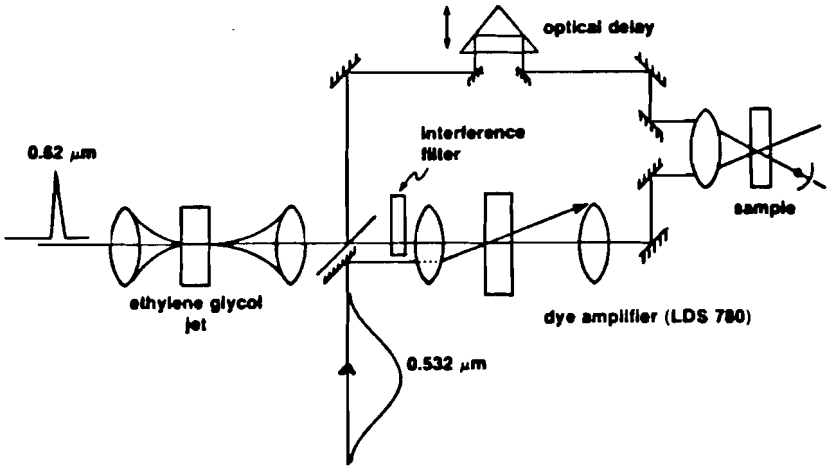

Fig. 5.3.2 Discrete pump/continuum probe arrangement.

pulses, when focussed into a jet of ethylene glycol, water, or other medium, have sufficient peak power to generate a continuum through the high-intensity nonlinear index response of the material [108]. The discrete pump/continuum probe arrangement is shown in Fig. 5.3.2. The continuum maintains the original 100fs pulsewidth but the spectrum has broadened to cover the range of 400-900nm, which results in an extremely useful subpicosecond spectroscopic tool.

After the white light is generated it is split into two beams. The probe beam passes through a computer-controlled optical delay line, then is focussed through the sample and the entire spectrum is recorded with an optical multichannel analyzer (OMA). Not shown in the figure is the compensation for the chirp on the probe pulse. Continuum generation with a relatively thick (1mm) jet results in a pulse in which the red frequencies are leading the blue, which is referred to as a "chirped pulse". In a femtosecond spectroscopy experiment all of the probe wavelengths must arrive at the same time. The chirp is corrected by passing the probe beam through a pair of high-index glass prisms [109]. In this way the chirp was reduced to 50fs across the 700-850nm band of interest, which is quite reasonable for a 100fs pulse duration.

In the pump beam the pump wavelength of interest (in this case 830nm) is selected out with a 10nm bandwidth interference filter. The energy of the pump pulse is boosted with a single-stage dye amplifier which is pumped with leftover light from the regenerative amplifier. The result is as much as 20nJ per pulse in the pump beam. The pump energy was adjusted during the measurements to yield densities of approximately $2x10^{17}cm^{-3}$. The pump beam was aligned parallel with the probe beam and was focussed into the sample through the same 50mm lens.

The pump and probe pulses were timed by placing a sum frequency generation (SFG) crystal at the sample position and performing a cross-correlation measurement. In addition, it was necessary to carefully overlap the focussed spots of the two beams at the sample position to optimize the transient absorption. This was accomplished by mounting a 12.5μm pinhole adjacent to the sample and scanning it

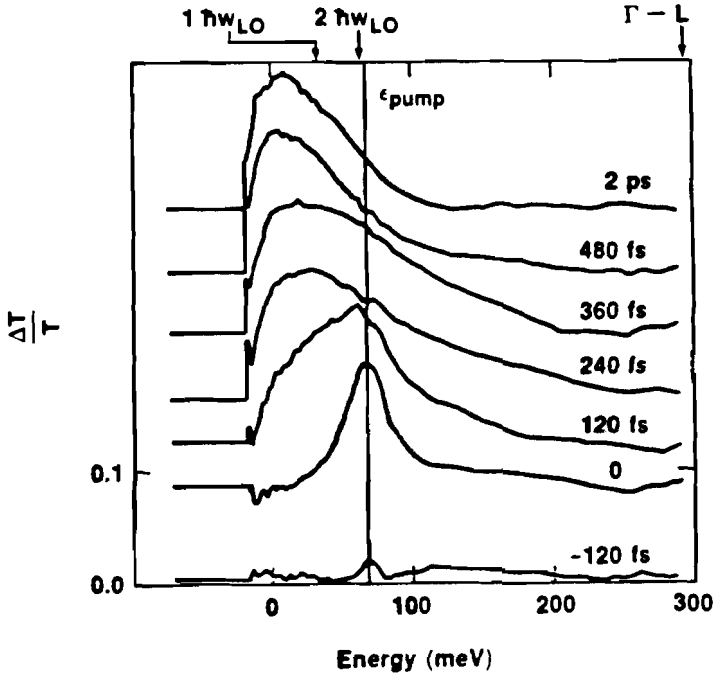

Fig. 5.3.3 Experimental transient absorption data for E=0, $n=2x10^{17}cm^{-3}$, and various pump/probe delays. The pump energy, LO phonon energies, and intervalley scattering threshold are indicated.

both vertically and horizontally across the pump and probe spots. In this way the probe beam could be precisely centered over the pump beam. The probe beam diameter was typically 70μm and the pump diameter was 120μm.

Experimental transient absorption curves for E=0 and $n=2x10^{17}cm^{-3}$ are shown in Fig. 5.3.3 for various pump/probe delays. The curves are plotted versus energy from the GaAs band edge and each is offset vertically for clarity in the figure. Each curve required approximately 20 minutes of integration. The time origin is somewhat arbitrary and was chosen to coincide with the peak of the initial nonthermal distribution. Some contribution from the leading edge of the excitation pulse can be seen at t=-120fs. The distribution thermalizes rapidly and after 240fs has become a quasi-Fermi distribution. These results may be compared directly with the Monte Carlo predictions of Fig. 5.2.2. The presence of the LO-phonon peak at 120fs is indicated by a shoulder in the experimental distribution at ε=30meV; this feature is not sharper because of the finite duration of the pump pulse (the Monte Carlo simulation does not take into account the temporal extent of the pump pulse). Note also that there

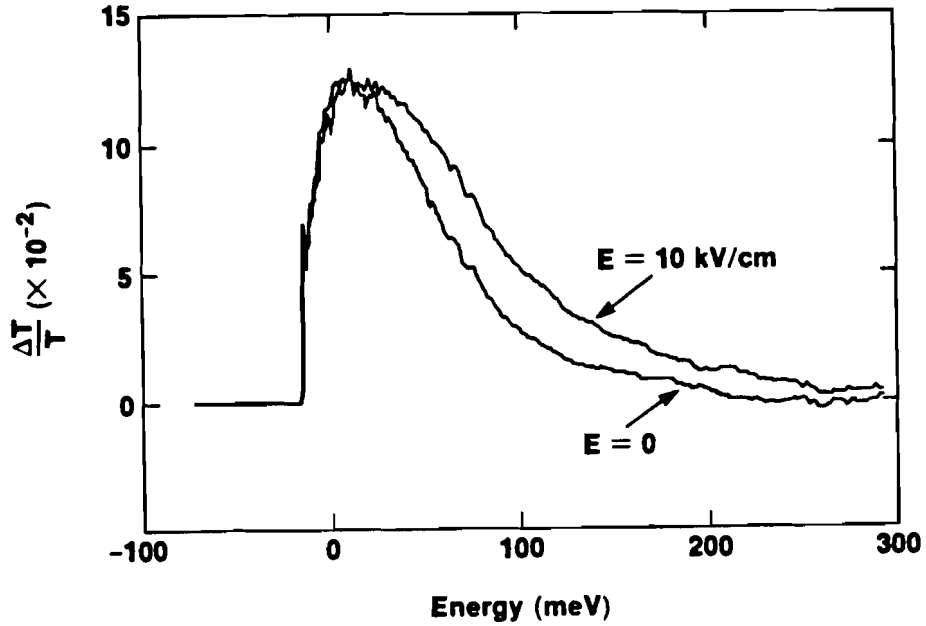

Fig. 5.3.4 Comparison of the measured electron distribution at t=480fs for E=0 and E=10kV/cm.

is no evidence of a long-lived nonthermal peak such as is predicted for $n=2x10^{18}cm^{-3}$ (Fig. 5.2.3). The agreement between experiment and theory is very good for E=0 and a density on the order of $10^{17}cm^{-3}$.

A measurement of the effect of a 10kV/cm electric field for a fixed pump/probe delay of 480fs is shown in Fig. 5.3.4. As expected, the presence of the field enhances the transmission at shorter wavelengths, indicating a higher electron population in the tail of the distribution. Unfortunately it was found that the degree of this transmission enhancement was not very reproducible. Only two MBE samples were studied in this experiment. The small number of samples was due to two reasons First, Spire MOCVD samples that had also been prepared were found to have a large dark current. This rendered them useless because they were likely to break down at high fields. Second, the thinned samples were very fragile and yields were low. There were two sources of variation within the experiment: between the two samples and from one long data acquisition to the next. As a reproducibility test, one of the samples was measured with E=0 for three different 30-minute data scans. The peak of the induced transmission near the bandedge was repeatable to within ±0.5% for the three scans, but the amplitude of the tails varied significantly. Specifically, the average value for $\Delta T/T$ at 100meV was 3±1%.

The second source of variation was from one sample to the other. The absolute magnitude of $\Delta T/T$ depended critically on the quality of the overlap between the pump and probe beams, which is why a detailed overlap procedure was developed. For this reason it was not possible to make quantitative comparisons of the magnitude of $\Delta T/T$ between the two samples.

Broad-band probe measurements are complicated by the fact that the shape of the white-light spectrum tends to "wobble" even when all components have been optimized, which limits the sensitivity of the measurement to 2% changes in

transmission. This is the same order as the expected changes in the tail of the distribution. For these reasons it was decided to proceed with the experiment using discrete probe wavelengths, a technique which improves the sensitivity by an order of magnitude.

5.3.4 Discrete Probe Results

The principal of probing at discrete wavelengths is illustrated in Fig. 5.3.5 with the data of Fig. 5.3.3 used as an example. The three probe wavelengths selected are 810nm, 780nm, and 750nm, corresponding to electron energies of 100, 150, and 200meV respectively. As explained in section 5.2, with no applied field there are never very many electrons with energies as high as 200meV, so only a very small transient absorption signal is expected at that energy. When a field is applied, however, electrons are heated by the field, a high-energy tail develops, and the transient absorption should be enhanced.

The simplest way to probe at discrete wavelengths would be to put interference filters in the probe beam in front of the sample. This is not an ideal situation because changing filters tends to misalign the pump/probe overlap and the optical delay introduced by each filter varies from one filter to another. This makes it difficult to make precise comparisons for different wavelengths. Instead, the full probe spectrum is focussed through the sample and the discrete wavelengths are selected after the sample. One other modification is necessary, shown in Fig. 5.3.6. A beamsplitter placed in the probe beam divides it into two beams, one which passes through the sample and one which serves as a reference. The reference and probe beams are detected with matched spectrometers and PMT's. The spectrometers are set

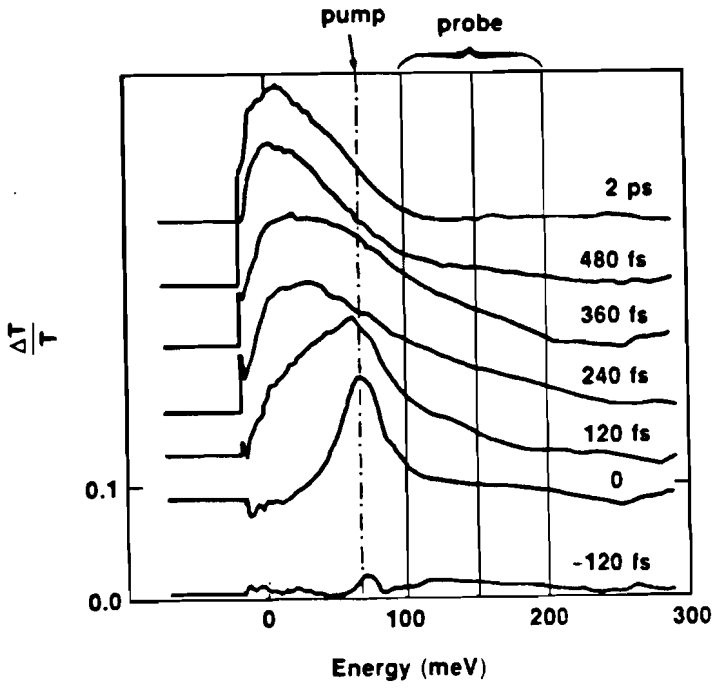

Fig. 5.3.5 Discrete versus continuum probing of transient absorption.

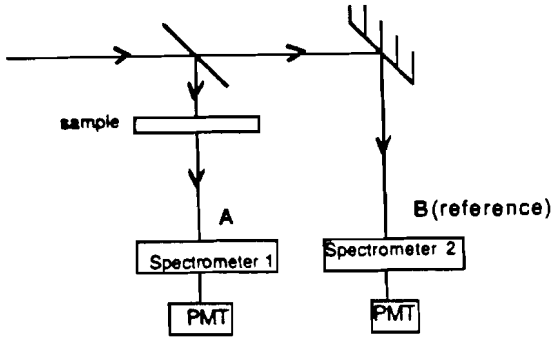

Fig. 5.3.6 Details of the differential technique used in the discrete probe wavelength mode.

to the discrete wavelengths of interest. By taking the difference spectrum between the probe and reference beams and normalizing to the reference amplitude the pulse-to-

pulse amplitude fluctuations in the white-light spectrum may be subtracted out, which yields an order of magnitude improvement in sensitivity. The sensitivity limit in this mode is a change in transmission of $1x10^{-3}$.

Experimental results for E=0 and $n=2x10^{17}cm^{-3}$ are shown in Fig. 5.3.7. The arrival of the electrons at ε=100meV is immediate, limited in this case by the pump pulsewidth. Electrons arrive later for ε=150meV and there are fewer at that energy. At the extreme energy of 200meV they arrive later still and there are so few that the transient absorption is barely detectable. These results may be compared with the predictions of Fig. 5.2.5; all of the qualitative features of the theory have been reproduced in the measurement.

The next step is to apply a DC bias to the sample. A 100V bias across a 100μm gap should result in a uniform field in the sample of 10kV/cm. The voltage switched across the gap was monitored on the load side of the gap with a high-speed oscilloscope. Under no conditions was the switched voltage greater than 0.5% of the applied voltage, indicating that the photoexcited density was low enough to induce

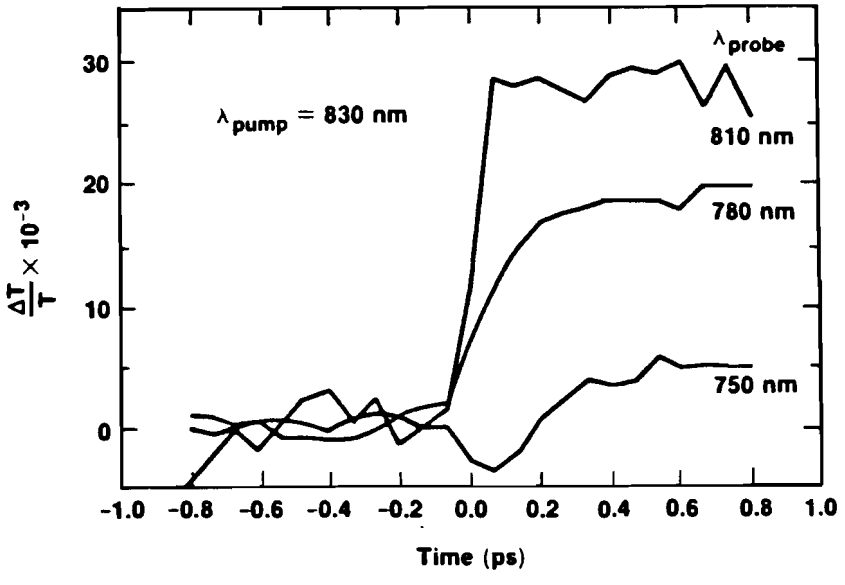

Fig. 5.3.7 Transient absorption data for three discrete wavelengths with E=0 and $n=2x10^{17}cm^{-3}$.

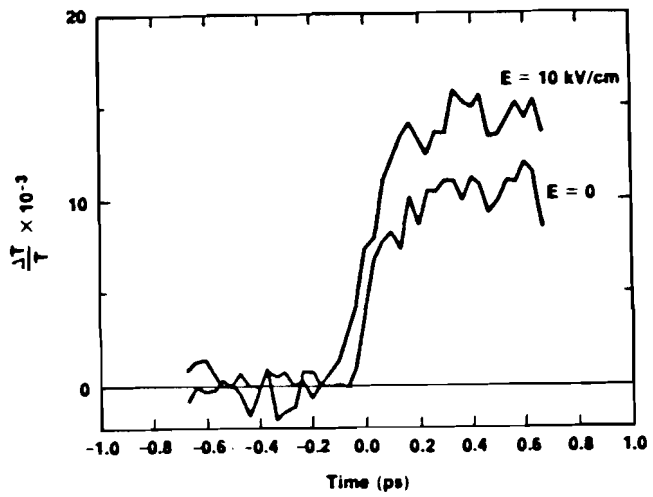

Fig. 5.3.8 Transient absorption data with λ_{probe}=780nm for high field and zero field conditions.

only a small perturbation in the applied field. This justifies the assumption of a time-independent field in the Monte Carlo simulation.

Transient absorption data for the intermediate probe wavelength of 780nm (ε=150meV) is shown in Fig. 5.3.8 for both E=0 and E=10kV/cm. Clearly. there is an enhancement of the transmission with the applied field and the onset occurs earlier in time. This indicates that there are more electrons at this point in the band and they arrive sooner with an applied field, as expected. However, there is no sign of the large "population overshoot" (Fig. 5.2.6) discussed in section 5.2 and predicted for a 10kV/cm field. This discrepancy will be discussed below.

The degree of the observed heating effect is quite reproducible. For one MBE sample the average of three separate 30-minute scans resulted in $\Delta T/T=10.4\pm1.2\times10^{-3}$ at t=400fs and E=0. Three separate long scans were run again for E=10kV/cm, yielding $\Delta T/T=14.9\pm0.8\times10^{-3}$ at t=400fs. Only one long scan was taken at each of the two fields for the second MBE sample. At t=400fs the results were $\Delta T/T$=7.3 for

E=0 and ΔT/T=10.5 for E=10kV/cm. The fact that ΔT/T was generally lower for the second sample was probably due to non-optimum pump/probe beam overlap.

Transient absorption data for the extreme wavelength of 750nm (ε=200meV) is shown in Fig 5.3.9 for E=0 and E=10kV/cm. Although the signal-to-noise is not large in this measurement it is clear that there is an enhancement of the transmission when the field is applied. In fact there are so few electrons in this point in the tail of the distribution with E=0 that they cannot be detected. It may be said that a transient absorption signal was observed with the field on but could not be detected in the absence of the field, in qualitative agreement with the predictions of Fig. 5.2.7. Again the effect was not as large as predicted and no overshoot of the transmission was observed

. Only one 30-minute scan was accumulated at this probe wavelength at E=0 and E=10kV/cm for each of the two MBE samples. For one sample the results were

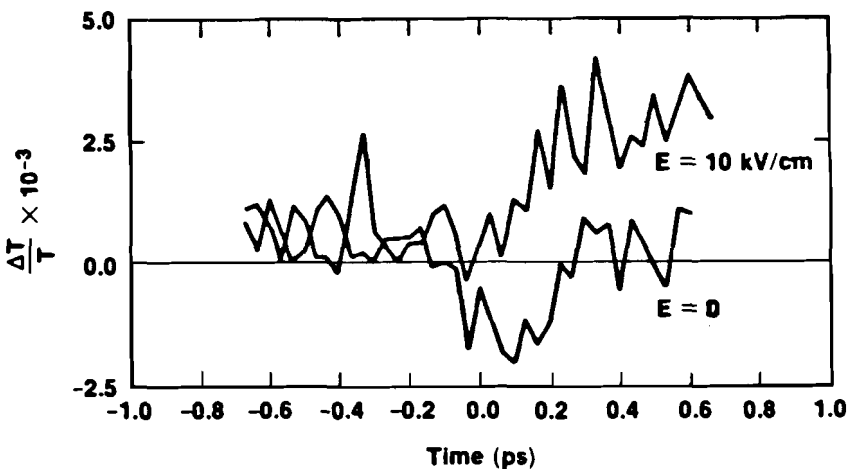

Fig. 5.3.9 Transient absorption data with λ_{probe}=750nm for high field and zero field conditions.

$\Delta T/T=2.4$ for E=10kV/cm and $\Delta T/T=0.3$ for E=0. For the other sample it was found that $\Delta T/T=1.9$ for E=10kV/cm and $\Delta T/T=-.05$ for E=0. In both cases a transmission increase was observed with an applied field and a pump/probe delay of 400fs that was clearly larger than the 1% noise level.

The data in figures 5.3.8 and 5.3.9, when compared with the Monte Carlo predictions, indicate the presence of a field but one which is much smaller than $E=V_B/L$. This could be due to poor contacts, but the contact fabrication used (n-GaAs/n^+-GaAs/AuGeNi) is essentially identical to that used for the transient photoconductivity samples. More likely is the formation of a stable high-field Gunn domain in the sample, which occurs when the background doping n_0 or the sample length L or both are too large. When the domain forms all of the applied field appears across the domain (at the anode) and the field in the rest of the gap is suppressed to a level below the threshold field of 3.8kV/cm. The role of Gunn domain formation in GaAs photodetectors has been discussed by Wei et. al. [110]. A linearized calculation by Jeppesen and Jeppsson [111] will be used to estimate the domain width for the samples parameters used here.

In Fig. 5.3.10 is plotted the domain width L_D relative to the gap length L for different applied biases and for representative values of the background doping. A polaron measurement of the doping versus depth for one of the absorption samples revealed that the doping level was $2x10^{18}cm^{-3}$ near the surface (the n^+ cap layer), fell to $5x10^{16}cm^{-3}$ in the undoped n-GaAs layer, exhibited a spike up to $1x10^{18}cm^{-3}$ at the GaAs/AlGaAs interface, and fell to $5x10^{16}cm^{-3}$ in the AlGaAs layer. The spike may be due to contamination at the interface or formation of a 2-dimensional electron gas. The relevant number is that in the GaAs and AlGaAs layers the background doping is $5x10^{16}cm^{-3}$. Referring to Fig. 5.3.10 indicates that the extent of the domain under these conditions is 10-15% of the sample length. In other words, the high-field

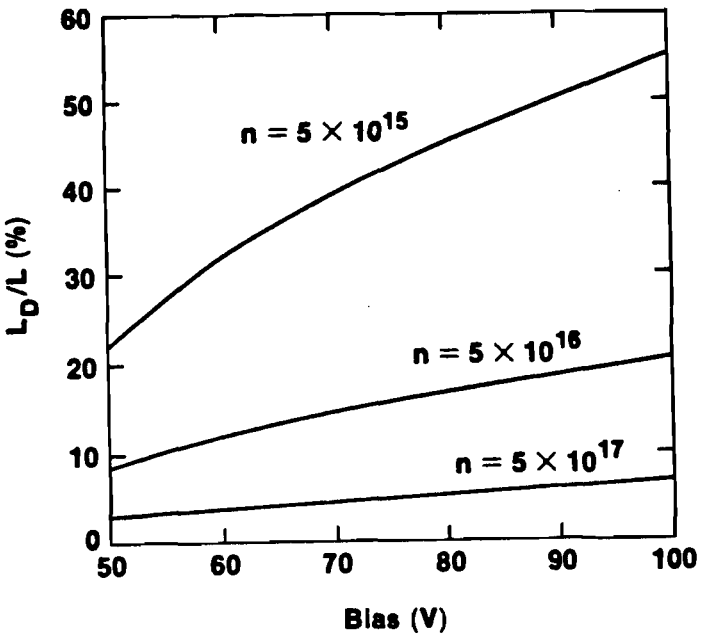

Fig. 5.3.10 Calculation of the extent of the high-field domain versus bias for several representative doping levels.

region is limited to the domain within 10-15μm of the anode; the field in the remainder of the sample is less than 3.8kV/cm. This is consistent with the transient absorption data, which indicated the existence of a field but one considerably smaller than the applied field.

An attempt was made to focus the probe beam more tightly in order to sample the high-field domain close to the anode, but the smallest spot size attainable was 30μm, which was not small enough to resolve the domain.

There are several improvements in the experiment that could be carried out to defeat the domain formation. The primary solution is to reduce n_0L. L is easily reduced by fabricating shorter gaps. The $5x10^{16}cm^{-3}$ background doping in the GaAs layer is not ideal; that material can be grown with much lower background levels. In addition, the AlGaAs layer could be removed with a selective etch from the back side of the sample. This would eliminate the AlGaAs contribution to the domain formation (the background level in the AlGaAs is about as low as can be expected with current

MBE technology). Also it might be possible to pulse-bias the voltage on a time scale which is shorter than that required for domain formation but long enough to insure that displacement currents do not play a large role in the experiment.

The question arises as to why there was no indication of a nonuniform field in the transient photoconductivity measurements in chapter 4. In that case L was 10μm and the measured background level was $5x10^{14}cm^{-3}$. This yields an n_0L product of $2x10^{11}cm^{-2}$, which is below the threshold for stable domain formation estimated by Jeppesen and Jeppsson to be $(n_0L)_{threshold}=1.5x10^{12}cm^{-2}$; in that case it is reasonable to assume that the internal field is uniform and given by $E=V_B/L$.

In this section experimental details of the transient absorption measurement have been described. Using the continuum probe approach relaxation of the initial nonthermal electron distribution on a 200fs timescale has been observed, in good agreement with Monte Carlo predictions and results published in the literature. Some heating of the distribution due to an applied electric field was observed but was not extremely reproducible.

In the discrete probe wavelength mode the experiment was repeated with an order of magnitude improvement in sensitivity. In this case an enhancement of the transient absorption was consistently observed with the application of the field, and in the high-energy tail of the distribution a transient signal was measured with the field applied that fell below the limits of sensitivity when the field was turned off. These results are in qualitative agreement with the Monte Carlo predictions, but indicate that the field in the sample is much lower than expected. A reasonable explanation of this discrepancy is that due to stable Gunn domain formation in the sample, most of the applied field appeared across the domain near the anode. Suggestions were described for future work to defeat the formation of the Gunn domain and perform the experiment with a uniform field.

6. Conclusions

The purpose of this work has been to develop and utilize experimental techniques capable of time resolving the dynamics of photoexcitedelectrons in GaAs under the influence of an applied electric field during the first few hundred femtoseconds of transport. The specific phenomenon of interest was velocity overshoot, which is of fundamental importance to the operation of a wide range of modern sub-micron semiconductor devices. Existing experimental evidence for this phenomenon has been reviewed and found to be, at best, incomplete.

The approach taken here has been to concentrate on measurements that yield direct information about the transient electron drift velocities and energies and that maintain the necessary temporal resolution. The only techniques currently available with sufficient temporal resolution are all-optical or hybrid electro-optic measurements that utilize ultrafast dye lasers. One classic experiment is the measurement of transient photoconductivity, which probes the drift velocity of an ensemble of carriers drifting in a bulk sample by measuring the current induced in the external circuit by the motion of the carriers. This technique has been used extensively from DC down to the nanosecond and picosecond time scales, and in this work has been extended into the subpicosecond regime.

Monte Carlo calculations of the transient electron drift velocity for our particular experimental conditions of temperature, electric field, excitation wavelength, and carrier density have been developed. They have been compared with the temporal evolution of voltage waveforms generated by a GaAs photoconductive switch. It has been shown in a qualitative analysis that under conditions in which the electron and hole densities and the hole velocities are approximately constant, the time dependence of the voltage transient is determined by the temporal evolution of the electron drift velocities. The experiment has been performed under these conditions.

Hence the measured temporal behavior of the voltage waveform and the calculated time dependence of the electron drift velocity may be compared directly.

Calculations and experiments have been compared with excitation wavelengths of 620nm and 760nm under conditions of high and low applied fields. All of the qualitative features of the Monte Carlo theory have been observed in the experiment. In particular, a significant photocurrent overshoot has been measured at E=10kV/cm which is not apparent at lower fields. This constitutes the first fully time-resolved qualitative measurement of velocity overshoot in GaAs. In addition, the Jones-Rees effect, which is apparent as a delay in the onset of photoconductivity at low fields, has also been measured.

Transient absorption spectroscopy is an all-optical technique which measures the shape of the joint electron and hole distribution function. To date this technique has been used to study the relaxation of a hot photoexcited distribution to its thermalized equilibrium state, in the process yielding important information about subpicosecond scattering processes in GaAs. A slight modification of the standard sample structure (addition of a n^+ layer and metallization) allows the experiment to be performed with an applied electric field. Thus heating of the electron distribution by the field may be studied, which is the process which drives velocity overshoot. Monte Carlo calculations of the evolution of the electron distribution function with various applied fields have been developed and compared with the experimental results. An increased population in the high-energy tail of the distribution has been consistently observed on a time scale of 100-200fs. Due to difficulties with the samples, which resulted in nonuniform field distributions in the structures, the observed effects were not as large as predicted. Suggestions were discussed for improving the experiment and optimizing the field in the samples which should yield experimental results in good agreement with the theoretical predictions.

7. Appendices

A1 DC IV Characterization of Metal-Semiconductor Contacts

It was discussed in chapter 4 that a series of contact metallizations and forms of GaAs were tried in the course of the transient photoconductivity study, and that some of these combinations resulted in "poor" metal-semiconductor contacts and that others resulted in "good ohmic" contacts. The basis for these qualifications will be described in this section.

It is well known that, in general, a metal evaporated onto a semiconductor will form a Schottky barrier. The band diagram for the interface is shown in Fig. A1.1.

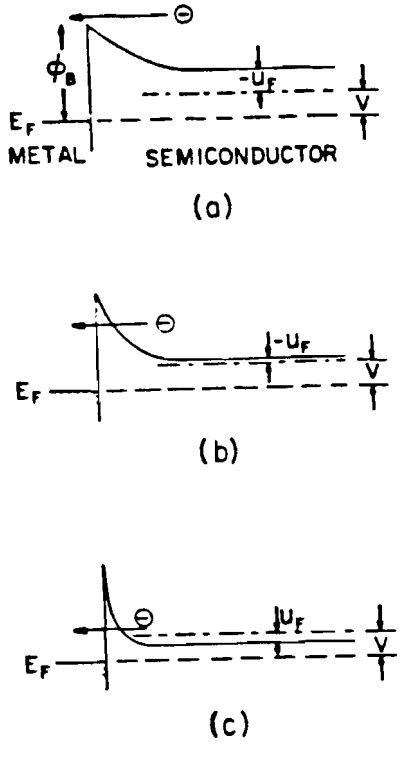

Fig. A1.1 Schematic band diagram of the metal-semiconductor interface: (a) thermionic emission mode; (b) thermionic-field-emission mode; (c) field emission mode [113]

There is a potential barrier between the metal and the semiconductor whose height and width depend upon the work function of the metal, the applied bias, and the doping of the semiconductor. The barrier may also depend on details of the surface preparation, i.e. whether or not an interfacial oxide layer exists. There are three regimes of transport across the interface. For lightly-doped semiconductors and wide barriers (Fig. A1.1(a)) electrons can only enter the semiconductor through thermionic emission over the barrier. This is the usual case for unannealed metals on undoped or lightly doped semiconductors; the current is determined by Schottky's diode equation [112]. For higher doping levels and lower work functions the emission over the barrier is accompanied by tunneling through the barrier; this mode is called thermionic-field-emission (Fig. A1.1(b)). Finally, if the barrier is thin enough then the tunneling current dominates in a process referred to as field emission (Fig. A1.1(c)). It is this latter condition that is most desirable for ohmic contact formation, since case the potential barrier appears almost transparent to carrier flow.

Achieving a high doping level in the interfacial region is critical for field emission injection. The standard approach to achieve this has been to use a metal or alloy which has a component that acts as a donor in the semiconductor of interest. For n-type GaAs the alloy of choice has been AuGeNi. When this alloy is annealed above the eutectic temperature Ge, a donor in GaAs, diffuses into the substrate. This forms a thin highly-doped layer between the metal and the semiconductor.

This system has been studied extensively and many different fabrication processes have been tried in order to optimize the contacts [113-117]. The chemistry at the interface during the anneal is quite complicated. While Ge diffuses into the substrate Ga outdiffuses; Ni also diffuses into the substrate, and grains of NiAsGe and AuGa alloys form at the surface [117]. In general the morphology of the surface is rough. Often doping spikes extend into the substrate instead of forming the desired

uniformly doped layer.[118]

For the photoconductivity experiments square contact pads with varying separations were fabricated along one edge of the chips for evaluation of the contacts. The initial measurements were carried out with the following structure: 200ÅNi/500ÅAuGe/2000ÅAu thermally evaporated onto semi-insulating Bridgeman-grown Cr-doped GaAs substrates. The substrates were cleaned with various organic solvents before being loaded into the evaporator. Representative IV curves for these samples (obtained with a Tektronix curve-tracer) are shown in Fig. A1.2. The characteristic of an unannealed sample with a 200um long gap is shown in Fig. A1.2(a). This is the classic diode behavior with turn-on at the extremely low field of 0.6kV/cm. These contacts fail at very low voltages. In Fig. A1.2(b) is shown the IV curve for a 50um long gap after furnace annealing for 10 minutes at 400C in a nitrogen atmosphere. This "soft diode" characteristic is representative of a leaky Schottky contact, in which tunneling through ohmic regions is in parallel with thermionic emission through areas of the contact where the doping was not effective.

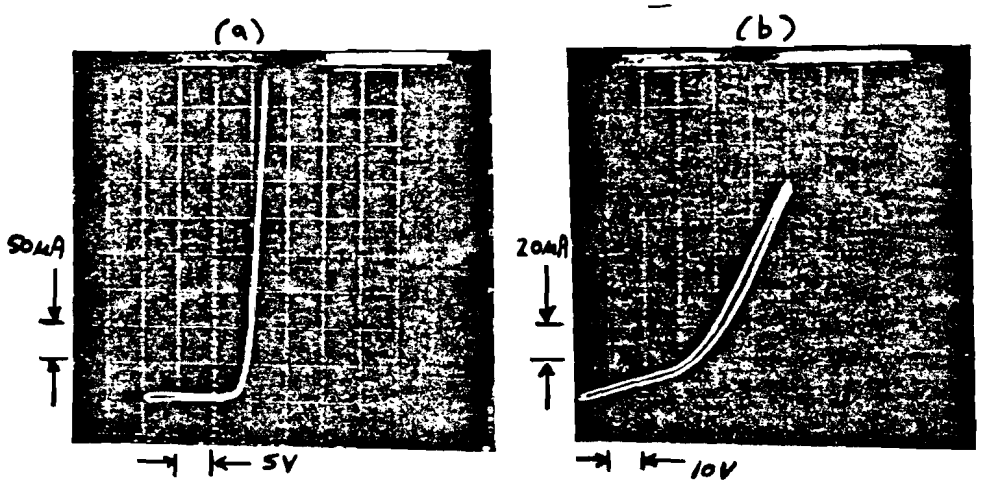

Fig. A1.2 IV curves for AuGeNi on Cr-doped semi-insulating GaAs: (a) unannealed 200um gap; (b) 50um gap after annealing at 400°C for 10 minutes in nitrogen.

The IV curve is linear to 6kV/cm but then increases sharply. The IV curve varies strongly from one test pattern to the next and from sample to sample within the batch indicating very nonuniform dopings under the contacts. These nonuniformities may have been caused by by an oxide or contamination on the surface, by the relatively poor quality of the GaAs (mobilities in boule-grown material are lower than in epitaxial material), or by the existence of deep traps in the GaAs (Cr is a mid-gap trap).

The next step in improving the contacts involved using undoped semi-insulating LEC GaAs and modifying the surface preparation. LEC GaAs does not have the Cr deep traps and is generally better quality material than the Cr-doped variety. Before loading the samples into the evaporator they were chemically cleaned and then a weak GaAs etch was used to remove 50-100Å of the surface. Then the samples were rinsed in de-ionized water and blown dry with dry nitrogen The samples were loaded immediately into the vacuum chamber and pumped down. This procedure was designed to remove the surface oxidation on the GaAs. Annealed

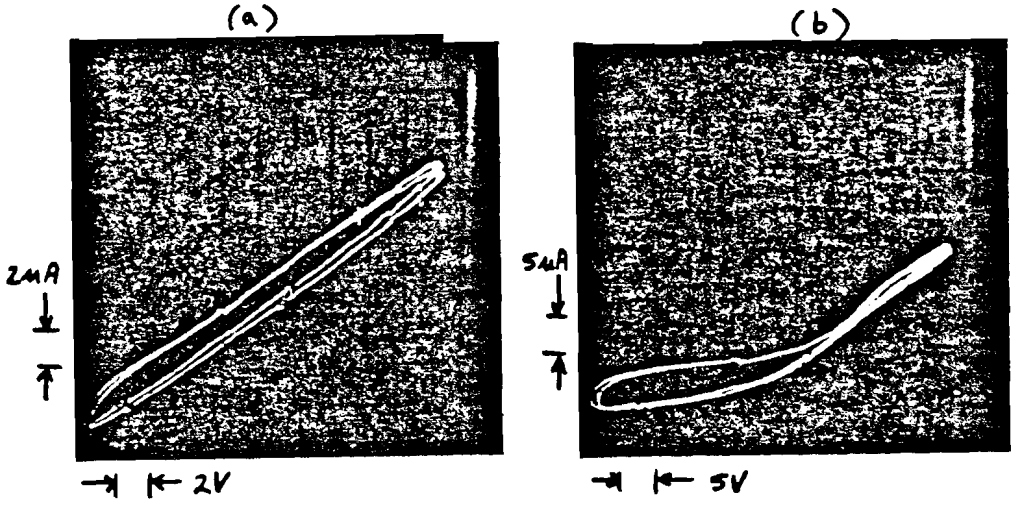

Fig. A1.3 IV curves for In on LEC GaAs annealed for 10 minutes at 400°C in a nitrogen atmosphere: (a) 10um gap; (b) 50um gap.

NiAuGe contacts were generally improved over the previous process. The best contacts were obtained using an evaporated annealed and In metallization (thickness=2000Å). According to Lakhani [119], annealed In on GaAs forms an InGaAs graded heterostructure in the interfacial region which assists tunneling into the GaAs.

Representative IV curves for two adjacent test patterns for a sample of annealed In on LEC GaAs are shown in Fig. A1.3. Some test patterns exhibited quasi-linear behavior to fields as high as 20kV/cm (Fig. A1.3(a)) while others demonstrated the "soft diode" bending of the current. Clearly the uniformity of the doping under the contacts was still not ideal. It was with these samples that some indication of a photocurrent overshoot was first observed (section 4.4.2).

At this point in the photoconductivity experiment, as discussed in chapter 4, it

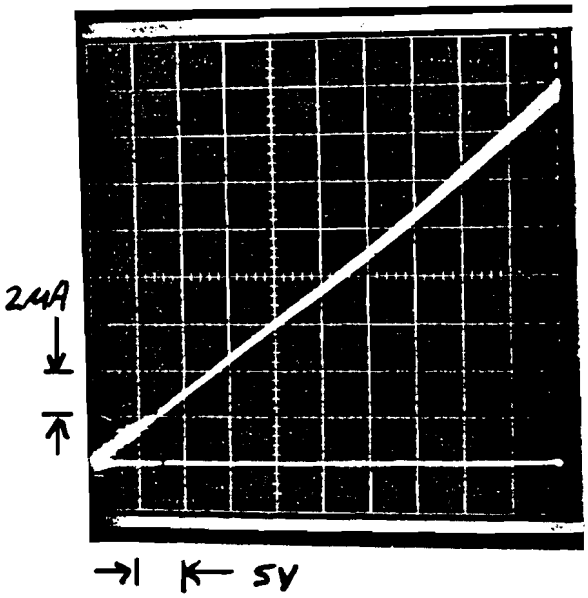

Fig. A1.4 IV curve for annealed NiAuGe contacts on epitaxial n^+/n-GaAs (gap length=10um).

was decided to extend the study to transport in epitaxial GaAs. MBE or MOCVD-grown GaAs has the highest purity and yields the highest mobilities of any GaAs known. An additional advantage is that during growth of the substrates a highly-doped n^+ cap can be included. This guarantees the existence of an extremely uniform highly doped layer at the surface. The problem of ohmic contact formation is the reduced to the problem of contacting to the heavily doped layer, which is straightforward. Fig. A1.4 shows the IV characteristic for annealed NiAuGe contacts on MBE-grown GaAs which .consisted of 500Å $2x10^{18}cm^{-3}$ n^+-GaAs/ 2um undoped ($5x10^{14}cm^{-3}$) GaAs grown on a semi-insulating substrate. After metallization the n^+ layer between the contacts was removed with a calibrated GaAs etch. The current was extremely linear to 50kV/cm, and furthermore the uniformity of the IV curves across a sample and from sample to sample was very good. The reproducibility of the I-V curves was +/- 5% throughout the batch. These samples yielded the reproducible photocurrent overshoot results discussed in detail in chapter 4.

A2. Description of Laser Sources and Amplifiers

A2.1 Colliding Pulse Mode-locked (CPM) and Linear-Cavity Near-IR Lasers

The transient photoconductivity measurements required subpicosecond high-repetition-rate laser pulses at visible and near-IR wavelengths. The visible wavelength (620nm) was obtained using a CPM dye laser [103,120,121]. In its original configuration this laser produced pulses as short as 120fs. Recently Valdmanis [103] has described optimization of the cavity configuration that allows pulse generation as short as 27fs. The layout of the dye laser is shown in Fig. A2.1. The dye laser is pumped with a CW argon-ion laser running at 514nm with an average power of 3W. The gain medium is rhodamine tetrafluoroborate in ethylene glycol and the saturable absorber is DODCI in ethylene glycol. The output coupler has a normal-incidence transmission of 3%. The repetition rate is determined by the cavity length and is typically 100MHz. The shortest pulses are produced when the net group velocity dispersion (GVD) in the cavity is at a minimum. Valdmanis added the four glass prisms to compensate for

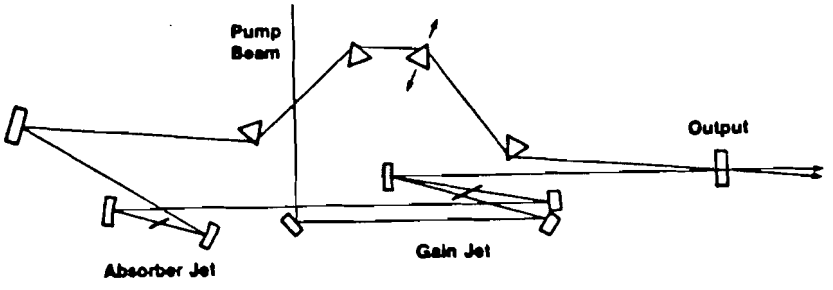

Fig. A2.1 Configuration of the CPM laser.

GVD introduced by the cavity mirrors and dye jets. Translating one prism laterally in the cavity varies the amount of GVD without affecting the cavity alignment. The minimum pulsewidth is obtained by monitoring the autocorrelation pulsewidth and adjusting the position of the prism. Pulses as short as 55fs with an average power of 10mW per beam (10pJ/pulse) were generated in our laboratory. During the transient photoconductivity measurements the laser typically generated pulses with durations of 65fs.

The laser used for the near-IR experiments was a synchronously-pumped linear-cavity dye laser, shown in Fig. A2.2 [122]. This laser is pumped with a Nd:YAG laser which generates 90ps pulses at a repetition rate of 100MHz and a (frequency-doubled) wavelength of 532nm. The average pump power is 850mW. The saturable absorber used was cryptocyanine and the gain medium was LDS722; in both cases the solvent was a combination of ethylene glycol and propylene carbonate. The maximum output power was 30mW and the minimum attainable pulsewidth was 300fs at a wavelength of 760nm. Unlike the CPM, adjustments in the amount of glass in the cavity only resulted in minor changes in the pulsewidth.

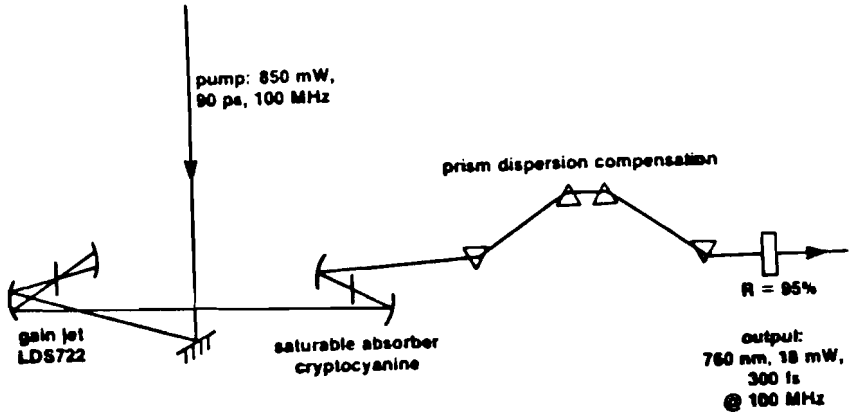

Fig. A2.2 Schematic of the linear-cavity near-IR dye laser.

A2.2 Synchronously-pumped CPM and Regenerative Amplifier

A diagram of the subpicosecond spectroscopy facility at LLE which was utilized for the transient absorption measurements is shown in Fig. A2.3 [123]. The system consists of four major components: a CW mode-locked Nd:YAG pump laser, a synchronously-pumped CPM dye laser [124], a multi-stage dye amplifier pumped with the output from a regenerative amplifier [125], and a continuum generation cell (described in section 5.3.1).

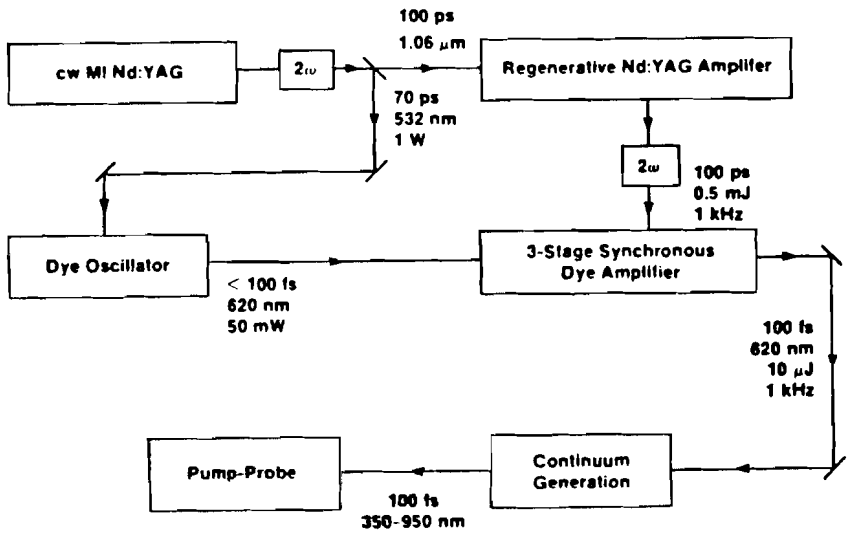

Fig. A2.3 Block diagram of the subpicosecond spectroscopy facility.

The synch-pumped CPM, shown in Fig. A2.4, is identical to that described by Norris et. al. [124] with the addition of four glass prisms for dispersion compensation, whose purpose was described in the preceding section. When the amount of glass in the cavity is optimized and the cavity length of the dye laser is precisely matched to that of the Nd:YAG laser (using a piezo-electric translator),

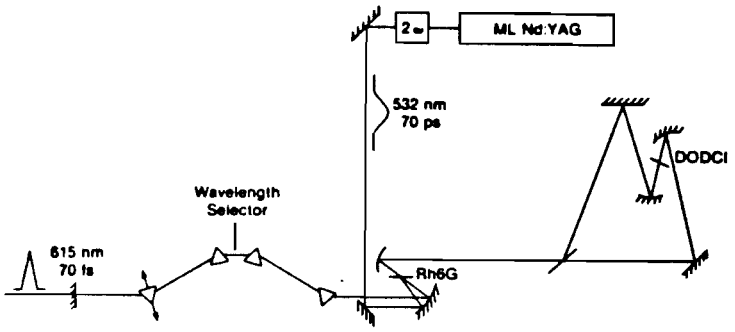

Fig. A2.4 Design of the synchronously-pumped CPM laser with prism dispersion compensation.

pulses as short as 70fs with an average power of 40-50mW may be generated. During the course of the transient absorption measurements the CPM routinely produced 100-120fs pulses.

A schematic of the regenerative amplifier (regen) and dye amplifier chain is shown in Fig. A2.5. This system has been described by Duling et. al. [125]. 15% of the cw mode-locked Nd:YAG power is converted to 532nm and is used to pump the CPM. About 300mW of the remaining IR power is sent through an optical fiber and the pulses are injected into another cw-pumped Nd:YAG cavity. After 40 round trips the pulses have been amplified to the 1mJ level and are rejected from the cavity with a cavity dumper. The regenerative amplifier can be run with a repetition rate as high as 1.7kHz; during the experiment a rate of 1kHz was used.

The regen output is frequency doubled and used to pump a standard 2- or 3-stage collinear dye amplifier chain. The amplifier dye was sulforhodamine 640 in 50/50 methanol/water and the saturable absorber was malachite green in ethylene

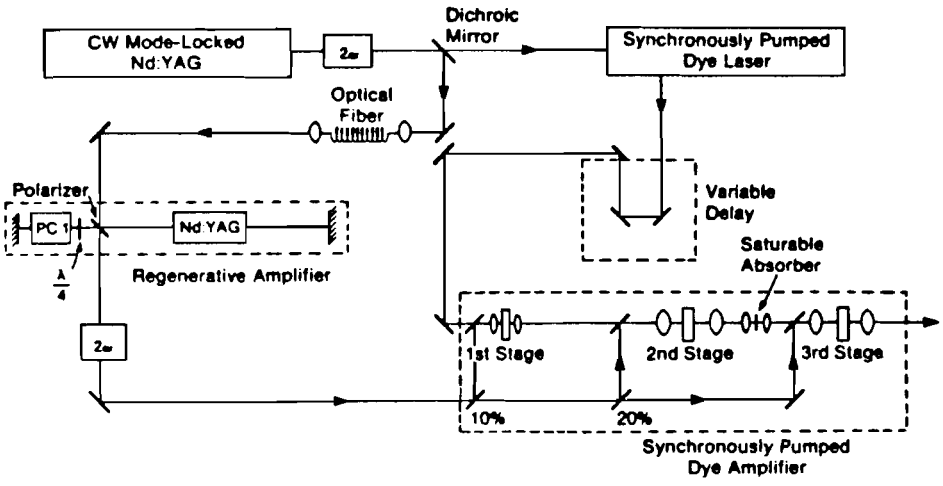

Fig. A2.5 Schematic of the regenerative amplifier and synchronously-pumped dye amplifier.

glycol. Using a 2-stage amplifier for the transient absorption experiments resulted in amplified dye pulse energies of 10uJ. Note that the dye oscillator pulses were pre-compensated with a prism pair before injection into the dye amplifier chain. This corrected for dispersion due to the optics in the amplifier and yielded amplified pulsewidths of 100-120fs.

A3. Recommendations for Future Work

A3.1 Transient Photoconductivity Experiment

a) Quantify the comparison between theory and experiment. The Monte Carlo transient velocities may be used as an input to a realistic circuit model of the photoconductive switch and transmission lines to predict the actual transient voltage on the terminal of the switch. This analysis is being developed by Bob Grondin and his students at Arizona State University.

b) Extend the study to other materials, including InP, AlGaAs, and relevant alloys. It would also be interesting to look at transport in p-type GaAs in which the electron mobilities are expected to be different than those in n-type material.

c) Extend the study to other structures. The optimal structure for achieving a uniform field in the sample would be a p-i-n structure, which would require replacing one of the n^+ contacts with a p^+ contact. Another interesting experiment would be to measure the transient photoconductivity in a HEMT layer; the electron mobilities in a two-dimensional gas are much higher than in bulk GaAs. This technique could be used to time-resolve real-space transfer as well as k-space transfer.

d) Perform the bulk GaAs experiment at low temperature. Velocity overshoot is expected to be significantly enhanced at 77K. The experiment should also be repeated with near-bandedge (870nm) photoexcitation to maximize the degree of velocity overshoot.

A3.2 Transient Absorption Experiment

a) As discussed in the text, the sample must be modified in order to defeat Gunn domain formation and allow for a uniform field in the structure. These steps should include: growing another MBE layer with reasonably low background doping; eliminating the electrical contribution from the AlGaAs layer by physically removing the layer from the back side of the sample using a selective etch; reducing the length of the sample (a 20um gap would be a reasonable size). Other possible steps to establish a uniform field might include using a p-i-n structure, carrying out the experiment in p-type GaAs, and pulse-biasing the sample on a time scale shorter than that necessary to form the domain.

b) For quantitative analysis of the data a careful measurement of the time-independent reflectivity and transmissivity of the sample needs to be carried out to establish the wavelength-dependent absorption coefficient.

c) The measured electron distribution should be plotted on a semi-log scale versus energy for interpretation of the temperature of the ensemble.

d) The experiment could be repeated at low temperature (77K) to yield information about the temperature dependence of the various scattering processes.

e) There is some controversy in the literature concerning hot-electron relaxation in bulk GaAs versus GaAs quantum wells. A series of different samples with various quantum well widths could be studied to shed light on what role the dimensionality of the sample plays in the relaxation and transport processes.

REFERENCES

1. B. K. Ridley and T. B. Watkins, Proc. Phys. Soc. (London) 78, 293 (1961).

2. J. B. Gunn, Solid State Comm. 1, 88 (1963).

3. J. B.Gunn, Int. Science Tech. , 43 (October, 1985).

4. B. K. Ridley, Proc. Phys. Soc. (London) 82, 954 (1963).

5. J. G. Ruch, IEEE Trans. Electron Dev. ED-19, 652 (1972).

6. M. Shur, Electron. Lett. 12, 615 (1976).

7. C. A. Liechti, IEEE MTT-24, 279 (1976).

8. B. Kim, H. Q. Tserng, and H. D. Shih, IEEE Electron Dev. Lett EDL-6, 1 (1985).

9. U. Mishra, E. Kohn, L. F. Eastman, Proc. of the 1980 IEEE Int. Electron Dev. Meeting, (Washington, DC) pg. 594.

10. W. R. Frensley, B. Bayraktaroglu, S. E. Campbell, H. Shih, and R. E. Lehmann, IEEE Trans. Electron Dev. ED-32, 952 (1985).

11. W. D. Goodhue, T. C. L. G. Sollner, H. Q. Le, E. R. Brown, and B. A. Vojak, Appl. Phys. Lett. 49, 1086 (1986).

12. J. S. Blakemore, J. Appl. Phys. 53, R123 (1982).

13. E. M. Conwell and V. F. Weisskopf, Phys. Rev. 77, 388 (1950).

14. H. Brooks and C. Herring, Phys. Rev. 83, 879 (1951).

15. J. L. T. Waugh and G. Dolling, Phys. Rev. 132, 2410 (1963).

16. L. Reggiani, in Hot Electron Transport in Semiconductors, edited by L. Reggiani (Springer-Verlag, NY, 1985) p.1.

17. X. Zhou, "Band Structure Engineering of III-V Compound Heterojunctions with Monte Carlo Calculations," Ph.D Thesis Proposal, Dept. of Elect. Eng., University of Rochester, 1987 (unpublished).

18. M. A. Osman and D. K. Ferry, J. Appl. Phys. 61, 5330 (1987).

19. M. A. Osman, "Electron-Hole Interaction Effects on the Relaxation of Hot Photoexcited Carriers in Seniconductors," Ph.D Thesis, Arizona State University, 1980.

20. J. L. Oudar, D. Hulen, A. Migus, A. Antonetti, and F. Alexandre, Phys. Rev. Lett. 55, 2074 (1985).

21. W. H. Knox, C. Hirlimann, D. A. B. Miller, J. Shah, D. S. Chemla, and C. V. Shank, Phys. Rev. Lett. 56, 1191 (1986).

22. D. W. Bailey, M. A. Artaki, C. J. Stanton, and K. Hess, J. Appl. Phys. 62, 4638 (1987).

23. P. Lugli and D. K. Ferry, Physica 117B & 118B, 251 (1983).

24. Robert Grondin, private communication.

25. P. N. Butcher and W. Fawcett, Phys. Rev. Lett. 21, 489 (1966).

26. W. Fawcett, A. D. Boardman, and S. Swain, J. Phys. Chem. Sol. 31, 1963 (1970).

27. R. Bosch and H. W. Thim, IEEE Trans. Electron Dev. ED-21, 16 (1974).

28. K. Blotekjer, IEEE Trans. Electron Dev. ED-17, 38 (1970).

29. E. Rosencher, Journal de Physique C7, supplement no. 10, 351 (1981).

30. J. Zimmermann, P. Lugli, and D. K. Ferry, Journal de Physique C7, supplement no. 10, 95 (1981).

31. R. Zwanzig, J. Phys. Chem. 40, 2527 (1966).

32. H. Mori, Proc. Theor. Phys. 33, 423 (1965).

33. D. K. Ferry and J. R. Barker, J. Appl. Phys. 52, 818 (1981).

34. R. Brunetti and C. Jacobani, Phys. Rev. B29, 5739 (1984).

35. P. Lugli, J. Zimmermann, and D. K. Ferry, Journal de Physique C7, supplement no. 10, 103 (1981).

36. R. Kubo, J. Phys. Soc. Jpn. 12, 570 (1957).

37. D. K. Ferry, H. L. Grubin, and G. I. Iafrate, in Semiconductors Probed by Ultrafast Laser Spectroscopy, edited by R. R. Alfano (Academic Press, NY, 1984) vol. 1, chapter 13.

38. B.Boittaux, E. Constant, L. Reggiani, R. Brunetti, and C. Jacobani, Appl. Phys. Lett. 40, 407 (1982).

39. R. W. McColl, R. L. Carter, J. M. Owens, and J. Shieh, IEEE Trans. Electron Dev. ED-34, 2034 (1987).

40. I. M. Sobol, the Monte Carlo Method, (Univ. Chicago Press, NY, 1974).

41. D. K. Ferry and J. R. Barker, Phys. Stat. Sol. B100, 683 (1980).

42. A. D. Boardman, W. Fawcett, and H. D. Rees, Solid State Comm. 6, 305 (1968).

43. M. A. Littlejohn, J. R. Hauser, and T. H. Glisson, Appl. Phys. Lett. 30, 242 (1977).

44. J. Frey, Proc. of the 1980 IEEE Int. Electron Dev. Meeting, December 1980 (Washington, DC).

45. R. O. Grondin, P. A. Blakey, and J. R. East, IEEE Trans. Electron Dev. ED-31, 21 (1984).

46. C. Jacobani and L. Reggiani, Rev. Mod. Phys. 55, 645 (1983).

47. C. V. Shank, R. L. Fork, B. I. Greene, F. K. Reinhart, and R. A. Logan, Appl. Phys. Lett 38, 104 (1981).

48. W. Franz, Z. Naturforsch. 13, 484 (1958).

49. L. V. Keldysh, Sov. Phys. JETP 7, 788 (1958).

50. K. Seeger, Semiconductor Physics, (Springer-Verlag, NY, 1973), p. 351.

51. D. H. Auston, K. P. Cheung, J. A. Valdmanis, and D. A. Kleinman, Phys. Rev. Lett. 53, 1555 (1984).

52. D. H. Auston and K. P. Cheung, J. Opt. Soc. Am B2, 606 (1985).

53. M. C. Nuss, D. H. Auston, and F. Capasso, Phys. Rev. Lett. 58, 2355 (1987).

54. D. H. Auston, Workshop on Femtosecond Physics in Semiconductors, sponsored by the Office of Naval Research, Dec. 9-11, 1987, Tempe, Arizona (unpublished).

55. M. S. Shur, Electron. Lett. 12, 615 (1976).

56. P. Das and D. K. Ferry, Solid State Electron. 19, 851 (1976); 20, 355 (1977).

57. S. Teitel and J. W. Wilkins, J. Appl. Phys. 53, 5006 (1982).

58. S. J. Allen, D. C. Tsui, F. Derosa, K. K. Thornber, and B. A. Wilson, Journal de Physique C7, supplement no. 10, 369 (1981).

59. S. J. Allen, C. L. Allyn, H. M. Cox, F. Derosa, and G. E. Mahoney, Appl. Phys. Lett. 42, 96 (1983).

60. M. E. Livinshtein and M. S. Shur, Sov. Phys.-Semiconductors 3, 915 (1970).

61. R. Zuleeg, IEEE Electron Dev. Lett. EDL-1, 234 (1980).

62. A. Yamashita, Jpn. J. Appl. Phys. 6, 1011 (1967).

63. L. F. Eastman, R. Stall, D. Woodard, N. Dandekar, C. E. C. Wood, M. S. Shur, and K. Board, Electron. Lett. 16, 524 (1980).

64. M. S. Shur and L. F. Eastman, IEEE Electron. Dev. Lett. EDL-1, 147 (1980).

65. S. Laval, S. Bru, C. Arnodo, and R. Castagne, Proc. of the 1980 Int. Electron Dev. Meeting, (IEEE, NY, 1980).p.626.

66. C. Bru, D. Pascal, S. Laval, C. Arnodo, and R. Castagne, in the Physics of Submicron Structures, edited by H. L. Grubin, K. Hess, G. I. Iafrate, and D.K. Ferry, (Plenum Pub., NY, 1984) p.219.

67. J. R. Barker, D. K. Ferry, and H. L. Grubin, IEEE Electron Dev. Lett.EDL-1, 209 (1980).

68. R. K. Cook and J. Frey, IEEE Trans. Electron Dev. ED-28, 951 (1981).

69. H. U. Baranger and J. W. Wilkins, Phys. Rev. B36, 1487 (1987).

70. J. R. Hayes, A. F. J. Levi, and W. Weigmann, Electron. Lett. 20, 851 (1984).

71. J. R. Hayes and A. F. J. Levi, IEEE J. Quant. Electron. QE-22, 1744 (1986).

72. U. K. Reddy. J. Chen, C. K. Peng, and H. Morkoc, Appl. Phys. Lett. 48, 1799 (1986).

73. A. P. Long, P. H. Beton, and M. J. Kelly, Semicond. Sci. Tech. 1, 63 (1986).

74. H. U. Baranger, J. L. Pelourd, J. F. Pone, and R. Castagne, Appl. Phys. Lett. 51, 1708 (1987).

75. A. Al-Omar and J. P. Krusius, J. Appl. Phys. 62, 3825 (1987).

76. J. Xu and M. Shur, J. Appl. Phys. 62, 3816 (1987).

77. A. P. Long, P. H. Beton, and M. J. Kelly, J. Appl. Phys. 62, 1842 (1987).

78. M. E. Kim, A. Das, and S. D. Senturia, Phys. Rev. B18, 6890 (1978).

79. P. Lugli and D. K. Ferry, IEEE Electron Dev. Lett. EDL-6, 25 (1985).

80. M. Heiblum, E. Calleya, I. M. Anderson, W. P. Dumke, C. M. Knoedler, and L. Osterling, Phys. Rev. Lett. 56, 2854 (1986).

81. I. Hase, H. Kawai, S. Imanaga, K. Kaneko, and N. Watenabe, J. Appl. Phys. 62, 2558 (1987).

82. D. E. Aspnes, Phys. Rev. B14, 5331 (1976).

83. J. F. Whitaker, G. A. Mourou, T. C. L. C. Sollner, and W. D. Goodhue, submitted to Physical Review Letters.

84. D. H. Auston, IEEE J. Quant. Electron. QE-19, 639 (1983).

85. J. A. Valdmanis, G. A. Mourou, and C. W. Gabel, IEEE J. Quant. Electron. QE-19, 664 (1983).

86. R. B. Hammond, Physica 134B, 475 (1985).

87. J. Xu, A. Bernhardt, M. Shur, C. H. Chen, and A. Peczalski, Appl. Phys. Lett. 49, 342 (1986).

88. R. O. Grondin and M. J. Kann, Proc. of the 1987 Hot Electron Conf., Boston, Massachusetts, July 1987 (to be published).

89. C. M. Caruso, "A Monte Carlo Simulation of the Electro-Optic Sampling Technique," Masters Thesis, Arizona State University, 1986.

90. J. A. Valdmanis, "Subpicosecond Electro-Optic Sampling," Ph.D Thesis, University of Rochester, 1983.

91. G. A. Mourou and K. E. Meyer, Appl. Phys. Lett. 45, 492 (1984).

92. K. J. Weingarten, M. J. W. Rodwell, H. K. Heinrich, B. H. Kolner, and D. M. Bloom, Electron. Lett. 21, 765 (1985).

93. R. K. Jain, D. E. Snyder, and K. Stenersen, IEEE Electron Dev. Lett. EDL-5, 371 (1984).

94. K. E. Meyer and G. A. Mourou, Electron. Lett. 21, 568 (1985).

95. J. A. Valdmanis, Workshop on Interconnections of High Speed and High Frequency Devices and Systems, sponsored by SPIE, Newport Beach, California, March 1988 (to be published).

96. J. Nees and G. Mourou, Electron. Lett. 22, 918 (1986).

97. K. Brennan and K. Hess, Phys. Rev. B29, 5581 (1984).

98. D. Jones and H. D. Rees, J. Phys. C6, 1781 (1973).

99. K. E. Meyer, M. Pessot, G. Mourou, R. L. Grondin, and S. Chamoun, submitted to Physical Review Letters.

100. D. von der Linde and R. Lambrich, Phys. Rev. Lett. 42, 1090 (1979).

101. R. F. Leheny, J. Shah, R. L. Fork, C. V. Shank, and A. Migus, Solid State Comm. 31, 809 (1979).

102. J. Collet, J. L. Oudar, and T. Amand, Phys. Rev. B34, 5443 (1986).

103 J. A. Valdmanis, R. L. Fork, and J. P. Gordon, Opt. Lett. 10, 131 (1985).

104. M. J. Rosker, F. W. Wise, and C. L. Tang, Appl. Phys. Lett. 49, 1726 (1986).

105. F. W. Wise, I. A. Walmsley, and C. L. Tang, Appl. Phys. Lett. 51, 605 (1987).

106. R. W. Schoenlein, W. Z. Lin, E. P. Ippen, and J. G. Fujimoto, Appl. Phys. Lett. 51, 1442 (1987).

107. D. W. Bailey, M. A. Artaki, C. J. Stanton, and K. Hess, J. Appl. Phys. 62, 4638 (1987).

108. W. H. Knox, M. C. Downer, R. L. Fork, and C. V. Shank, Opt. Lett. 9, 552 (1984).

109. J. D. Kafka and T. Baer, Opt. Lett.. 12, 401 (1987).

110. C. J. Wei, H. J. Klein, and H. Beneking, IEEE Trans. Electron Dev. ED-29, 1442 (1982).

111. P. Jeppesen and B. I. Jeppson, IEEE Trans. Electron Dev. ED-20, 371 (1973).

112. W. Schottky, Naturwissenschaften 26, 843 (1938).

113. A. Y. C. Yu, Solid State Electron. 13, 239 (1970).

114. N. Braslau, J. Vac. Sci. Tech. 19, 803 (1981).

115. W. Patrick, W. S. Mackie, S. P. Beaumont, and C. D. W. Wilkinson, Appl. Phys. Lett. 48, 986 (1986).

116. Y. C. Shih, M. Masanori, E. L. Wilkie, and A. C. Callegari, J. Appl. Phys. 62, 582 (1987).

117. M. Ogawa, J. Appl. Phys. 51, 406 (1980).

118. A. K. Roi, A. Ezis, A. W. McCormick, A. K. Petford-Long, and D. W. Langer, J. Appl. Phys. 61, 4682 (1987).

119. A. A. Lakhani, J. Appl. Phys. 56, 1888 (1984).

120. R. L. Fork, B. I. Greene, and C. V. Shank, Appl. Phys. Lett. 38, 671 (1974).

121. R. L. Fork, C. V. Shank, R. Yen, and C. A. Hirlimann, IEEE J. Quant. Electron. QE-19, 500 (1983).

122. This laser system was assembled, optimized, and maintained by Maurice Pessot.

123. The sync-pumped CPM and regenerative amplifier were assembled, optimized, and maintained by Ted Norris.

124. T. Norris, T. Sizer II, and G. Mourou, J. Opt. Soc. Am. B2, 613 (1985).

125. I. N. Duling, T. Norris, T. Sizer II, P. Bado, and G. A. Mourou, J. Opt. Soc. Am. B2, 616 (1985).

126. Mohammed Osman, private communication.

127. M. Hazakis, B. J. Canavello, and J. M. Shaw, IBM J. Res. Dev. 24, 452 (1980).

128. H. Klose, R. Sigush, and W. Arden, IEEE Trans Electron. Dev. ED-32, 1654 (1985).

129. Vicki Diadiuk, private communication.

130. J. M. Chwalek and D. R. Dykaar, to be submitted to IEEE Trans. Instr. Meas.

131. D. R. Dykaar, "Picosecond Switching Measurements of a Josephson Tunnel Junction," Ph.D thesis, Department of Electrical Engineering, University of Rochester, 1988.